

**Investigations on Interlaminar Fracture
Toughness of T300/914 Composite and Severe
Plastic Deformation of C70600 Alloy**

Thesis

Submitted in partial fulfilment of the requirement for the degree of

DOCTOR OF PHILOSOPHY

By

S SACHIN

Reg.No. 165010ME16F15



DEPARTMENT OF MECHANICAL ENGINEERING

NATIONAL INSTITUTE OF TECHNOLOGY KARNATAKA

SURATHKAL, MANGALORE – 575025

July 2022

DECLARATION

I hereby declare that the research thesis entitled “**Investigations on Interlaminar Fracture Toughness of T300/914 Composite and Severe Plastic Deformation of C70600 Alloy**” which is being submitted to the **National Institute of Technology Karnataka, Surathkal** in partial fulfilment of the requirements for the award of the degree of Doctor of Philosophy in Mechanical Engineering is a bonafide report of research work carried out by me. The material contained in this research thesis has not been submitted to any other universities or institutes for the award of any degree.

Register number: **165010ME16F15**

Name of the research scholar: **S Sachin**

Signature of the research scholar: *S Sachin* / 15/07/2022

Department of Mechanical Engineering

Place: NITK-Surathkal

Date:

CERTIFICATE

This is to certify that the Research Thesis entitled “**Investigations on Interlaminar Fracture Toughness of T300/914 Composite and Severe Plastic Deformation of C70600 Alloy**” submitted by **Mr. S. Sachin (Register Number: 165010 ME16F15)** as the record of the research work carried out by him, *is accepted as the Research Thesis submission* in partial fulfilment of the requirements for the award of the Degree of **Doctor of Philosophy**.

H.S. Nayaka
Dr. H. Shivananda Nayaka
Research guide

Date: *18/7/2022*



S. Sachin
Chairman- DRPC
18.7.2022

Acknowledgment

At first, I would like to express my sincere gratitude and heartiest thanks to my research guide **Dr. H Shivananda Nayaka**, Associate Professor, Department of Mechanical Engineering, National Institute of Technology Karnataka (NITK), Surathkal for his valuable guidance, inspiration, unwavering moral support, constructive criticism, and painstaking efforts during the course of this work.

It is an opportunity to thank the RPAC members, **Dr. Prasad Krishna** Professor, Department of Mechanical Engineering and **Dr. Jagannath Nayak** Professor, Department of Metallurgical and Materials Engineering, for evaluating the work and their precise suggestions and extended support during my research work.

I would like to thank **Dr. Santhosh B.** for his guidance and providing an opportunity to conduct tests at Vikram Sarabhai Space Centre (VSSC), Thiruvananthapuram, Kerala.

I wish to thank **Dr. Ravikiran Kadoli**, Professor and Head of the Department. I express my sincere gratitude to **Dr. K. V. Gangadharan**, **Dr. S. Narendranath**, **Dr. Shrikntha S. Rao** Professor and former Heads of Mechanical Department and all faculties in Department of Mechanical Engineering for giving opportunity to utilize facilities in the department and valuable support to complete my research work. I convey my gratitude to Mr. C A Verghese, Mr. Pradeep, Mr. Sudhakar Naik R, Mr. Mahaveera, Mr. K Nishan, Mr. Mahesh Anchan, Mr. Guruprasad, Mr. Avinash Devadiga for their kind support to execute the experiments.

It's my pleasure to submit my gratitude for **Dr. Ravishankar K. S**, Professor and Head, **Dr. K Narayan Prabhu** and **Dr. Udaya Bhat K.** Professor and Former Head, Department of Metallurgical and Materials Engineering for providing opportunity to use the facilities of Department of Metallurgical and Materials Engineering for completing my research work.

I would like to thank **Dr. B.M. Dodamani**, Professor and Head, and **Dr. Amba Shetty** Professor and Former Head, Department of Water Resources & Ocean En

gg. for giving an opportunity to conduct part of experiments in Department of Water Resources & Ocean Engg. I convey my gratitude to Mr. Vishwanath Poojary Mr. Shailendra, Mr. Padmanabha Acharya and Mr. Harish D S for their kind support to execute the experiments.

It is very important to thank **Dr. K. Umamaheshwar Rao**, former Director, NITK and **Ministry of Human Resource and Development** (MHRD) for their financial support provided for me during my research.

A special thanks to all my family, friends, teachers and well-wishers for their constant help, encouragement and support. And special thanks to my parents.

30/18/07/2022
S. Sachin

ABSTRACT

Experiments were conducted to investigate Interlaminar fracture toughness of carbon epoxy composite T300/914. carbon epoxy composite T300/914 has wide range of applications in aerospace industry as a structural material. For measuring inter-laminar fracture toughness, laminates with a thickness of 4.6 mm comprising of 48 layers of T300/914 are used. Hand layup technique were used to create these specimens, which were then cured in an autoclave machine. Double Cantilever Beam (DCB) test for Mode I and End Notch Flexure (ENF) test for Mode II were carried out in line with ASTM standards. The findings of pulse-echo tests and C-Scan pictures of the specimens were used to pinpoint specific locations of delamination. During early testing, it was discovered that the interlaminar fracture toughness varied due to release of film's bonding to laminate's sides. Mode I and Mode II fracture toughness values of T300/914 laminate composites were determined to be 0.090 kJ/m^2 and 0.542 kJ/m^2 , respectively, using Modified Beam Theory. Fracture toughness of identical laminate specimens changed depending on degree of compaction.

Copper-Nickel alloy, C70600, because of its superior anti-corrosion and anti-fouling properties, was used in sea water pipe line applications, C70600 was subjected to severe plastic deformation process by equal channel angular pressing (ECAP) technique. Material were pressed at room temperature along route B_C for 8 passes. Microstructural analysis, mechanical characterization and corrosion properties of the alloy was done for each of the ECAP processed samples. Initial homogenized material having equiaxial grains of average grain size $74\mu\text{m}$ was reduced to $20\mu\text{m}$ after 8 ECAP passes. Electron backscatter diffraction (EBSD) data presented an increase in low angle grain boundaries with increase in number of ECAP passes. Initially ultimate tensile strength (UTS) and hardness showed an increase of nearly 60% and 90% respectively. After 5th ECAP pass, drastic reduction in UTS and ductility was witnessed. Fractured surface revealed ductile type of failure with reduced ductility. Corrosion study showed improvement in corrosion resistance at higher ECAP passes.

CONTENTS

LIST OF FIGURES.....	xv
LIST OF TABLES.....	xxi
NOMENCLATURE.....	xxiii
SYMBOLS.....	xxv
PART-ONE INVESTIGATION ON INTERLAMINAR FRACTURE TOUGHNESS OF T300/914 COMPOSITE	1
Chapter 1 INTRODUCTION.....	1
Chapter 2 LITERATURE REVIEW	3
2.1 Important literature on T300/914 carbon epoxy component	3
2.2 Research Gap	9
2.3 Scope and objective	11
2.3.1 Scope.....	11
2.3.2 Objectives.....	11
Chapter 3 METHODOLOGY	13
3.1 Fabrication of laminate	13
3.2 Non-destructive testing (NDT) of laminates.....	14
3.2.1 Pulse-Echo test.....	14
3.2.2 C Scan Imaging.....	15
3.2.2.1 Description	15
3.2.2.2 Principle.....	15

3.3	Mode I.....	16
3.3.1	Position of hinge on the laminate.....	16
3.3.2	Procedure for Mode I (Double Cantilever Beam) test	17
3.4	Mode II.....	18
3.4.1	Procedure for Mode II (End notch flexure) test	18
3.4.1.1	Fracture test	18
Chapter 4 RESULTS AND DISCUSSION		21
4.1	Laminate test.....	21
4.1.1	Pulse-Echo.....	21
4.1.2	C Scan	23
4.2	Analysis of Fracture toughness test	24
4.2.1	Mode I.....	24
4.2.1.1	Calculations as per ASTM 5528 for Mode I (ASTM 2014).....	24
4.2.2	Mode II.....	26
4.2.2.1	Calculations as per ASTM D6671M for Mode II.....	26
Chapter 5 CONCLUSION.....		31
PART-TWO SEVERE PLASTIC DEFORMATION OF C70600 ALLOY.....		33
Chapter 6 INTRODUCTION.....		35
Chapter 7 LITERATURE.....		37
7.1	Severe plastic deformation processes	37
7.1.1	Multi-Directional Forging (MDF).....	37

7.1.2	Accumulative Roll Bonding (ARB).....	38
7.1.3	High-Pressure Torsion (HPT)	39
7.1.4	Equal Channel Angular Pressing (ECAP).....	41
7.2	Copper and Copper alloys.....	44
7.2.1	Copper	44
7.2.2	Physical properties	44
7.2.3	Copper alloys	45
7.3	Some important literature on C70600 alloy	46
7.4	Research Gap	56
7.5	Objectives of Research	57
Chapter 8 EXPERIMENTAL PROCEDURE		59
8.1	Flow chart	59
8.2	Material	60
8.3	Experimental setup.....	61
8.3.1	Universal Testing Machine (UTM).....	61
8.3.2	ECAP die.....	61
8.3.3	Lathe.....	63
8.4	Experimental procedure	63
8.5	Material characterization	64
8.5.1	Microstructural characterization	64
8.5.1.1	Optical microscope imaging.....	65
8.5.1.2	Scanning Electron microscope (SEM)	65

8.5.1.3	X-ray diffraction (XRD).....	66
8.5.1.4	Electron Backscatter Diffraction (EBSD)	67
8.5.2	Mechanical Characterization.....	68
8.5.2.1	Tensile test.....	68
8.5.2.2	Vickers micro hardness test.....	69
8.5.2.3	Corrosion test.....	70
Chapter 9 RESULTS AND DISCUSSION		73
9.1	Microstructure study	73
9.1.1	Optical microscope image analysis	73
9.1.2	XRD analysis	75
9.1.3	SEM Image analysis.....	77
9.1.4	EBSD analysis.....	79
9.2	Mechanical characterization	80
9.2.1	Micro hardness test	80
9.2.2	Tensile test	82
9.2.2.1	Fractography.....	85
9.2.3	Corrosion test	86
9.2.3.1	Potentiodynamic polarization study	86
9.2.3.2	Electrochemical impedance spectroscopy (EIS)	88
Chapter 10 CONCLUSION		91
SCOPE FOR FUTURE WORK		93
REFERENCES.....		95

DETAILS OF PUBLICATION:	107
BIO-DATA	109

LIST OF FIGURES

Figure 1.1 Failure modes of unidirectional composites.....	2
Figure 1.2 Basic fracture modes	2
Figure 2.1 (a) In-plane tensile test (b) through thickness tensile test (c) shear test results with respect to applied strain rate. (Hou and Ruiz 2000)	6
Figure 2.2 Healing property of Hollow Glass Fiber embedded in T300/914 composite (Williams et al. 2007)	8
Figure 3.1 Machining layup of Mode II laminate.....	13
Figure 3.2 Machining layup of Mode I laminate	14
Figure 3.3 Schematic representation of working of Pulse Echo test	14
Figure 3.4 Reading of Pulse echo test.....	14
Figure 3.5 Specimen mounting in C-Scan apparatus.....	16
Figure 3.6 C- Scan test apparatus	16
Figure 3.7 Location of Hinges	16
Figure 3.8 DCB specimen geometry and notation.....	17
Figure 3.9 ENF Specimen, Fixture, and Dimensions	19
Figure 4.1 Mode I laminate (a) front face (b) back face, Mode II laminate (c) front face (d) back face.....	21
Figure 4.2 Pulse echo readings of laminate with release film not soaked in release agent (a) & (b) area without delamination, (b) & (d) delaminated region	22
Figure 4.3 Pulse echo readings of laminate with release film soaked in release agent (a) & (b) area without delamination, (b) & (d) delaminated region.....	23
Figure 4.4 C Scan result of Mode I laminate	24

Figure 4.5 C Scan result of Mode II laminate before machining.....	24
Figure 4.6 Mode I Interlaminar fracture toughness	25
Figure 4.7 load vs displacement for specimen 1	27
Figure 4.8 Graph of Compliance vs cube of respective crack length	28
Figure 4.9 Mode II Interlaminar fracture toughness.....	29
Figure 6.1 MDF (Ramesh et al. 2019)	37
Figure 6.2 Schematic representation of Accumulative Roll Bonding setup (Mehr et al. 2015)	38
Figure 6.3 Schematic representation of High-Pressure Torsion setup (Xu et al. 2008)	40
Figure 6.4 Variation in the hardness along the length of Al6061 subjected to HPT (Xu et al. 2008)	40
Figure 6.5 Schematic representation of ECAP process	41
Figure 6.6 Sheared element formed during ECAP process (Kapoor 2017).....	42
Figure 6.7 Shear plane formed during ECAP along different routes (Valiev and Langdon 2006).....	43
Figure 6.8 Applications of Copper and Copper alloys	44
Figure 6.9 Periodic table and atomic properties of copper	45
Figure 7.1 Microhardness distribution across the stir zone of FS processed CuNi with and without addition of ZrCp.....	47
Figure 7.2 Anodic and cathodic polarization curves in aerated seawater at 50 °C for sodium dichromate pre-treated C70600 (2%, 1 hour at 50° C) as compared to untreated C70600 (Lee 1983)	49

Figure 7.3 Corrosion rate of C70600 exposed to different corrosive medium over different range of time (Al-Odwani et al. 2006)	50
Figure 7.4 Effect of iron concentration on the corrosion rate of C70600 alloy when exposed to sea water for 300 days (Stewart and LaQue 1952).....	51
Figure 7.5 schematic representation of steps involved in formation of corrosion layer for Cu-Ni 90/10 alloy (Ma et al. 2015)	52
Figure 7.6 Corrosion rates of CuNi 90/10 in flowing seawater showing the effect of exposure history and seawater chemistry: DS – deaerated and sulphide-polluted (0.05–0.1 g/m ³ O ₂ , 0.2–1.3 mg/l HS ⁻);.....	54
Figure 7.7 Corrosion rates for Alloy C70600 for long term seawater exposures (Tuthill 1987)	55
Figure 8.1 Flow chart for experimental procedure followed to conduct the experiments and testing	59
Figure 8.2 Machined sample of C70600 to execute ECAP	60
Figure 8.3 20T Universal Testing Machine	61
Figure 8.4 (a) Sectional view ECAP split die and plunger, (b) Material flow mechanism during ECAP [1]	62
Figure 8.5 ECAP Split die	63
Figure 8.6 ECAP processed C70600 alloy	64
Figure 8.7 Test specimen location	64
Figure 8.8 Optical microscope setup	65
Figure 8.9 Scanning electron microscope setup	66
Figure 8.10 X-ray diffraction (XRD) setup	66
Figure 8.11 Electron Backscatter Diffraction (EBSD) setup.....	67

Figure 8.12 Tensile test specimen.....	68
Figure 8.13 Dimensions of tensile test specimen.....	68
Figure 8.14 Tensile testing machine (Micro Universal Testing Machine)	69
Figure 8.15 Micro hardness testing setup	70
Figure 8.16 Corrosion test setup	71
Figure 9.1 Optical microstructure of C70600 copper alloy samples in (a)homogenised condition and ECAP (b) 1P, (c) 2P, (d) 3P, (e) 4P, (f) 5P, (g) 6P, (h) 7P, (i) 8P conditions.....	74
Figure 9.2 Change in average grain size with respect to number of ECAP passes	75
Figure 9.3 XRD graph of homogenized and ECAP processed samples	76
Figure 9.4 SEM image of (a)homogenized and ECAP processed samples (b) 1 pass, (c) 2 pass, (d) 3 pass, (e) 4 pass, (f) EDS data of processed sample	78
Figure 9.5 Orientation-imaging microscopy of C70600 alloy for homogenized and ECAP processed samples.....	79
Figure 9.6 Misorientation angle distribution of C70600 alloy for homogenized and ECAP processed samples.....	80
Figure 9.7 Hardness of homogenised and ECAP processed samples.....	81
Figure 9.8 Stress vs strain graph of homogenized and ECAP processed samples	82
Figure 9.9 Ultimate Tensile Strength and elongation for Homogenized and ECAP processed samples with respect to grain size.....	83
Figure 9.10 SEM image of tensile test fractured surface for (a) homogenized, ECAP pass (b)1, (c)5, (d)6.....	85
Figure 9.11 Tafel plot of Homogenized and ECAP processed samples in 0.1M, 0.5M and 1M NaCl solution.....	87

Figure 9.12 Tafel plot of homogenized and ECAP processed sample with increase in concentration of NaCl solution88

Figure 9.13 Nyquist plots for homogenised and ECAP processed Cu-Ni samples89

LIST OF TABLES

Table 1 Nominal composition of C70600 alloy.....	60
Table 2 Electrochemical kinetic parameters like corrosion potential, corrosion current and corrosion rate.....	86

NOMENCLATURE

ARB	: Accumulative Roll Bonding
ASTM	: American Society for Testing and Materials
BCC	: Body Center Cubic
CFRP	: Carbon fiber reinforced polymer
EBSD	: Electron Back-Scatter Diffraction
ECAP	: Equal Channel Angular Pressing
EDS	: Energy Dispersive X-ray Spectroscopy
EIS	: Electrochemical Impedance Spectroscopy
FCC	: Face Centred Cubic
FE-SEM	: Field Emission Scanning Electron Microscope
HAGB	: High Angle Grain Boundaries
HPT	: High Pressure Torsion
IPF	: Inverse Pole Figure
LAGB	: Low Angle Grain Boundaries
MAF	: Multi Axial Forging
MBT	: Modified Beam Theory
OIM	: Orientation Imaging Microscopy
OM	: Optical Microscopy
SAED	: Selected Area Electron Diffraction
SCE	: Saturated Calomel Electrode
SEM	: Scanning Electron Microscopy
SPD	: Severe Plastic Deformation
TEM	: Transmission Electron Microscopy
UFG	: Ultrafine grain
UTM	: Universal Testing Machine
UTS	: Ultimate Tensile Strength
XRD	: X-ray Diffraction
YS	: Yield Strength

SYMBOLS

a	: Length of delamination from loading points to crack tip
b	: Width of specimen
d	: Grain size
E_{corr}	: Corrosion potential
G_{I}	: Mode I Interlaminar fracture toughness value
G_{IC}	: Critical Mode I Interlaminar fracture toughness value
G_{II}	: Mode II Interlaminar fracture toughness value
G_{IIC}	: Critical Mode II Interlaminar fracture toughness value
h	: Thickness of specimen
HV	: Vickers microhardness
i_{corr}	: Corrosion current density
L	: Length of specimen
m	: Slope of the line
\emptyset	: Diameter
P	: Peak load
β_{a}	: Anodic constant
β_{c}	: Cathodic constant
δ	: Crack opening displacement
ε_{N}	: Equivalent strain
ρ	: Metal density
Φ	: Die channel angle
Ψ	: Outer arc of curvature

PART-ONE

**INVESTIGATION ON INTERLAMINAR
FRACTURE TOUGHNESS OF T300/914
COMPOSITE**

CHAPTER 1 INTRODUCTION

Composite materials have widely been used in aerospace applications, to reduce the weight, as well as, to improve functionality of the structure by tailoring strength. Laminated fiber-reinforced composites are becoming more popular in essential load bearing members (structures) and machinery. Laminated fiber-reinforced composite materials do have certain drawbacks despite all of their strengths. The basic building block of a laminated fibre-reinforced material is lamina (ply). Within a lamina, high-strength fibres are combined with a light-weight matrix. By selecting a bonded sequence of lamina with various orientations of principal material directions and/or different materials, wide range of mechanical properties of laminated composites can be designed according to needs. With this special material design methodology, material anisotropy and heterogeneity are greatly increased. As a result, many issues that do not exist, for isotropic and homogeneous materials arise when using laminated composites. The damage phenomenology of composite laminate is highly complicated due to material's intrinsic anisotropy. The degree to which a material fails is largely determined by the stress distribution inside it, which is impacted not only by the size of the applied load but also by its direction and the arrangement of the laminates.

The following categories apply to composite laminate failure modes:

- Intra-laminar failure: internal laminar fracture (i.e., matrix crack, fibre breakage, matrix-fibre debonding)
- Inter-laminar failure: Fracture between two adjacent plies, parallel to the plane of the fibres (i.e., delamination)
- translaminar failure: fracture is positioned transverse to the laminate plate.

Delamination is one of these damage mechanisms that is both crucial and poorly understood. Because delamination can result in a catastrophic loss of compressive strength, it is very critical. Non-destructive examinations may not always pick up little delamination, which may expand to unsafe configurations under in-service loads. Sometimes devices or buildings collapse tragically with no prior notice from the outside world. Delamination is a significant barrier to the greater use of modern composite materials in machines and buildings because of this failure scenario. Therefore, it is

essential to comprehend delamination better. The main focus of finite element analysis has been to capture both the beginning (initiation) and evolution of delamination.

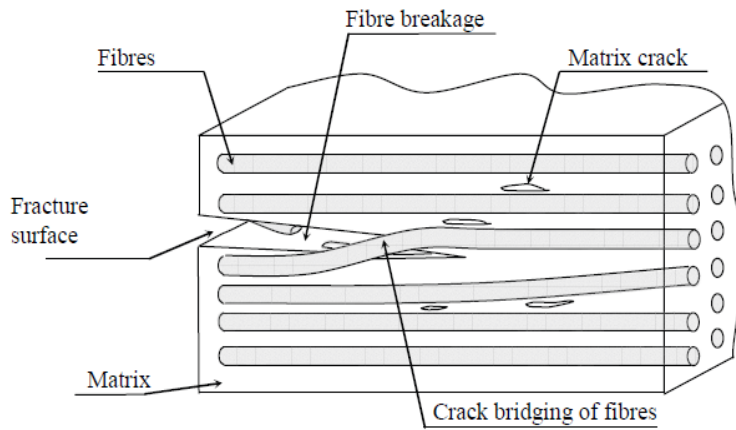


Figure 1.1 Failure modes of unidirectional composites

ASTM standard D5528-01 defines two major types of fracture for laminated composite materials based on relative displacement crack surfaces (Figure 1.2)

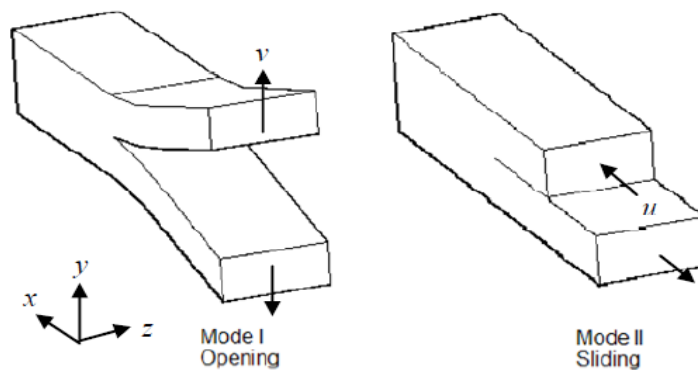


Figure 1.2 Basic fracture modes

Mode I (Crack Opening) — Mode I type of IFT (interlaminar fracture toughness) is a crack mode in which the delamination faces split away from each other and there is no relative crack face sliding. G_{IC} denotes the crucial value of interlaminar fracture toughness for delamination development in this mode.

Crack sliding mode (Mode II) — There is no relative crack face opening (in the direction perpendicular to the leading edge). Delamination faces move over each other in the direction of delamination growth. The interlaminar fracture toughness of Mode II is indicated by G_{IIC} .

CHAPTER 2 LITERATURE REVIEW

The following literature review focuses on crucial aspects of delamination that are directly related to the present study: Interlaminar fracture toughness (IFT) testing.

2.1 Important literature on T300/914 carbon epoxy component

Under static and fatigue loading, researchers Ramkumar et al. (Ramkumar 1985) looked at the roles of Mode I (opening mode) and Mode II (in-plane shear) strain-energy release rates (G_I and G_{II} , respectively) in producing delamination development. T300/5208 graphite/epoxy was used to make all of the specimens. Delaminations were placed between two 0° plies to prevent delamination from spreading over plies and onto neighbouring surfaces. Static double-cantilever-beam (DCB) experiments yielded fundamental Mode I strain-energy release rate, G_{Ic} . The overall strain-energy release rate was quantified using static testing employing mixed-mode cracked lap-shear specimens and then broken down into G_I and G_{II} components using a geometrically nonlinear finite-element approach. Critical Mode II strain energy release rate was calculated by incorporating the values of G_I and G_{II} , as well as G_{Ic} from static DCB test results.

Symons and Davis (Symons and Davis 2000) studied impact-damaged T300/914 carbon-fibre-reinforced plastic coupons when subjected to fatigue testing. BVID (barely visible impact damage) and VID (visible impact damage) were represented by two damage levels. A frequency of 5 Hz was selected for fatigue tests. Variations in ultrasonic C-scan in coupon modulus and hysteresis in impact damaged coupons were used to track the progression of fatigue damage. At dynamic rates of cyclic loading (2–5 Hz), significant hysteresis was measured for the overall force/extension response of impact damaged coupons.

Hallett (Hallett 2000) discovered that changing the impact mass by roughly 25% made no significant difference to the amount of damage generated to 21 unidirectional plies of T300/914 carbon-fibre composite. Analysing the fractured surface, it was discovered that the failure begins with fibre breakage at the rear face once the peak force is attained.

This started fracture then spreads throughout the specimen, followed by significant delamination. Energy balance equations have also been offered to explain the increase in damage.

Schön et al. (Schön et al. 2000) investigated the critical energy release rate of DCB specimens using both computational and experimental methods. Different interfaces ($0^\circ/0^\circ$, $45^\circ/45^\circ$, and $90^\circ/90^\circ$) and three materials, IM7/8552, HTA7/6376, and T300/914, were examined for static and cyclic characteristics. Different data analyses, as well as two-beam models against a FE solution, were tested. Non-zero interfaces have a plateau value that is almost four times greater than the onset value, which is nearly the same as the zero interface, according to toughness measured on DCB specimens. The fact is that the initial crack deviates from the original symmetrical fracture plane and results in higher toughness ratings. The rate of delamination development under fatigue increased sharply as the applied energy release rate increased, with the $0^\circ/0^\circ$ interface having the fastest growth rate. Specimen with a $90^\circ/90^\circ$ interface has the most uniform energy release rate distribution, whereas specimen with a $45^\circ/45^\circ$ contact has the most uneven energy release rate distribution. The critical energy release rate is much lower for T300/914 when compared to that for IM7/8552 and HTA7/6376.

Effect of loading rate on crucial energy release rate G_{Ic} of fibre-reinforced epoxy laminates was studied by Hug et al. (Hug et al. 2006). A new test apparatus was created in order to execute pure Mode I loading at greater opening velocities. A symmetrical opening displacement was performed on the DCB specimen. The impact of kinetic energy was considered during data reduction. At crack opening rates up to 1.6 m/s, findings obtained on unidirectional carbon–epoxy laminate T300/914 revealed a minor influence of loading rate on G_{Ic} strength.

Henaff-Gardin and Lafarie-Frenot (Henaff-Gardin and Lafarie-Frenot 2002) investigated the two-dimensional shear lag of cracked cross-ply composite laminate exposed to uniaxial loading while accounting for residual thermal stresses. This approach introduces a non-dimensional damage variable η , which is a function of

fracture density, material parameters, and stacking order of lamina. An investigation was performed on T300/914 CFRP composite material. In any cross-ply laminate subjected to uniaxial fatigue loading, the use of characteristic damage variable has led to phenomenological laws that allow accurate prediction of the number of fatigue cycles required for initiation of first matrix cracks, as well as the kinetics of this damage, up to "saturation" stage.

Shivakumar et al. (Shivakumar et al. 2006) modelled a delaminated composite structure based on fracture mechanics. Delamination growth comprises of 3 domains: subcritical, linear and ultimate fracture. In case of unidirectional composites, matrix cracking and fibre bridging increase resistance; in case of woven/braided fibre composites, two splitting, separation, bridging, and breaking increase resistance. Resistance was determined as a function of delamination extension using the ASTM standard Mode I fracture test. A fatigue onset life test was used to figure out the threshold energy release rate. Delamination growth rate (da/dN) was determined as a function of maximum cyclic energy release rate using a constant amplitude cyclic opening displacement fatigue test ($G_{I_{max}}$). The total life of the delamination growth rate was found and was verified for a block loading. It was found to accurately predict the delamination length.

Crack bridging traction study used to assess Mode I interlaminar fracture toughness of z-pinned fibre-polymer laminates was re-evaluated by Mouritz and Koh (Mouritz and Koh 2014). Existing bridging traction models include a number of simplifying assumptions regarding the physical state and failure mode of z-pins embedded inside laminates, which reduce the numerical accuracy. Misalignment of z-pins, interfacial cracking surrounding z-pins, porosity inside z-pins, and z-pin failure mode all impact traction qualities, according to microstructural studies and z-pin bridging traction tests. The traction loads computed with the improved model are more accurate than actual loads recorded for fibrous z-pins in a carbon-epoxy laminate.

Yasaee et al. (Yasaee et al. 2014) gave an experimental assessment of through-thickness reinforced composite laminates' mechanical performance and behaviour. Unidirectional (UD) and quasi-isotropic (QI) stacking sequences were examined. Pins in

UD samples had much higher pin/matrix binding strength than those in QI laminates, according to findings. Results show that a non-UD laminate type may undergo pin pull-out, resulting in greater energy absorption for a broader range of mode mixes than a UD laminate type.

For modelling delamination propagation under high-cycle fatigue stress, a damage model was devised by Turon et al. (Turon et al. 2007). The damage state was calculated as a function of loading circumstances and the material's empirically established Paris law crack propagation rate coefficients. It is demonstrated that experimental results may be recreated using the constitutive fatigue damage model in a structural analysis without the need for extra model-specific curve-fitting parameters.

Mode I delamination of z-pinned double-cantilever beams (DCB) and associated z-pin bridging processes were investigated experimentally by Liu et al. (Liu et al. 2007). Tests were carried out on three different types of samples: big-pin with a density of 2%, small-pin with a density of 2%, and small-pin with a density of 0.5%. Loading rates were set at 1 mm/min and 100 mm/min for each kind of sample. Rate impacts on delamination crack opening and growth may be seen by comparing fracture load under different loading rates. Optical micrographs of z-pins after pullout were also shown in order to determine the bridging mechanisms of z-pins at various loading rates.

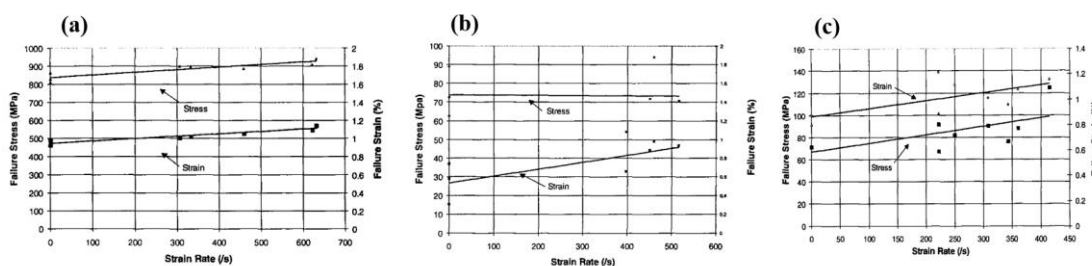


Figure 2.1 (a) In-plane tensile test (b) through thickness tensile test (c) shear test results with respect to applied strain rate. (Hou and Ruiz 2000)

J. P. Hou and C. Ruiz (Hou and Ruiz 2000) made measurements of in-plane characteristics of the woven CFRP T300/914. The measurements were made by the split Hopkinson pressure bar apparatus for high strain rate tension and compression

tests. Under strain until failure, samples in the warp and weft directions showed linear elastic behaviour until failure. Plastic deformation under compression occurs soon before fracture. While qualities dominated by the matrix are strain rate dependent because the resin is harder at high strain, those dominated by the fibres are not strain rate sensitive. A brittle failure under tensile strain has been seen in both the warp and weft orientations.

S. R. Hallett and C. Ruiz (Hallett and Ruiz 1997) tried to identify the dependence of the in-plane tensile test, through-thickness tensile test and shear test on strain rate by split Hopkinson pressure bar apparatus. It was experimentally found (Figure 2.1) that all three parameters were dependent on the applied strain rate.

F. Pierron and A. Vautrin (Pierron and Vautrin 1994) published two innovative experimental technique to find the shear modulus of laminated composites. The initial shear modulus of carbon/epoxy samples may be determined using the Iosipescu and off-axis tests, which are both proven to be reliable in this research. The extremely low dispersion also shows that these two techniques are precise enough to identify minute changes in shear modulus brought on, for example, by moisture absorption or damage. However, the authors' experience shows that in order to obtain such findings, precise specimen preparation and testing techniques are absolutely important.

D. D. Symons (Symons 2000) studied the high and low-speed impact on T300/914 carbon epoxy composite. The results showed delamination cracks are distributed across the thickness of a 0/90 lay-up laminate as a result of low-speed impact damage. Additionally, a fibre fracture initiates on the coupon's rear face. Increasing incident impact energy causes persistent indentation and delamination area to increase. The high-speed impact showed a higher permanent indent but was more localized than low-speed impact.

M. C. Lafarie-Frenot and F. Touchard (Lafarie-Frenot and Touchard 1994) compared the properties of the thermoset T300/914 and thermoplastic AS4/PEEK. It was seen that samples made of T300/914 and AS4/PEEK had similar shear behaviour from the time of loading until a force of roughly 150 MPa was applied. There is a relatively small

quasi-linear elastic range. Also, The amplitudes of shear stiffness loss and plastic strain build-up for the two materials were equal in this loading range. The thermoset matrix fracture formation is quicker above 150MPa up to failure. An explanation of why the T300/914 specimens failed earlier was found to be due to the thermoset matrix's reduced shear strength. Careful examination of the crack morphology and interply delaminations on the specimen edges were made to understand the reduction in shear strength.

A. Zhang et al. (Zhang et al. 2011) studied the impact of voids on the static bending and bending fatigue characteristics of T300/914 composite laminates that are subjected to various environmental conditions, including room temperature, hygrothermal conditions, and drying environments. It was discovered that the degree of the specimen's void content affected the reduction in material strength. The variations in weight and size grew progressively as the hygrothermal environment's porosity rose from 0.33 percent to 1.50 percent. It was discovered that the thickness direction saw the highest rate of dimensional change. With increased porosity, bending strength and fatigue performance were both diminished. Aged specimens had more severe damage evaluations than unaged and drying specimens.

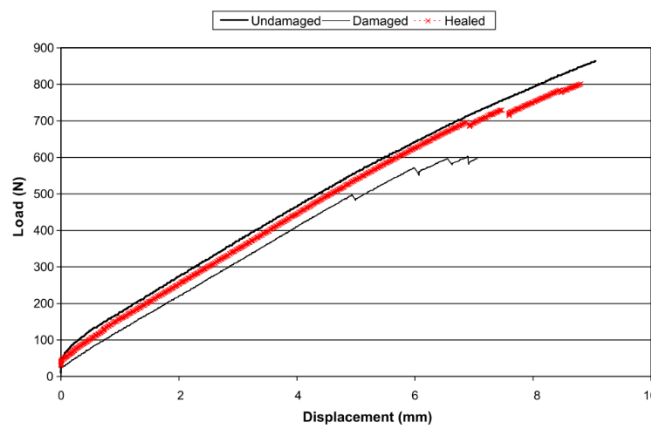


Figure 2.2 Healing property of Hollow Glass Fiber embedded in T300/914 composite (Williams et al. 2007)

G. Williams, R et al.(Williams et al. 2007) studied the effect on T300/914 carbon fibre

reinforced epoxy with resin-filled embedded hollow glass fibres (HGF), which provided a self-healing functionality. Due to energy absorption from HGF crushing, laminates with higher volume fractions of HGF showed a greater degree of damage tolerance during quasi-static impact events (Figure 2.2). In the course of an impact event, intra-ply shear fractures and delaminations result in HGF fracture and the release of healing resin into the linked damage sites. The absence of evident fracture path deviation in the presence of evenly dispersed HGF at a ply contact suggests that they do not produce weak points under these stressful circumstances. Small HGF clusters, in contrast, can significantly impair the fracture course when paired with resin-rich areas.

2.2 Research Gap

From the literature survey, it was seen that the T300/914 Carbon epoxy composite is widely used in space craft and air craft applications. The composite being laminate in form may inherently cause delamination due to mishandling of parts, accidental impact loading, moisture or air entrapment during the fabrication process. These delaminations tend to expand during service conditions and may lead to catastrophic failure of parts. Several researchers have studied the impact load behaviour of the material, the mechanism of fracture during different tensile and compressive loading conditions. There are multiple FEM analysis models available to study the effect of different layup angles on load-bearing capacity. But a detailed study on interlaminar fracture growth is not available in the literature. Two important modes of interlaminar fracture growth have not been addressed.

In this present work, 48 layered defect-free laminates were fabricated to determine the two major modes of interlaminar fracture growth, namely Mode I and Mode II.

2.3 Scope and objective

2.3.1 Objectives

- Fabricate defect-free 48-layer Carbon Epoxy laminate and generate required pre-crack.
- Fabricate Mode I test samples and experimentally determine Mode I fracture toughness of Carbon epoxy composite.
- Fabricate Mode II test samples and experimentally determine Mode II fracture toughness of Carbon epoxy composite.

2.3.2 Scope

- Setting up experimental setup to obtain Strain Energy Release Rate (SERR) of the specimen during each mode of fracture.
- Generation of test specimens for evaluating the growth of delamination or debond.
- Evaluation of crack growth during the test.
- Determination of crack growth using classical solutions available in the literature.

CHAPTER 3 METHODOLOGY

The current chapter explains the processes of fabrication and testing of carbon epoxy composite to determine different parameters required for predicting crack growth using modelling.

3.1 Fabrication of laminate

Laminates were made by stacking T300/914 prepreg cut to required dimensions. Laminates were placed one after the other in a single direction. To create the requisite artificial fracture, laminates were made out of 48 layers of prepreg with a release film added in the intermediate plane. All artificial cracks in the laminates were made of high-temperature no-bleed release film (Fluorinated Ethylene Propylene), that had been soaked in release agent (boron nitride complex) for 24 hours before being inserted into the layup. Both Mode I and Mode II laminates were vacuum bagged to 0.4 bar and cured for 2 hours at 170°C. A steady pressure of 0.4 bar was established in the autoclave machine. Laminates were 370mm x 170mm in size for Mode I and 400mm x 170mm in size for Mode II. Using a diamond-coated band saw cutter, laminates were reduced to 10 specimens measuring 165mm x 25mm for the Mode I test (Figure 3.2). Figure 3.1 shows a laminate sample cut to 190mm x 25mm dimensions for Mode II.

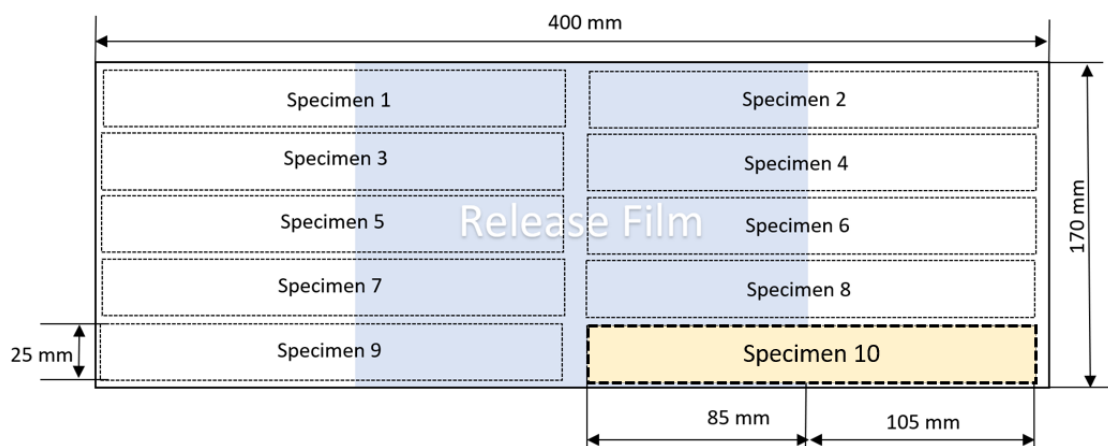


Figure 3.1 Machining layup of Mode II laminate

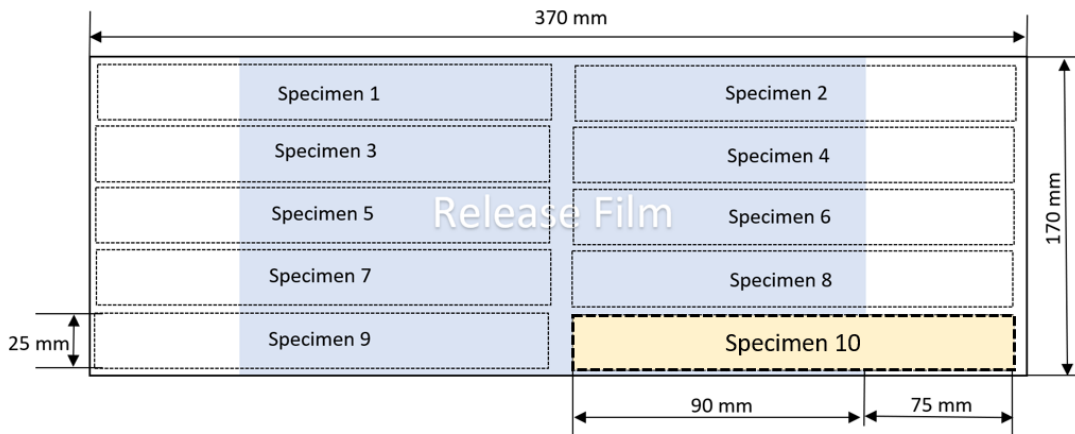


Figure 3.2 Machining layup of Mode I laminate

All dimensions shown are in mm.

3.2 Non-destructive testing (NDT) of laminates

Fabricated laminates were tested using pulse-echo and C-scanning to determine the presence of any defects in the laminates.

3.2.1 Pulse-Echo test

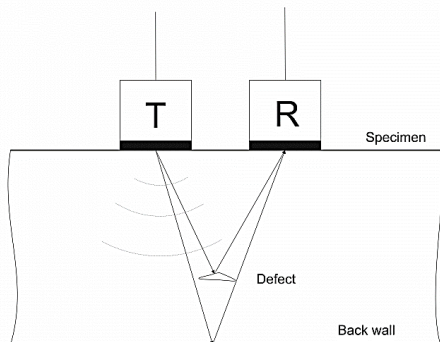


Figure 3.3 Schematic representation of working of Pulse Echo test

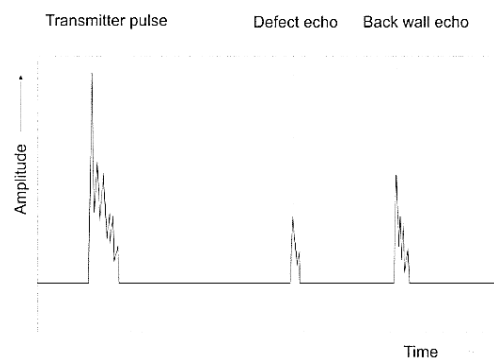


Figure 3.4 Reading of Pulse echo test

The ultrasonic pulse-echo method, often known as the pulse-echo method, is a non-destructive testing technique that detects faults in materials using ultrasonic waves. Figure 3.3 & Figure 3.4 depict the pulse-echo method's principles. The transmitter (T)

creates an ultrasonic pulsed wave that is reflected by inhomogeneity in the specimen, such as a defect or back wall, obtained by the receiver (R). As seen in Figure 3.4, the received signal is shown on a screen as peaks.

3.2.2 C Scan Imaging

3.2.2.1 Description

C-Scan is an NDT technique where a high-frequency ultrasound is passed through the material and the intensity of the signal received on the other side is analysed to find the location and size of the defect. This device allows for determining the depth of flaws in the sample. This feature makes it a helpful tool for tracking the specific delamination site between individual plies induced by impact or fatigue loading.

3.2.2.2 Principle

A focused transducer transmits an extremely high-frequency signal (up to 50 MHz) to the sample. At interfaces, flaws, porosities, and significant changes in acoustic impedance in the sample, the initial signal is partially reflected back to the transducer, while the rest of the signal, if not totally reflected, continues through the sample.

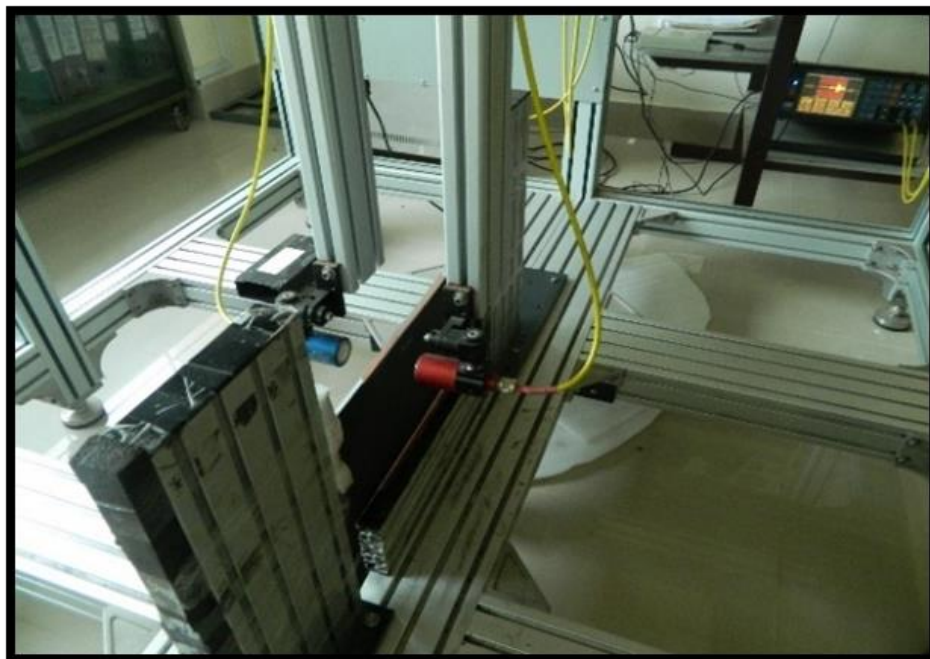


Figure 3.5 Specimen mounting in C-Scan apparatus



Figure 3.6 C- Scan test apparatus

3.3 Mode I

3.3.1 Position of hinge on the laminate

Hinges are attached at the delaminated region as shown in the Figure 3.7

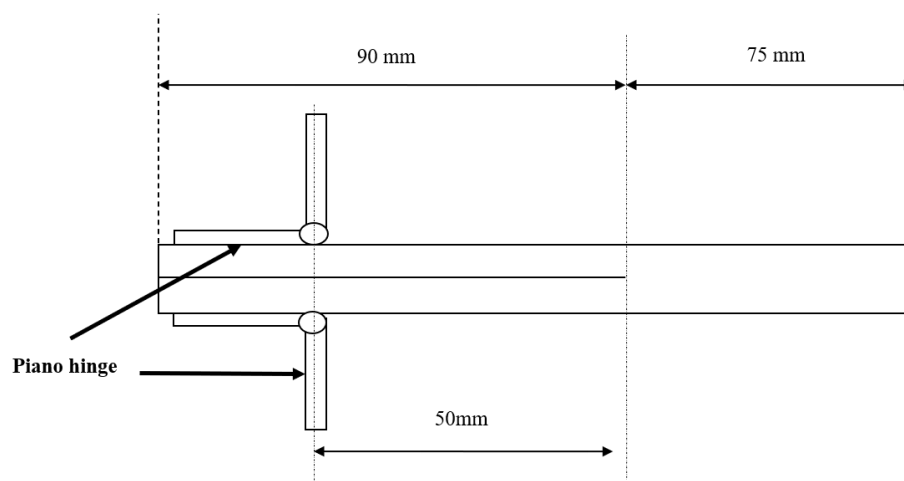


Figure 3.7 Location of Hinges

3.3.2 Procedure for Mode I (Double Cantilever Beam) test

- ❖ The width and thickness of the specimen are measured to the nearest 0.05mm. Any variation in length more than 0.1mm is not used for testing
- ❖ Both sides of the specimen ahead of the insert edges were coated with white paint for clear visualization of the front portion of the crack during testing.
- ❖ Along the side of the specimen markings are made to clearly quantify the crack length
- ❖ Piano hinges are mounted on the specimen at the delamination region (Figure 3.7)
- ❖ Specimens are loaded at a constant loading rate of 5mm/min.
- ❖ The load vs displacement graph is plotted. Also, the delamination position is recorded with an accuracy of $\pm 0.5\text{mm}$.
- ❖ The visual onset of delamination is marked in the load vs displacement graph.
- ❖ Loading was continued till the delamination grew by 5mm.
- ❖ The loaded specimens are unloaded at a constant rate of 25mm/min.
- ❖ The ends of delamination are marked on both sides of the specimen.
- ❖ From the new crack front, the crack is grown till the failure of the specimen by repeating the above steps.

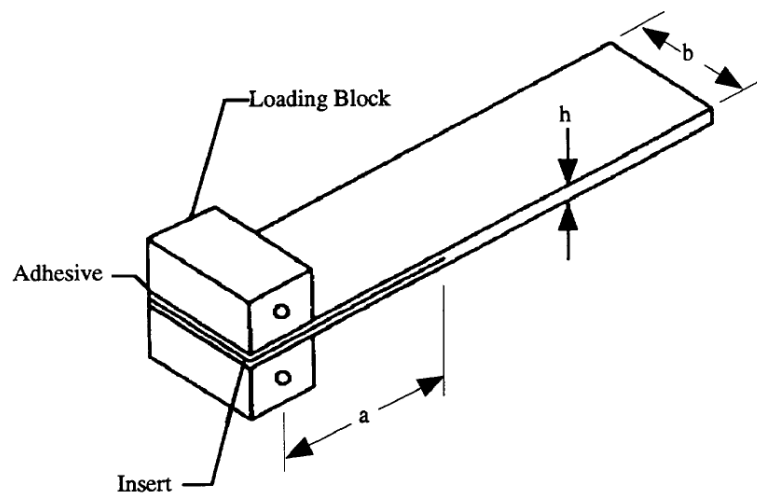


Figure 3.8 DCB specimen geometry and notation

3.4 Mode II

3.4.1 Procedure for Mode II (End notch flexure) test

- ❖ The sides of the specimens were coated with white paint and dried for clearly viewing the crack front during testing.
- ❖ Three compliance lines at 20mm, 30mm and 40mm are marked from the crack tip towards the crack end.
- ❖ 3-point bend test apparatus is used for the test with a 10mm diameter roller. The span of the support roller was set to 100mm.

Compliance Calibration Test

- ❖ The specimen was placed on the support roller such that the first calibration mark from the crack tip was supported above the roller. (20 mm mark)
- ❖ The load was applied at a constant rate of 0.5mm/min till the pre-calculated peak calibration load.
- ❖ Load vs Displacement graph was drawn during the test.
- ❖ Unloading was done at a constant rate of 1mm/min.
- ❖ The specimen was now placed on the support roller such that the last calibration mark from the crack tip was supported above the roller (40 mm mark)
- ❖ The load was applied at a constant rate of 0.5mm/min till the precalculated peak calibration load.
- ❖ Load vs. Displacement graph was drawn during the test.
- ❖ Unloading was done at a constant rate of 1mm/min

3.4.1.1 Fracture test

- ❖ The specimen was then placed on the support roller such that the middle calibration mark from the crack tip was supported above the roller (30 mm mark)
- ❖ The load was applied at a constant rate of 0.05mm/min till the crack propagation was seen or a dip in the load vs. displacement curve was seen.
- ❖ Load vs. Displacement graph was drawn during the test.
- ❖ The new crack tip was marked on the specimen.

❖ Unloading was done at a constant rate of 1mm/min

Load vs displacement data of all the tests are recorded with a minimum of 750 data points per test.

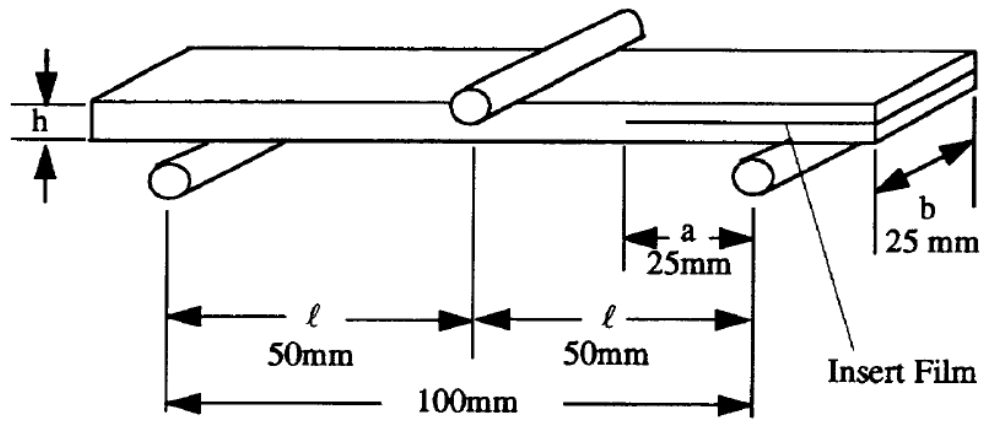


Figure 3.9 ENF Specimen, Fixture, and Dimensions

CHAPTER 4 RESULTS AND DISCUSSION

Figure 4.1 shows the laminates after autoclave curing for 2 hours for Mode I and Mode II. The position of the release film is also indicated in the figure. Laminates are of Size 370 X 170 mm and 400 X 170 mm, respectively, for Mode I and Mode II. These laminates are trimmed to specimen dimensions using a diamond-coated band saw cutter.

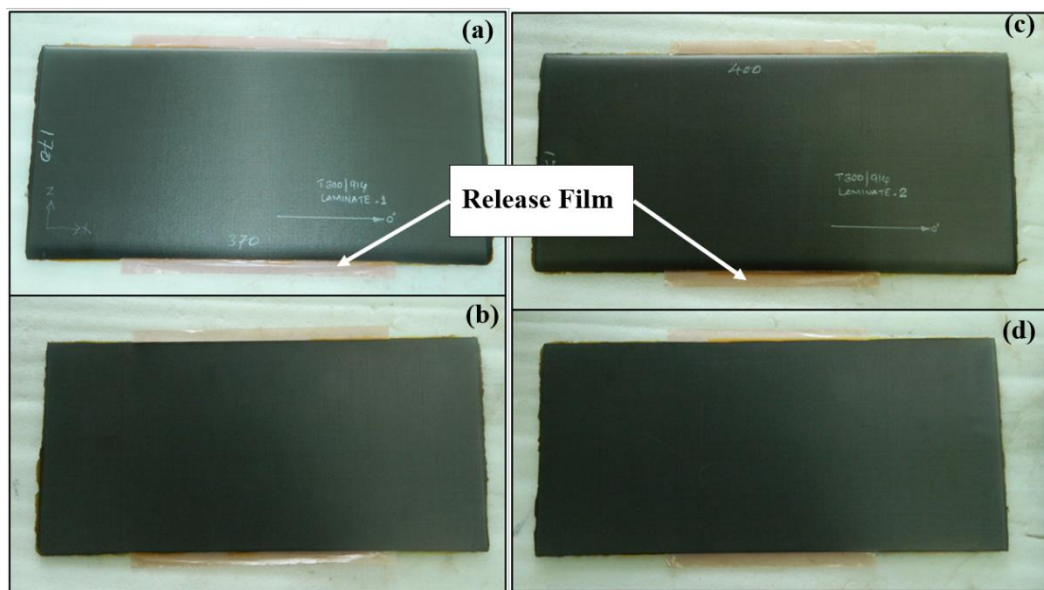


Figure 4.1 Mode I laminate (a) front face (b) back face, Mode II laminate (c) front face (d) back

4.1 Laminate test

4.1.1 Pulse-Echo

Pulse-Echo tests were performed on laminates fabricated for Mode I and Mode II testing, to confirm the existence of delamination caused by the release film. The creation of delamination was tried in one of the sets of laminates by placing the release film in the mid plane of laminates. It was clear from the pulse-echo test that release film operated as an inclusion rather than causing delamination (Figure 4.2). Two sets of peaks can be detected in the reading when the pulse signal is sent across the thickness of the laminate where the release film was not inserted (Figure 4.2 (b)). Two peaks

are caused by echo reflected from the laminate's top and bottom surfaces. A third peak appears in between the previous two sets of peaks when the pulse signal is delivered across the thickness of the laminate where the release film is positioned (Figure 4.2 (c)). It is a sign that there is a substance present that has a different density than the parent material.

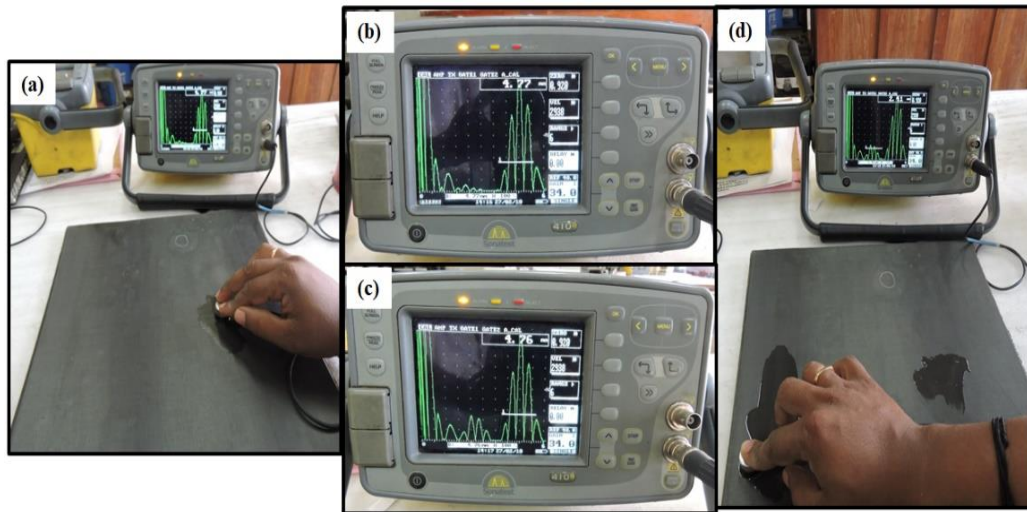


Figure 4.2 Pulse echo readings of laminate with release film not soaked in release agent (a) & (b) area without delamination, (b) & (d) delaminated region

The strength of signal reflected off the bottom surface of the laminate would decrease if it were delaminated, as seen in (comparing Figure 4.3 (c) and (d)). Pulses that would be transmitted to the opposite side of delamination would be decreased due to the existence of delamination (the rest would be reflected or absorbed by delamination), resulting in a reduction in signal echoing from the bottom surface. The release film that produced delamination in the laminate was created by soaking it in a release agent for 24 hours before inserting it in the laminate during the manufacturing process.

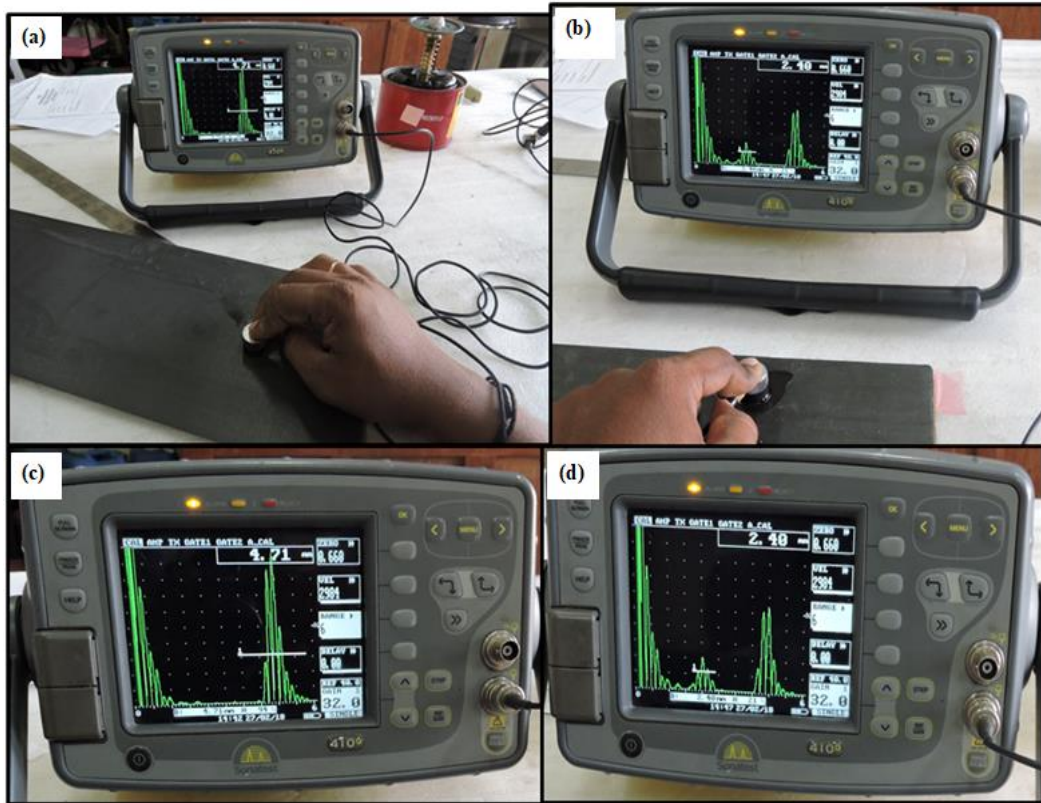


Figure 4.3 Pulse echo readings of laminate with release film soaked in release agent (a) & (b) area without delamination, (b) & (d) delaminated region

4.1.2 C Scan

Figure 4.4 and Figure 4.5 illustrate C-Scan imaging of laminate formed by soaking release film for Mode I and Mode II, respectively. Instead of detecting the echo of signal on the same side as in the pulse-echo test, signals transmitted from one side of the laminate are received by a sensor situated on the opposite side in C-Scan. This test allows for a better knowledge of the laminate's packing compaction.

The white region in the centre of Figure 4.4 and Figure 4.5 shows the positions of the release film (location of least compaction). The region of maximum compaction was very close to suction pump attachment during autoclave curing and is shown by dark blue regions in the Figure 4.4 and Figure 4.5. Location of Specimens A5, A6 from

Mode I laminate and position of specimens B3 and B4 from Mode II laminate are shown in the Figure 4.4 and Figure 4.5 respectively.

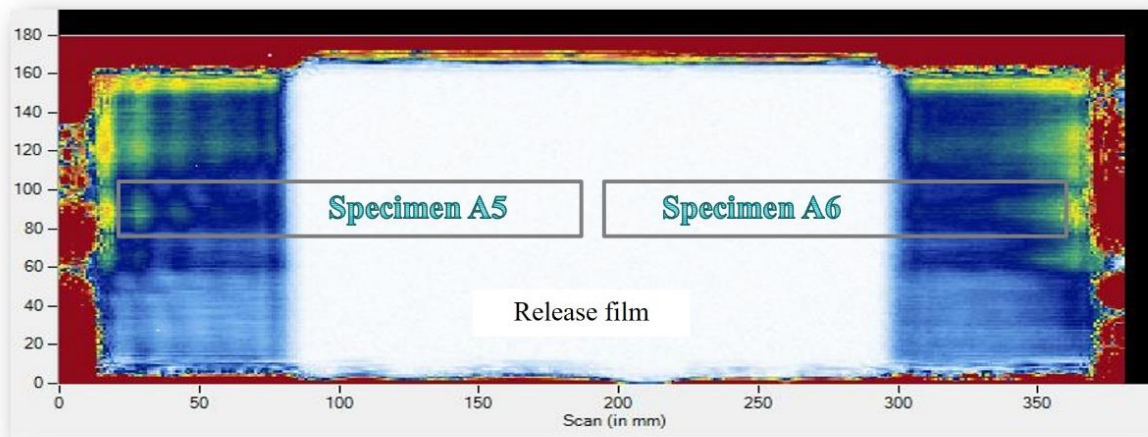


Figure 4.4 C Scan result of Mode I laminate

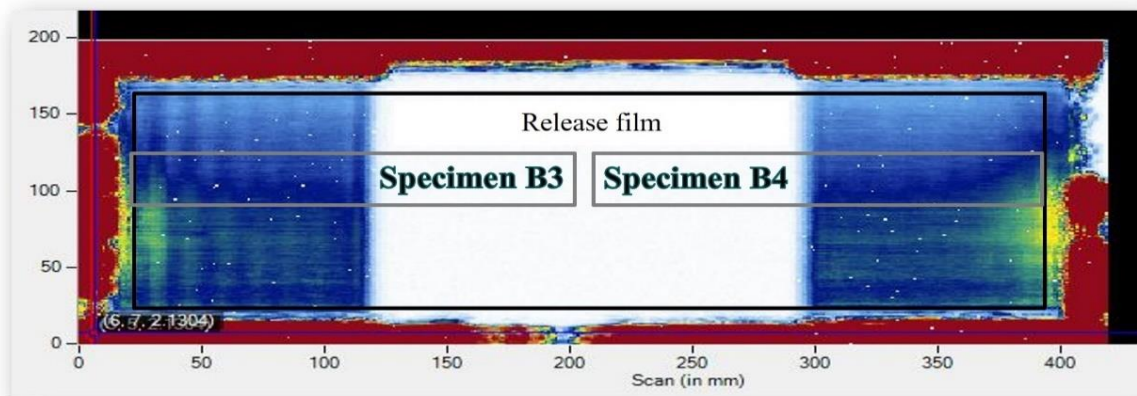


Figure 4.5 C Scan result of Mode II laminate before machining

4.2 Analysis of Fracture toughness test

4.2.1 Mode I

4.2.1.1 Calculations as per ASTM 5528 for Mode I (ASTM 2014)

Length of specimen L (mm) = 165

Width of specimen b (mm) = 25

Thickness of specimen 2h(mm) =4.8

$$G = \frac{3P\delta}{2ba} \quad (1)$$

Where, P and δ are the load and total crack opening displacement, respectively, b is the specimen width, a is the length of delamination from loading points to crack tip. Interlaminar fracture toughness of Specimen A2 at different crack lengths are calculated and shown in Figure 4.6. Modified Beam Theory (MBT) procedure is widely accepted for calculating Mode I interlaminar fracture toughness of a specimen. Figure 4.6 shows Mode I interlaminar Fracture Toughness values of all specimens tested. It is noted that specimens A5 and A6 show higher interlaminar fracture toughness due to a higher degree of compaction than in other regions (Figure 4.4).

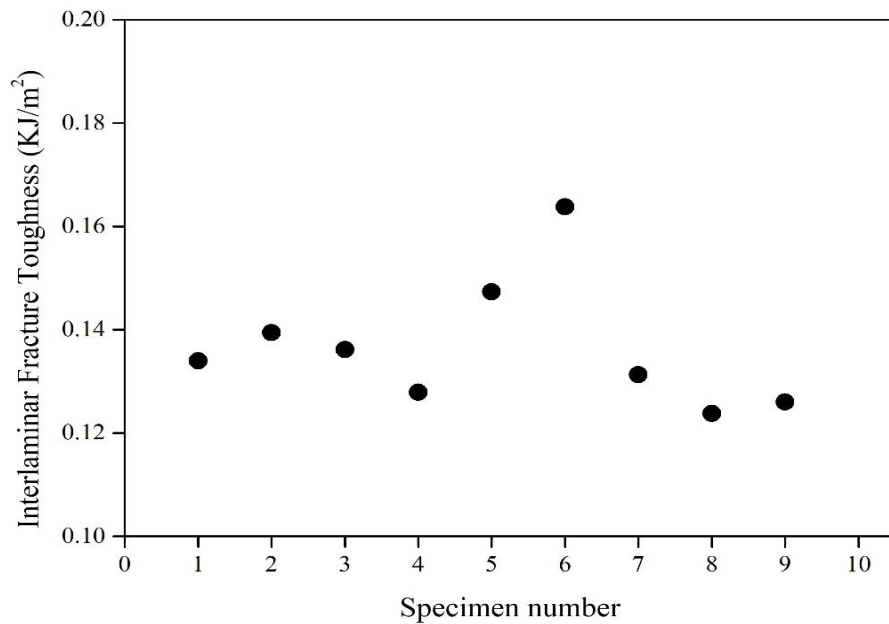


Figure 4.6 Mode I Interlaminar fracture toughness

4.2.2 Mode II

4.2.2.1 Calculations as per ASTM D6671M for Mode II

Length of specimen L(mm)		=190
Width of specimen B(mm)		= 25
Thickness of specimen 2h(mm)		=4.8
Crack length (a_1) (mm)		=20
Crack length (a_2) (mm)		=30
Crack length (a_3) (mm)		=40
Compliance load applied at 40mm compliance line (N)		= 400
Slope of load vs Displacement curve (Figure 4.7)	m_1	=470.9
Compliance load applied at 20mm compliance line (N)		= 400
Slope of load vs Displacement curve (Figure 4.7)	m_2	=675.8
Maximum load at failure P_{max} (N)		=912.5
Slope of load vs Displacement curve (Figure 4.7)	m_0	=619.6

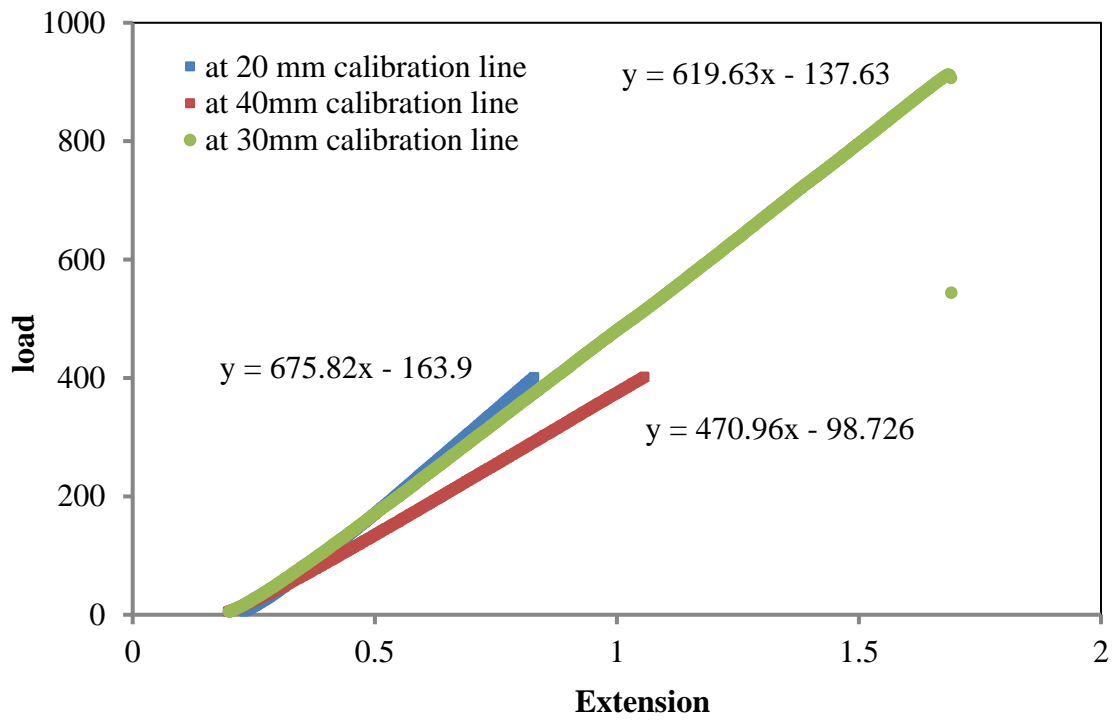


Figure 4.7 load vs displacement for specimen 1

Compliance

$$C_j = \frac{1}{m_j}$$

$j = 0, 1, 2$

$$C_1 = \frac{1}{m_1}$$

$$= 1/470.9$$

$$C_1 = 0.00212$$

Similarly, $C_2 = 0.00140$

$$C_0 = 0.001562$$

From the graph in Figure 4.8

Intercept in X axis A = 0.001

Slope m = 0.00000001

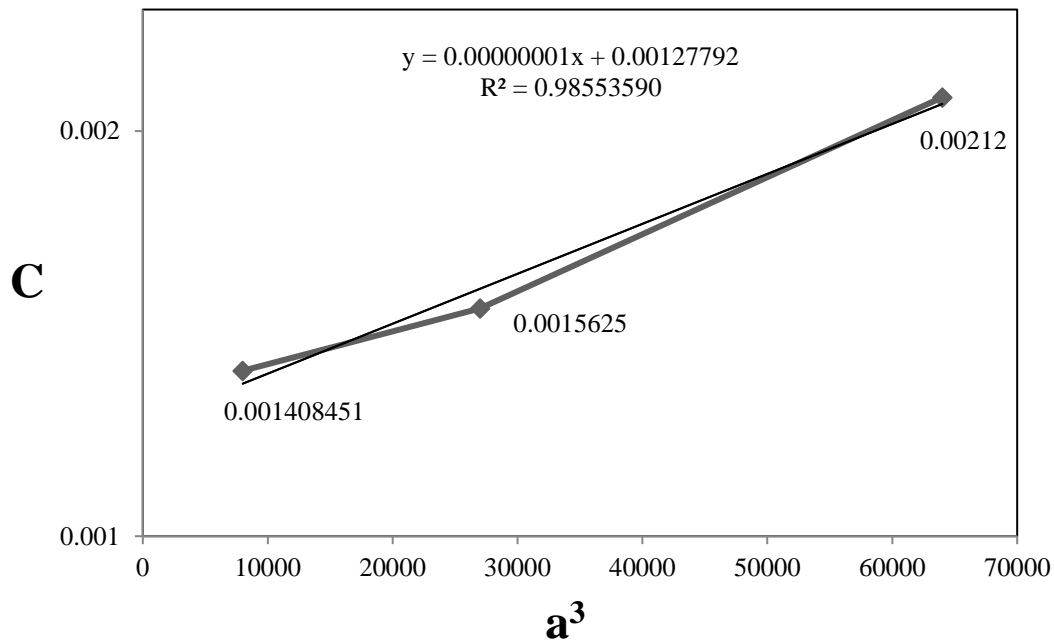


Figure 4.8 Graph of Compliance vs cube of respective crack length

The candidate toughness (G_{IIC}) is determined using

$$G_{IIC} = \frac{3mP_{max}^2 a_0^2}{2B}$$

$$G_{IIC} = \frac{3(0.00000001)912.5^2 30^2}{2 * 25}$$

$$G_{IIC} = 0.449634375 \text{ kJ/m}^2$$

New calibration loads (Pj) are determined by

$$E_{Ij} = \frac{L}{4ABh^3}$$

$$= 4961661$$

$$P_j = \frac{2B\sqrt{G_{IIc}E_{lf}h^3}}{3a_j}$$

j= 1,2

P1 = 450 P2 = 450

Mode II interlaminar fracture toughness for Non-pre-cracked specimen of all the specimens are calculated and the results are shown in Figure 4.9

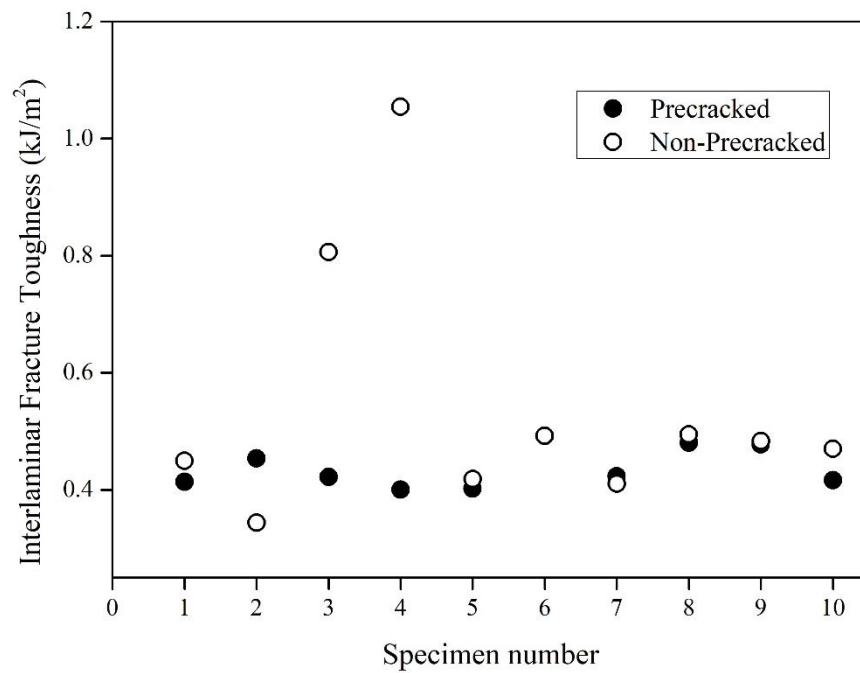


Figure 4.9 Mode II Interlaminar fracture toughness

CHAPTER 5 CONCLUSION

- The current work is based on an experimental analysis of interlaminar fracture toughness for composite T300/914 in Mode I and Mode II.
- Larger compaction laminates were able to tolerate higher loads before fracture propagation.
- The specimen's Mode I Fracture Toughness is calculated to be 0.140 kJ/m^2 using the modified beam theory.
- The specimen's Mode II fracture toughness is calculated to be 0.542 kJ/m^2 .
- When compared to other locations, the region near the vacuum pump during the autoclave curing process showed a higher degree of compaction. Due to severe compaction in this location, the release agent was pushed out of the release film, which failed to provide the required artificial delamination for the test.

PART-TWO

**SEVERE PLASTIC DEFORMATION OF
C70600 ALLOY**

CHAPTER 6 INTRODUCTION

Metals have been an integral part of human race from for a long time. Archeologists have recorded artifacts made of Copper, Gold, Silver, lead from the prehistory times. Their importance has been repeatedly documented by archeologists who have named the Ages of Mankind on the basis of the materials used by society — Stone Age, Copper Age, Bronze Age, and Iron Age. World war I and World War II have boosted the need of advancement in material properties than the naturally available properties. This has led to sudden increase in development of new techniques to improve existing materials. Different methods adopted include alloying, composite structuring, heat treatment, surface treatment, strain hardening etc.

In alloying, two or more elements are mixed together to form a new component by chemical bonding. Properties of the formed material depend on alloying elements and proportion of each element used. Similarly, a composite is formed by mixing two or more immiscible elements to form a strong physical bonding between elements. Properties of composites depend not only on composition but also on the orientation of each component. Properties of composite may be tailor made to produce functionally graded materials that suit a particular requirement. Alloying and composite designed structure are adopted during initial stages of processing like casting process. Hence, alteration of properties of already formed material require other advanced techniques.

Heat treatment techniques have been in practice since a long time. Material of interest is heated to required temperature and held there for predetermined time and then cooled to room temperature at a defined rate. During the process, recrystallization takes place in the material and the dwelling time allows for recrystallization and phase transformation of required number of grains. Cooling rate is determined by the phase and size of grain required at the end of process. Similar processes may be adopted to cause grain restructuring of surface level grains only. This process is called surface heat treatment.

According to Hall- Petch equation the strength of the material can be improved by reducing the grain size (Hall 1951). This has led to development of new techniques to

create bulk material with ultra-fine grain (UFG) structure. Severe plastic deformation (SPD) is one of the methods to generate UFG materials. Some of the commonly used SPD techniques are Multi-Directional Forging (MDF), Accumulative Roll Bonding (ARB), High Pressure Torsion (HPT), Equal Channel Angular Pressing (ECAP).

In ECAP technique the material is passed through two channels intersecting at an angle. As the materials passes through the intersection, shear strain is induced the material. The material may be passes multiple number of times to accumulate the shear strain induced in the material. This leads to structural refinement in the material causing improvement in the mechanical properties.

C70600 is an alloy of Copper and Nickel. It is primarily used in marine structural application because of their superior biofouling properties, corrosion resistance to saline water and low cost. It is majorly used in ship building, heat exchangers, piping in desalination plants, etc. Because of their wide acceptability, many studies have taken place to understand the corrosion mechanism taking place in the material when subjected to different sea water conditions. Limited literature is available addressing the mechanical properties of the alloy. In the following chapters, the mechanical properties of the material are discussed and improvement in the mechanical properties achieved by ECAP process is explained.

Chapter 7 LITERATURE

Different types of severe plastic deformation processes and literatures available on C70600 alloy are presented in this chapter

7.1 Severe plastic deformation processes

Strain hardening or work hardening is a process of increasing the strength of the material by introducing deformation in the material. Deformations cause generation of dislocations in the material. Properties of deformed materials are altered because of generation of new dislocations and moment of dislocations in crystal structure of the material. Strain hardening can be introduced by different methods of severe plastic deformation. Some of the commonly used severe plastic deformation methods are

1. Multi-directional forging (MDF)
2. Accumulative roll bonding (ARB)
3. High pressure torsion (HPT)
4. Equal channel angular pressing (ECAP)

7.1.1 Multi-Directional Forging (MDF)

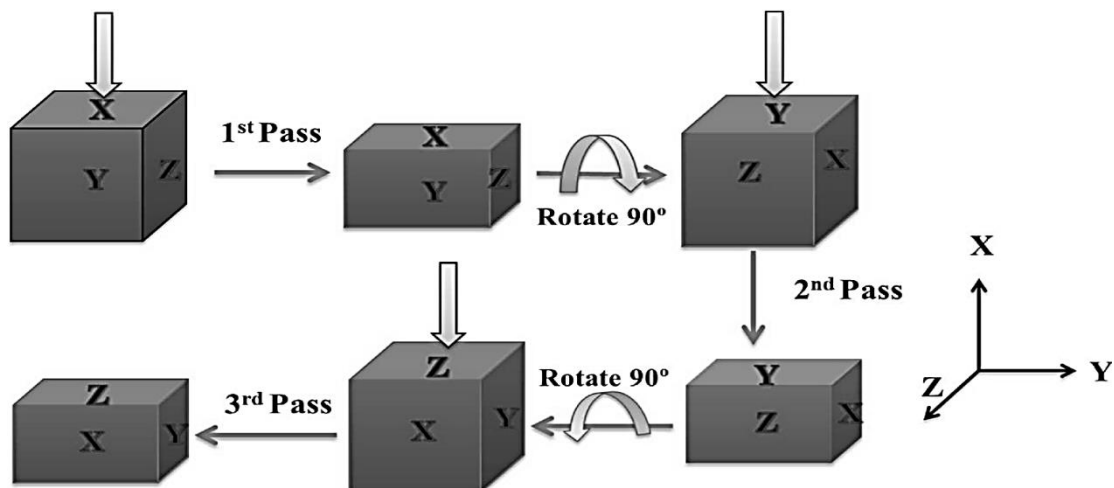


Figure 7.1 MDF (Ramesh et al. 2019)

Multi directional forging is a severe plastic deformation process developed in late 1980s. In this process, the material is uniaxially compressed repeatedly in three

orthogonal directions with 90° rotation before each pressing. The process is schematically represented in Figure 7.1. MDF may be performed in an open die or closed die. Although, load required for compression ratio is less in open die. Disadvantage of open die process is that, during each pass, material tends to bulge which leads to non-uniform loading. Also, flat surface is required for next pass, and hence arising a need for grinding off the bulged material before next pass. These difficulties can be avoided by using a closed die for MDF. Closed die also enables an increased plain strain than strain produced during open die compression for same reduction ratio.

7.1.2 Accumulative Roll Bonding (ARB)

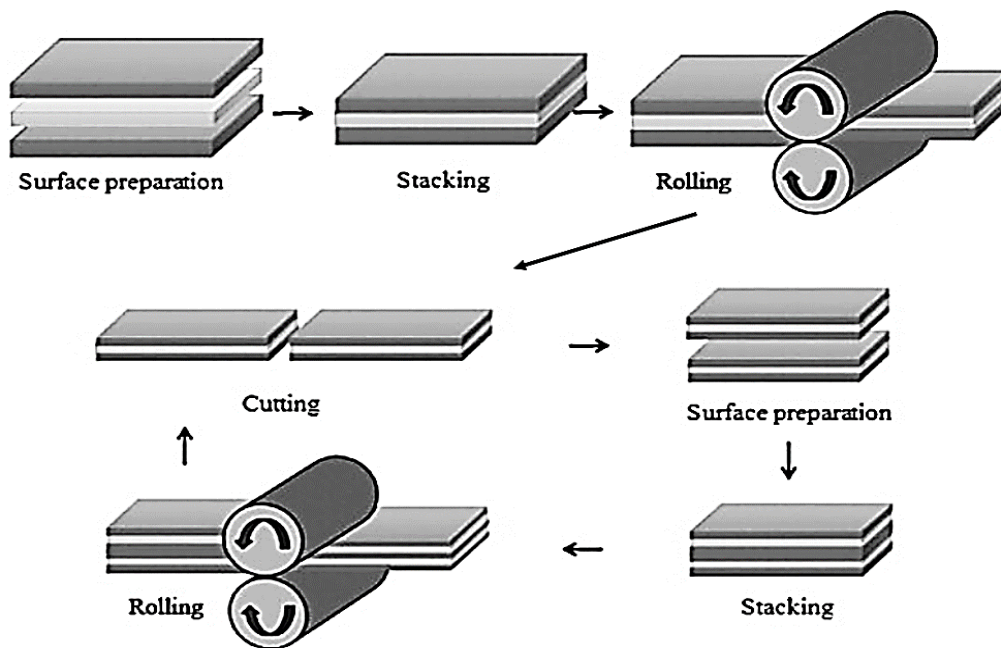


Figure 7.2 Schematic representation of Accumulative Roll Bonding setup (Mehr et al. 2015)

Accumulative roll bonding is a method of producing Ultra fine grains in sheets of metals. In this method sheets metals are stacked one above the other and rolled using a rolling mill with the high reduction ratio. The rolled product is then cut in to half and stacked one over the other to be roll again to produce multi-layered material. By multiple pass ARB Ultra fine grain structure can be obtained. The process has been

schematically being represented in Figure 7.2. Proper surface preparation is required for the bonding of the sheets to take place.

After each pass, when reduction ratio is 1:2, thickness of a layer of sheet (t_n) is calculated as

$$t_n = t_i/2^n \quad (2)$$

Where t_i is the initial thickness of the sheet, n is the number of ARB pass.

After n cycles, total reduction is

$$r = 1 - 1/2^n \quad (3)$$

Hence the equivalent plastic strain is $\epsilon_T = 0.8n$.

The problem with accumulative roll bonding process is that cracks may occur at the free edges of the material at high strain. Also, to form good bond between the materials high reduction ratios are required which require high capacity rolling mills. Moreover, performing the rolling at lower temperature will result in a material with low ductility and poor bond strength (Faraji et al. 2018).

7.1.3 High-Pressure Torsion (HPT)

High-pressure torsion is a process where the material, in the form of a disc, is subjected to compression load, as well as, torsion load at the same time. Material is held between a fixed support and a rotatable lower anvil. Upper anvil and lower anvil together constrains all movement of material. Upper anvil moves towards lower anvil and applies a compressive load on material which is in the range of Giga Pascals. Lower anvil is rotated by a predefined angle to produce torsional load on the material (Figure 7.3). Because of the frictional force between the intersecting surface of upper anvil, material and lower anvil, both loads together create shear strain in material, causing grain refinement, which is found to vary from centre of the disc to the outer edge.

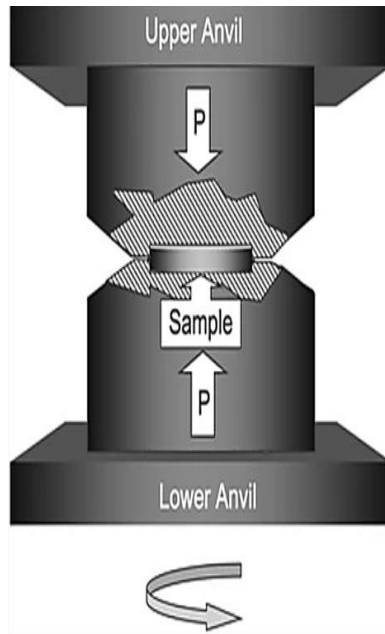


Figure 7.3 Schematic representation of High-Pressure Torsion setup (Xu et al. 2008)

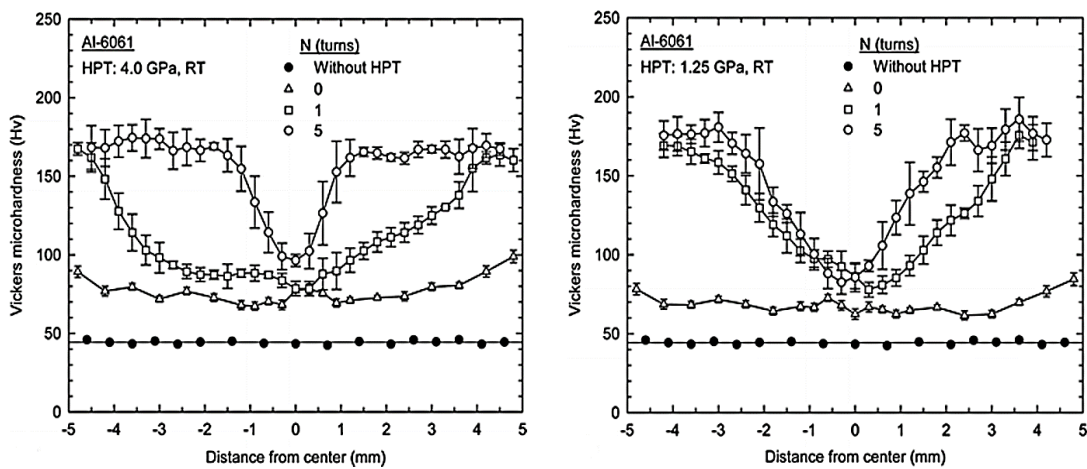


Figure 7.4 Variation in the hardness along the length of Al6061 subjected to HPT (Xu et al.

The shear strain(γ) induced in the material is calculated by

$$\gamma = 2\pi rN/l \quad (4)$$

Where r is radius, N is number of turns, l is the thickness of the material (Xu et al. 2008). Hence, strain induced at a point depends on its distance from the center of the disc. Hence, there is variation in properties from the center of the disc to outer edges.

Figure 7.4 shows the variation in hardness along the length of Al-6061 disc subjected to HPT for different numbers of rotation. It is to be noted that as the applied pressure increases from 1.25GPa to 4GPa, hardness value becomes more homogeneous.

7.1.4 Equal Channel Angular Pressing (ECAP)

ECAP is an extrusion process introduced during 1970s and 1980s (Zhou et al. 2021). It gained popularity among researchers during 90s and is still in active use. Basic intention of this process is to introduce strain in the material and causing work hardening of the material which improve the property of the material. Advantage of this process over other formation processes like forming, extrusion, rolling and drawing processes is that the initial material and the processed material have the same cross-sectional area and strain is introduced without any change in dimensions of material. Also during extrusion, small defects like voids, porosity and blow holes are rectified. Figure 7.5 depicts the schematic representation of the ECAP process.

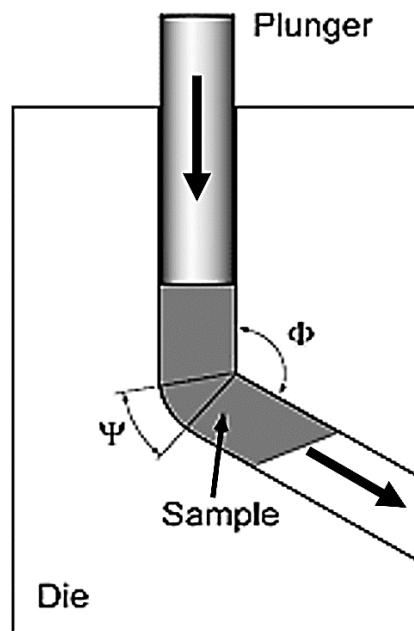


Figure 7.5 Schematic representation of ECAP process

In ECAP, sample is passed through a channel which is bent at an angle ϕ . As the sample passes through the bend, shear strain is introduced (Figure 7.5), which causes grain refinement. As there is no change in cross section of the sample, same sample can be passed multiple times through the die with minimum specimen preparation between passes. With multiple pass ECAP, ultrafine grains can be formed in the sample.

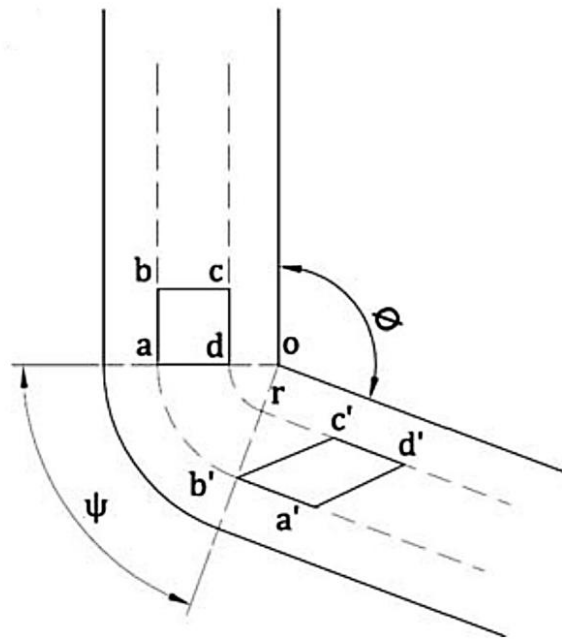


Figure 7.6 Sheared element formed during ECAP process (Kapoor 2017)

Equivalent strain after N passes ϵ_N was expressed in general form as (Kapoor 2017)

$$\epsilon_N = \frac{N}{\sqrt{3}} [2 \cot(\Phi/2 + \Psi/2) + \operatorname{cosec}(\Phi/2 + \Psi/2)] \quad (5)$$

Where the angle ψ and Φ are shown in the Figure 7.6.

When $\psi = 20^\circ$ and $\Phi = 90^\circ$ the effective strain is found to be 1. That is during multi pass ECAP process the effective strain after N number of passes is equal to N .

As cross section of the material remains constant throughout the ECAP process, the sample may be rotated between two successive passes along the longitudinal axis. If no rotation is performed between the two successive passes, the material is said to be

processed in route A. If the specimen is rotated by 90° in the same direction, between successive passes, then sample is said to be processed in route B_C . If specimen is rotated by 90° in alternative direction during the successive passes, specimen is said to be processed by route B_A . If the sample is rotated by 180° between successive passes, processing route is called route C. Different shear planes formed during ECAP along each of the routes are schematically represented in Figure 7.7(c).

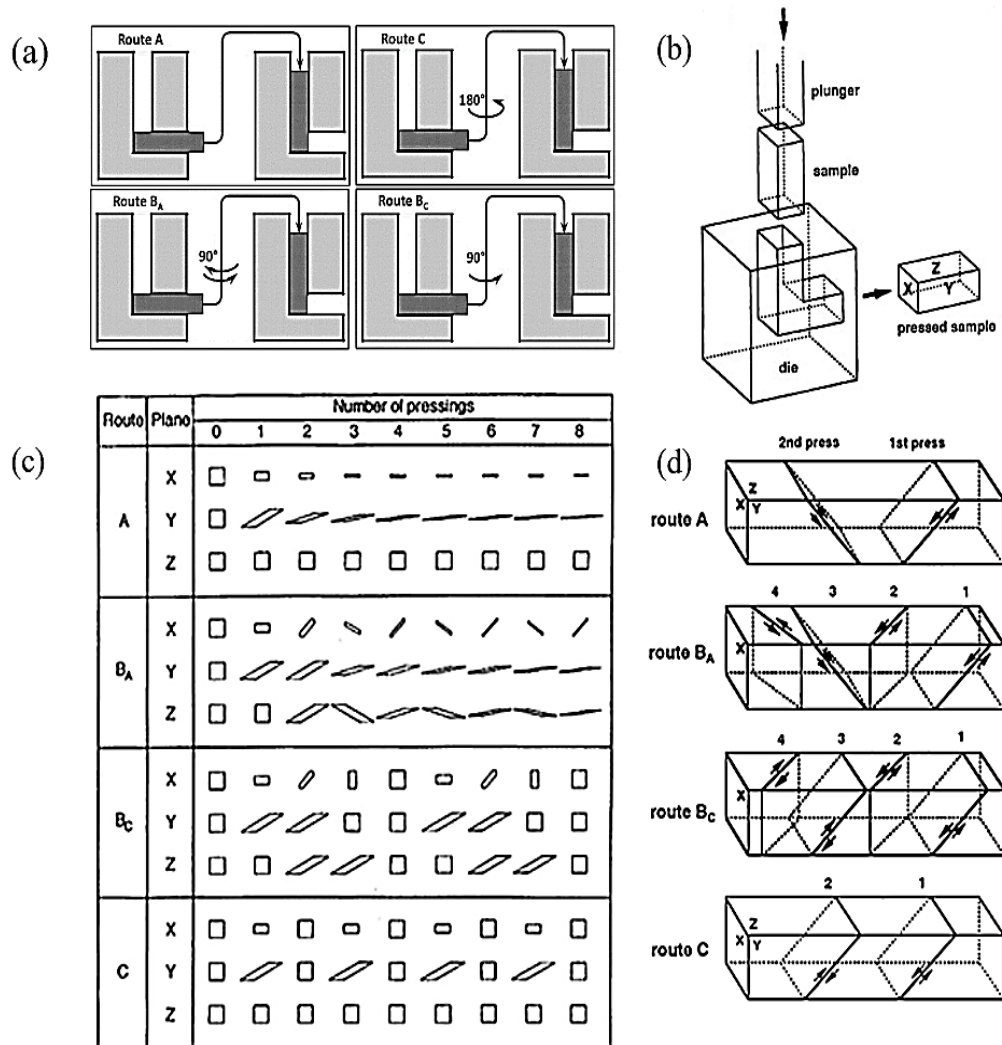


Figure 7.7 Shear plane formed during ECAP along different routes (Valiev and Langdon 2006)

7.2 Copper and Copper alloys

7.2.1 Copper

Copper is a chemical element which has chemical formula Cu. (Latin: cuprum). Copper being one of the very few metals that is found in nature, in a directly usable form, was used from, as early as, 8000BC. Copper has an atomic number of 29, melting point 1080°C. It is a soft, ductile, malleable, thermally and electrically conductive material. These properties make it an ideal material for electrical and thermal conductive and structural applications. Copper has found its place in application from as small as a printed circuit boards to as big as statue of liberty in USA.



Figure 7.8 Applications of Copper and Copper alloys

7.2.2 Physical properties

Copper is a group 11 element in the periodic table (Figure 7.9). Like other elements of group 11, gold, silver and Roentgenium, copper has only 1 electron in s-orbit, which is over the completely filled d-orbit. Half-filled s-orbit enables copper to form metallic bond with other materials. Unlike metals with half-filled d-orbit, copper exhibits very less covalent nature and hence forms a weak bonding. This explains the reason for

copper's low hardness and high ductility. Copper has Face Centered Cubic (FCC) crystal structure. At macroscopic level, hardness of the material can be improved by restricting the movement of lattice structure by introducing defect in lattice structure. This can be done by strain hardening, alloying and precipitation hardening methods.

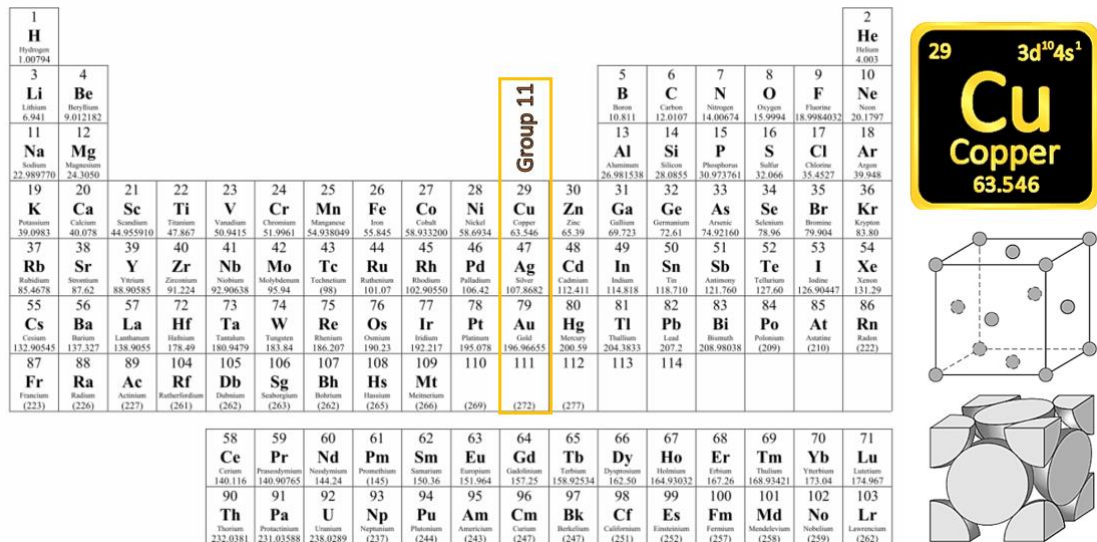


Figure 7.9 Periodic table and atomic properties of copper

7.2.3 Copper alloys

Copper forms an alloy with numerous other elements, and are depicted below

- **Brass** an alloy of copper and zinc, widely used for its bright appearance, low melting point, high workability, high corrosion resistance and low friction and is used in hinges, musical instruments, zippers, gears, locks etc.
- **Bronze** an alloy of copper and tin, was the hardest material known to people in history. Bronze age marks the era of extensive use of bronze in ancient civilizations for weapons, armors, building material. Present age bronze is used in springs, clips, electric connectors for its superior toughness. Used in hammers, wrenches and other tools, because they (beryllium copper) produce no spark when hit against a hard surface, making them ideal tool in explosive environments.

- Copper is also used in jewelry industry, to be alloyed with silver or gold, to enhance the strength for the jewelry.
- Copper and nickel have similar atomic numbers, hence atomic size of copper and nickel are nearly same. Also, nickel is completely soluble in copper producing single phase alpha structure. Cu-Ni alloys are well known for their superior corrosion resistance in moist air and steam condition and are excellent at stress corrosion cracking resistance. They possess moderate strength and thermal stability. They have inherent resistance to biofouling and are easily fabricated. Most common composition of Cu-Ni are 90/10 and 70/30.

7.3 Some important literature on C70600 alloy

(Ardy et al. 2021) studied corrosion in 90-10 Cu-Ni alloy immersed in 10% ammonia, 10% Na₂S, and the mixture of ammonia and Na₂S solutions under 3 different tensile loading conditions. After 15 days of immersion in different solutions, corroded compounds formed on Cu-Ni alloy were found to be Cu(OH)₂, Cu₂S, and copper ammonium ion complex. It was found that stress corrosion cracking (SCC) was in the initial stage, where slip dissolution was observed along with pitting and intergranular corrosion. It is to be noted that tensile stresses induced in the material did not affect corrosion rate.

(Suganya Priyadharshini et al. 2017) attempted to produce Surface Metal Matrix Composite (SMMC) of C70600 alloy and ZrC particles, using friction stir (FS) process. The composite produced homogenous particle distribution and good bonding between the reinforcement and matrix. There was 28% increase in hardness and 2% increase in tensile strength compared to friction stir processed C70600 alloy without reinforcement.

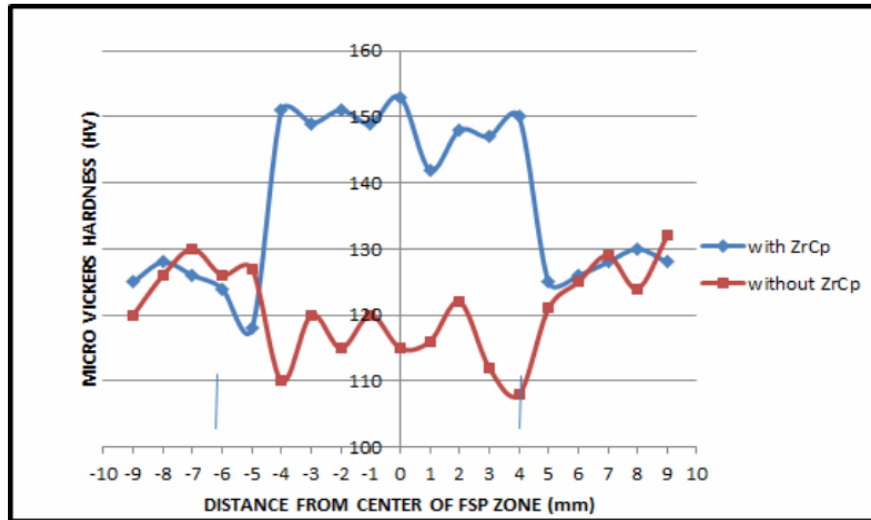


Figure 7.10 Microhardness distribution across the stir zone of FS processed CuNi with and without addition of ZrCp. (Suganya Priyadharshini et al. 2017)

Ultimate tensile strength (UTS) increased but ductility reduced as ZrC particles are brittle and presence of ZrC particles act as stress concentration points and reduce redistribution of stress during yielding. This caused formation of micro-voids between ZrC particles and matrix leading to plastic deformations during uniaxial tensile loading. Hardness distribution along friction stir processed zone with and without addition of ZrC is shown in Figure 7.10. Annealing effect and grain coarsening at friction stir processed area decreased the hardness of the material when ZrC particle were not added.

(Chung et al. 2018) studied welding of two C70600 alloy plates by Friction Stir Welding (FSW) followed by Gas Tungsten Arc Welding (GTAW). FSW caused crushing and stirring of oxides present in the base metal at stir zone (FSW-SZ) which was seen a black-arc-arrays in microstructure. This mixing of oxide in the weldment caused the material to fail during tensile and bend tests. UTS of FSW joint was found to be 317MPa which was similar to GTAW joint. GTAW caused these mixed oxides to re-gasify oxygen causing pores in the regions of GTAW weld metal.

(Faeghfar et al. 2019) investigated dissimilar metal welding of C70600 with AISI 304 L austenitic stainless steel using Tungsten-Gas Arc welding with ERNiCr-3 as filler.

ERNiCr-3 produced austenitic microstructure with longer dendrites formation when welded in non-pulse mode. During tensile testing, the welded sample fractured at the interface of filler material and C70600 in ductile manner. This interface showed increased grain size at the interface of filler material and stainless steel.

(Biglari et al. 2014) investigated the effect of annealing time, tool rotation speed on mechanical and microstructural properties of friction stir welded C70600 alloy. It was found that annealing of FS welded C70600 had a great impact on tensile strength and hardness of weldment. Longer annealing time and lower tool speed produced finer grains at nugget zone. This resulted in increase in hardness and tensile strength of the material.

(Lee 1983) investigated various organic and inorganic chemical pretreatment of C70600 alloy to reduce initial corrosion rate by restricting copper discharge during initiating of new condenser. Pretreatment for 1 hour in 2% Sodium dichromate solution at 50°C could reduce initial Cu ion discharge into seawater from condenser up to 10 folds. Pretreatment with sodium dichromate did not affect other properties of C70600 alloy, like bio-fouling resistance and erosion-corrosion resistance. Figure 7.11 shows the polarization curve of treated and untreated C70600 alloy in aerated seawater at 50°C.

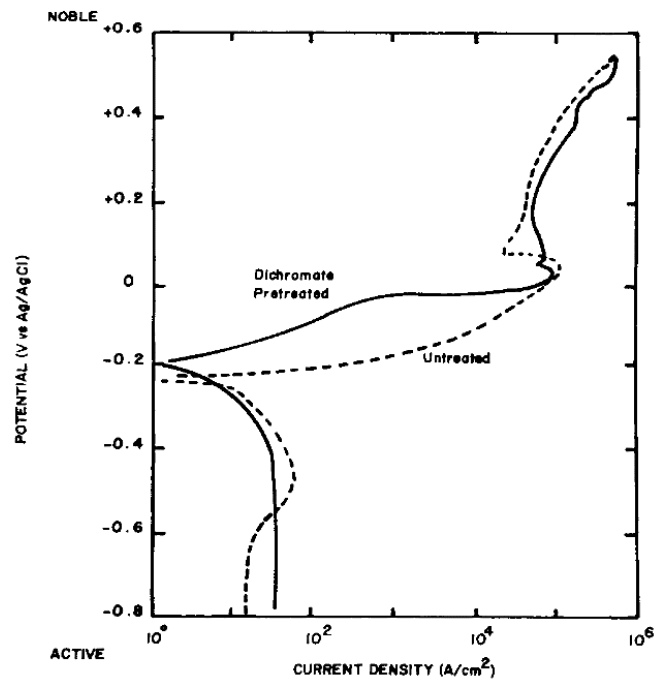


Figure 7.11 Anodic and cathodic polarization curves in aerated seawater at 50 °C for sodium dichromate pre-treated C70600 (2%, 1 hour at 50 °C) as compared to untreated C70600 (Lee 1983)

(Schleich 2004) provided the evaluation on optimum and critical operating conditions for ensuring successful application of CuNi 90/10 alloy in seawater piping applications. Metallurgical design and fabrications considerations were provided to prevent occurrence of erosion-corrosion and corrosion damage in polluted water. In addition, a compiled report on measures to be taken for commissioning, starting up, shutting down of operations to enable establishment and re-establishment of protective layer in the pipelines are provided.

H. Ezuber and A. Al Shater (Ezuber and Shater 2015) investigated the effect of environmental parameters like carbon dioxide, oxygen and chloride concentration and temperature in the corrosion behavior of CuNi 90/10 alloy. Tests have revealed an increase in chloride corrosion rate with increase in temperature and decrease in CO₂ concentration. Corrosion potential of alloy shifts to negative direction, with aeration of chloride-CO₂ solution. Pitting corrosion was seen on the surface exposed to chloride

solution with or without the presence of CO₂. Hemispherical pits formed on the surface were deeper with the presence of CO₂.

Al-Odwani et al. (Al-Odwani et al. 2006) studied corrosion resistance and performance of UNS C70600, C71500 and titanium-based UNS R50400 alloys in heat recovery section of multistage flash (MSF) distillation plants. C70600 alloy showed (Figure 7.12) highest corrosion rate during the initial phase of the test and gradually reduced up to 150 days. By then a greenish corrosion product was formed on the surface that prevented further corrosion and acted as a barrier reducing corrosion rates thereafter. The corroded surface showed the presence of Cl, Si and O.

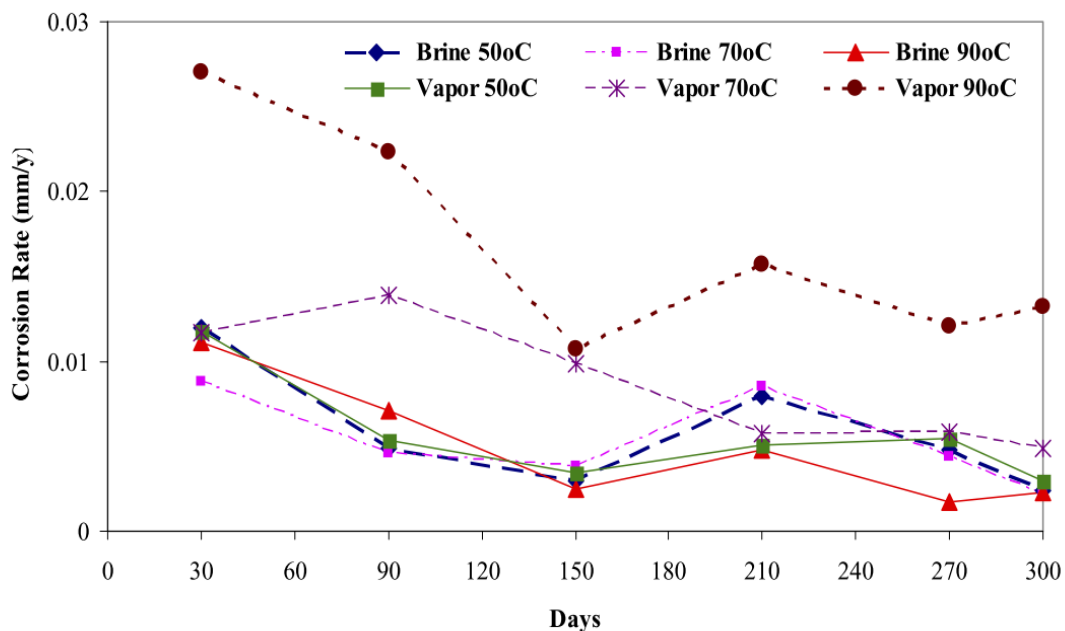


Figure 7.12 Corrosion rate of C70600 exposed to different corrosive medium over different range of time (Al-Odwani et al. 2006)

Yang et al. (Yang et al. 2018) studies the effect of aluminum concentration in mechanical and electrochemical corrosion properties of Cu-Ni-Fe-Mn alloy. Alloy with 3 wt. % Al showed highest tensile strength of 395 MPa. Addition of Al decreased corrosion resistance of the material over 3wt %. Addition of Al resulted in formation of compact oxide protective film on surface that prevented further corrosion, but

existence of a potential difference between precipitated phase and substrate hindered corrosion resistance of the material.

Taher et al. (Taher et al. 2007) studied corrosion properties of C70600 alloy in natural seawater and artificial seawater with different sulphate concentrations at room temperature. Study, based on different electrochemical techniques, could conclude that corrosion resistance properties of the alloy was highly depended on sulphate concentration in the electrolyte. It was concluded that 2,260 ppm of sulphate in artificial saline solution produced results close to corrosion characteristics of commercially available C70600 alloy in natural seawater.

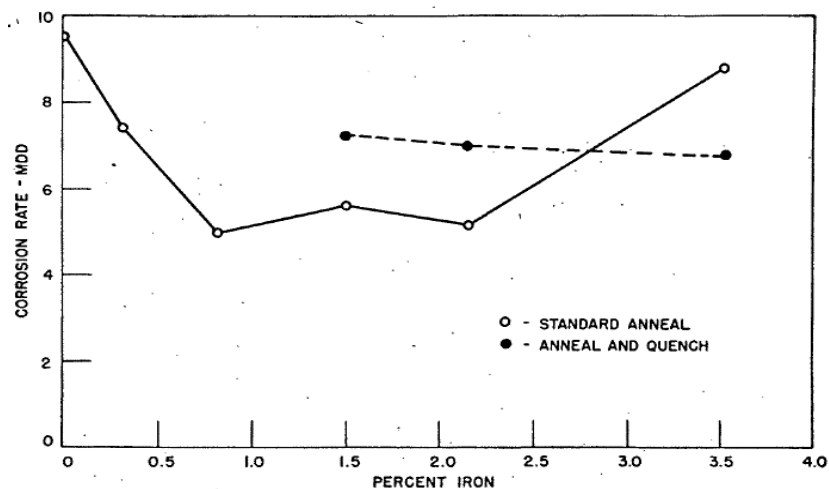


Figure 7.13 Effect of iron concentration on the corrosion rate of C70600 alloy when exposed to sea water for 300 days (Stewart and LaQue 1952)

Stewart and LaQue (Stewart and LaQue 1952) studied corrosion behavior of iron modified CuNi 90/10 alloy, when iron exceeded solubility limit and precipitated to form iron rich precipitate from solid solution. When the alloy was held at 600°C after quenching from 900°C, precipitation of iron rich precipitates, only visible under higher magnification of SEM, was observed. These showed a change in color when annealed at 750°C. Figure 7.13 shows the effect of iron concentration on corrosion rate of C70600 alloy, exposed to sea water for 300 days for annealed quenched to 600°C specimen and normal specimen .

H. M. Ezuber (Ezuber 2015a) studied the effect of thiosulphate addition (one of the major sulphide oxidation products in seawater), to corrosion medium, on corrosion rate of CuNi 90/10 alloy at different temperatures. It was found that rate of corrosion increased with increase in temperature. Also rate of corrosion correlated with change in free corrosion potential to negative direction. Addition of thiosulphate increase the rate of corrosion. It was seen that, with addition of thiosulphate, at higher temperatures, formation of protective film was interfered and a black film was formed, which reduced the alloy corrosion rate.

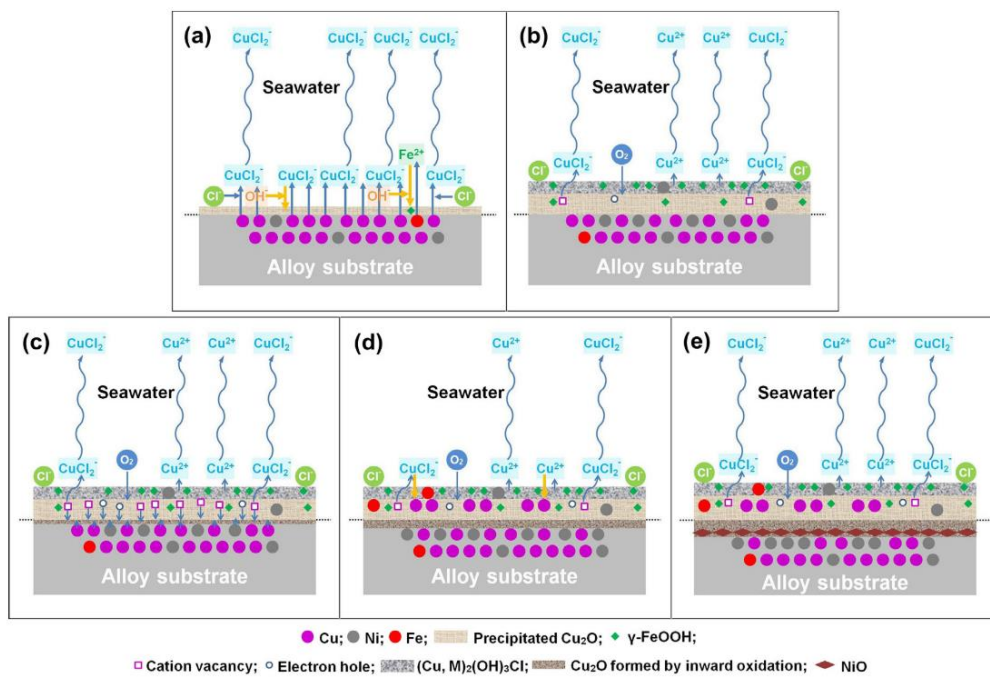


Figure 7.14 schematic representation of steps involved in formation of corrosion layer for Cu-Ni 90/10 alloy (Ma et al. 2015)

Ma et al. (Ma et al. 2015) studied the composition and structure of corrosion components formed on CuNi 90/10 alloy, when immersed in seawater for 30 days. Studies showed formation of 3 layers of components in corrosion product. Outer, middle and inner layers are enriched with Fe (γ -FeOOH and metallic Fe), copper and Ni (NiO/Ni(OH)_2 and metallic Ni), respectively, which provides superior corrosion resistance to the sample. Figure 7.14 represents the steps involved in formation of

corrosion film in CuNi 90/10 alloy during immersion in sea water. During initial stage, Cu dissolution takes place with formation of CuCl_2^- and precipitation of Cu_2O . Oxidation of Cu_2O takes place along with formation of $\text{Cu}_2(\text{OH})_3\text{Cl}$. Further, because of corrosion, Cu_2O film is developed along with the formation of cations and electron holes. During the next stage, thickness of Cu_2O increase along with deposition of pure Cu grains. During the final stage, formation of NiO takes place in the inner layer of the film along with thickening of Cu_2O film.

A M Taher et al. (Taher et al. 2011) investigated the effect of iron concentration in corrosion resistance behaviour of Cu-Ni 90/10 alloy in saline water and natural sea water. Alloy with higher concentration of Fe showed better electrochemical behaviour after quenching. Addition of Fe reduced porosity in corrosion film formed on the alloy after exposure to saline and natural sea water. When exposed to medium containing sulphur, corrosion products formed contained FeS and NiS. In the absence of Sulphur, in corrosion medium, corrosion film mainly contain chlorides and Fe_2O_3 .

Eiselstein et al. (Eiselstein et al. 1983) studied the effect of sulphur concentration on corrosion rate of CuNi 90/10 alloy by exposing the alloy to alternate aerated Sulphur polluted sea water, de-aerated unpolluted with Sulphur sea water and de-aerated unpolluted with Sulphur sea water (Figure 7.15). It was found that the alloy had lower corrosion rate when the polluted sea water was de-aerated than when the sea water was aerated. Significant increase in localized corrosion was noted in sample exposed to aerated Sulphur polluted sea water. It was seen that the material corrosion rate reduced when the material was first exposed to aerated unpolluted seawater before exposure to aerated polluted seawater. This showed that the protective film formed during exposure to unpolluted seawater provided protection when exposed to Sulphur polluted seawater.

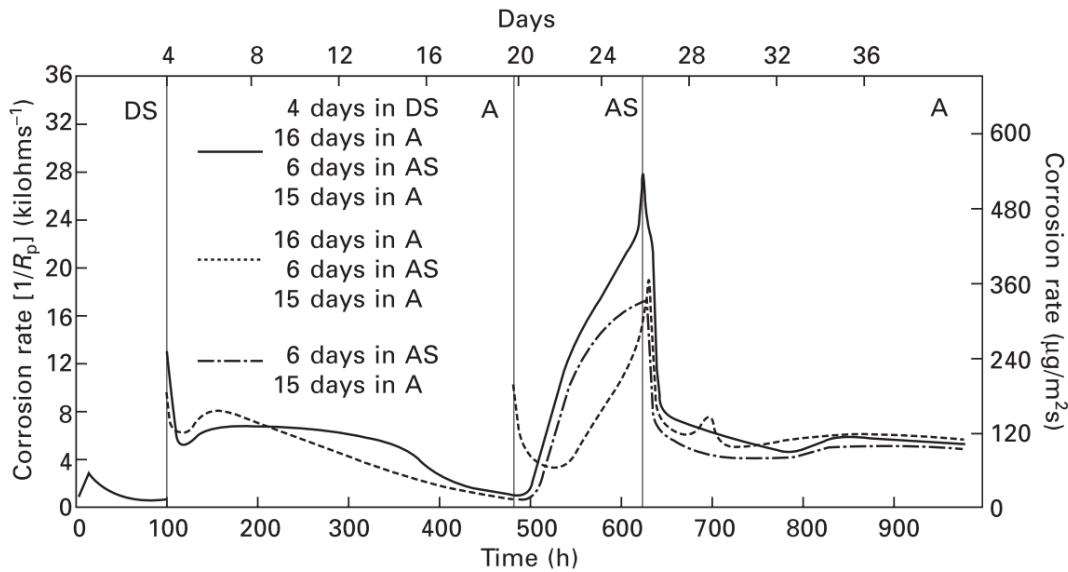


Figure 7.15 Corrosion rates of CuNi 90/10 in flowing seawater showing the effect of exposure history and seawater chemistry: DS – de-aerated and sulphide-polluted ($0.05\text{--}0.1\text{ g/m}^3\text{ O}_2$, $0.2\text{--}1.3\text{ mg/l HS}^-$);

A – aerated unpolluted ($6.6\text{ g/m}^3\text{ O}_2$);

AS – aerated and sulphide-polluted ($0.1\text{--}0.3\text{ g/m}^3\text{ O}_2$, $0.4\text{--}1.6\text{ mg/l HS}^-$) (Eiselstein et al. 1983)

R. F. North and M. J. Pryor (North and Pryor 1970) found that the structure of protective layer formed on the CuNi alloy. It was seen that the major composition of the protective layer was of Cu_2O with cuprous hydroxychloride [$\text{Cu}_2(\text{OH})_3\text{Cl}$] and cupric oxide (CuO) being present. It was seen that the thickness of the protective layer ranged upto 2800 \AA for copper to 4400 \AA for C70600 alloy. The film was basically found to be adherent, protective and generally brown or greenish brown in color.

H. M. Ezuber (Ezuber 2014, 2015b) investigated the effect of iron content in the CuNi 90/10 subjected to 3.5% NaCl stagnant and flowing corrosive environment at different temperatures. It was found that with increase in percentage of iron in the alloy increase the corrosion rate in all the conditions. With increase in iron more than 2 wt. % of the alloy there was a significant change in open circuit potential. This change in corrosion resistance with increase in iron content is found to be because of iron rich precipitate that are detrimental in production of corrosion resistance film when exposed to

corrosive environment. There was a significant shift in open circuit potential to the negative side with increase in temperature and flow rate.

A. H. Tuthill (Tuthill 1987) studied the corrosion behavior of C70600 alloy in different sea water conditions. Figure 7.16 shows the rate of corrosion in CuNi alloy when exposed to different seawater conditions. It is seen that the rate of corrosion is highest in flowing water and least in quite waters. It was also seen that the rate of corrosion reduces significantly with increase in exposure time in each case.

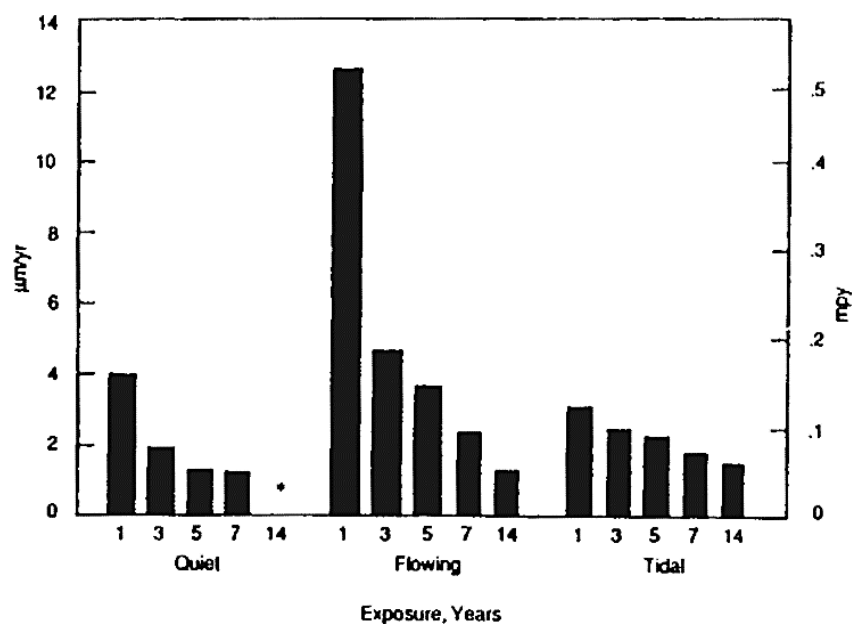


Figure 7.16 Corrosion rates for Alloy C70600 for long term seawater exposures (Tuthill 1987)

Gopi et al.(Gopi and Shivananda Nayaka 2017a; b; Praveen et al. 2018) worked on the AM series magnesium alloys, which were processed using ECAP along route B_C and analysed for microstructure and mechanical strength. After four passes, the grain size decreased from 100 μm for as-received to 1 μm after 4 ECAP passes. Due to ECAP processing, the results of the EBSD investigation showed a change in the misorientation angle and the presence of high angle grain boundaries. Samples with the highest tensile strength after two ECAP runs had strengthened grain boundaries. Strength was lowered at higher ECAP passes due to dynamic recrystallization. Wear studies showed a decline

in the coefficient of friction along with an increase in the number of ECAP passes, which was in correlation with the hardness test.

Kim et al.(Kim et al. 2012) improved the mechanical properties of Cu-40%Zn alloy by ECAP process in route C was at a temperature of 250°C. Heat treatment for recrystallization was applied for 20 minutes at 350 °C. Vickers microhardness, electron backscattered diffraction, and tensile tests were utilised to assess the grain boundary character distributions and mechanical characteristics of ECAP materials. Grain refinement increased noticeably with further ECAP runs, going from 13µm in the original sample to 300 nm after 4 passes. In addition to maintaining a more refined grain size than that of the initial condition, the post-heat-treated material following ECAP also increased tensile strength without reducing elongation.

Ni et al. (Ni et al. 2016) tried to improve the mechanical properties of pure copper used in electrical application by making a metal matrix composite with TiC particle and then extruding the composite through an ECAP die. The mechanical characteristics of the as-cast alloy were judged inadequate since fine TiC particles were in the as-cast Cu matrix in clustered form. The as-cast alloy's grains were greatly uniformly distributed by continuing ECAP at 473 K. The ECAP-processed alloys retained good conductivity with noticeably increased tensile strength and hardness values thanks to the multiple pass ECAP process. The fine-grained copper alloy's elongation and conductivity increased with the appropriate tensile strength after post-ECAP annealing. The new combination method gives the alloy the performance it needs to work with the existing high-frequency electrification systems for railways.

7.4 Research Gap

From the extensive literature survey, it was found that huge quantities of C70600 is used in marine structural application every year. By enhancing the mechanical properties of the material, the quantity of the material required to withstand the same load maybe reduced. Severe plastic deformation (SPD) is promising technique to improve the mechanical properties of the material by introducing strain hardening in the material. Equal channel angular pressing (ECAP) is one of the SPD methods that allows strain hardening in bulk material without changing the cross section of the

material. Also, it is seen that the process is repeatable and it enables accumulating of strain in the material during each pass. From the literature survey it was seen that, literatures available are focused on studying the effect of different corrosion environment on the corrosion properties of the material, study of corrosion products formed on the surface, surface properties enhancement by fabricating surface metal matrix composite. There are literatures on weldability of the material with similar and dissimilar materials as well. No literature is available on improving the mechanical properties of the bulk C70600 alloy. Objectives of the present work focuses on improving the mechanical properties of the C70600 alloy by subjecting the material to ECAP. The mechanism of grain refinement and correlation with the mechanical properties is discussed in this work. An elementary corrosion study is also made to ensure that there is no significant reduction in corrosion resistance of the material after the ECAP process.

7.5 Objectives of Research

Based on the available literature review and the gaps in literature, following objectives have been formulated and are listed below. The main objective of the research work is to perform SPD process, to improve mechanical and corrosion properties of CuNi alloy.

- Microscopic investigating on ECAP processed sample to investigate the effect of grain refinement.
- Mechanical characterization on ECAP processed sample to investigate the effect of multiple pass SPD process.
- Study the effect of SPD process on corrosion property of the material.

CHAPTER 8 EXPERIMENTAL PROCEDURE

The equipment and setups used in the research work are explained in the present chapter.

8.1 Flow chart

Flow chart in Figure 8.1 shows the experimental steps and characterization techniques used in ECAP processing of C70600 alloy. Microstructural characterization is done using optical microscope imaging, scanning microscope imaging, XRD and electron back scatter diffraction (EBSD) techniques.

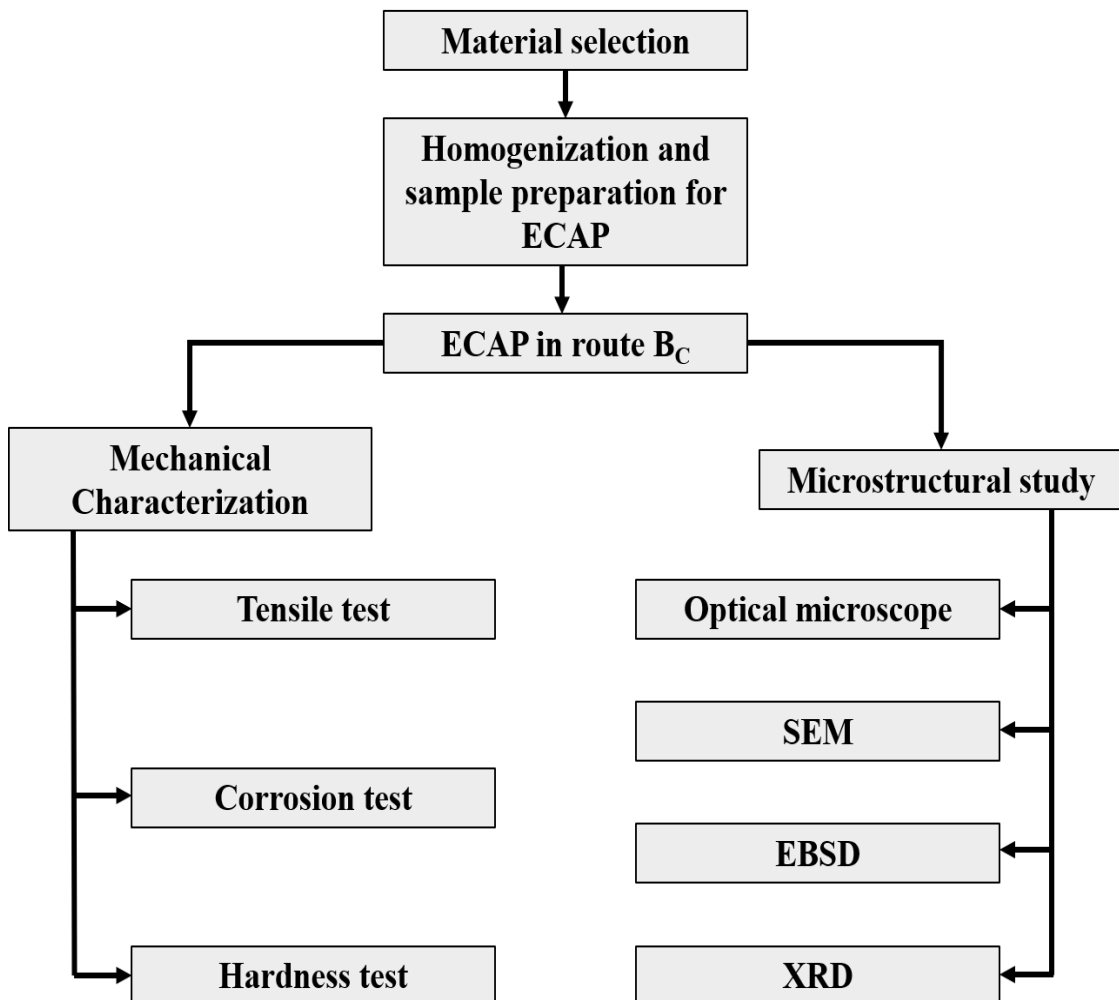


Figure 8.1 Flow chart for experimental procedure followed to conduct the experiments and testing

8.2 Material

Commercially available Copper Nickel alloy, C70600 is used in this research. Material is received in the form of rods. Nominal composition is shown in Table 1.

Table 1 Nominal composition of C70600 alloy

Ni	Fe	Si	Mn	Al	Cu
9.2	2.32	1.01	0.57	0.5	Rem.

As received samples were homogenized at 600°C for 2h followed by furnace cooling. the homogenized samples were turned to rods of diameter 16mm and length 100mm (Figure 8.2). These turned samples were used for ECAP process.



Figure 8.2 Machined sample of C70600 to execute ECAP

8.3 Experimental setup

Following equipment's were used for ECAP processing of C70600 alloy

8.3.1 Universal Testing Machine (UTM)

Pressing was carried out on a 40T Universal Testing Machine setup (Figure 8.3).



Figure 8.3 20T Universal Testing Machine

8.3.2 ECAP die

The die used for ECAP is made of hardened steel. It consists of two internal channel of diameter 16mm and length 100mm intersected at an angle of 110° . Outer edge of intersection is rounded off for an angle of 20° as shown in cross section Figure 8.4(b).

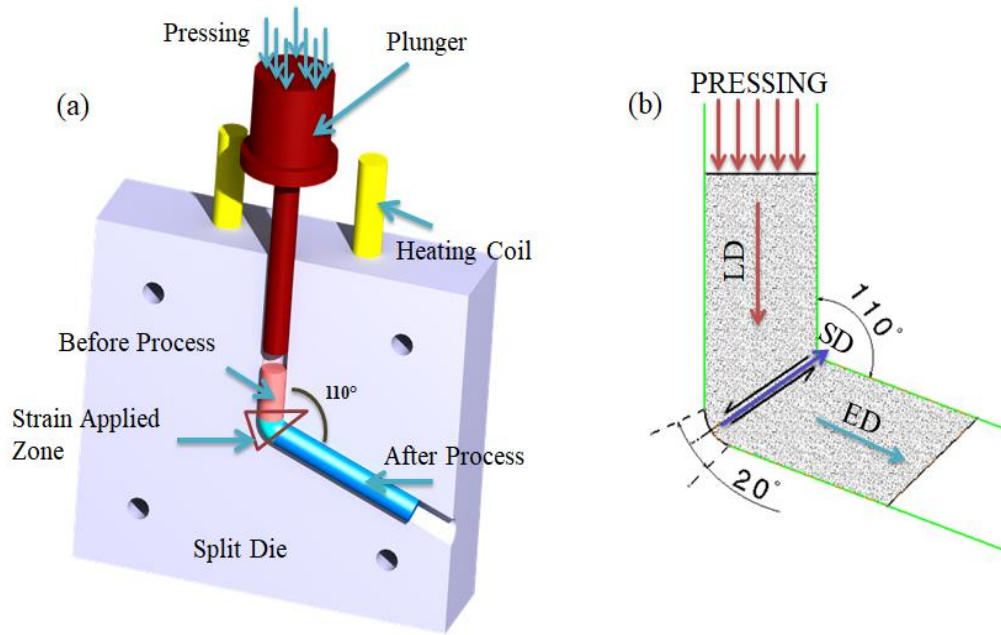


Figure 8.4 (a) Sectional view ECAP split die and plunger, (b) Material flow mechanism during ECAP [1]

Equivalent micro-strain (ε) induced in the sample can be calculated by

$$\varepsilon = \frac{N}{\sqrt{3}} \left[2 \cot \left(\frac{\phi}{2} + \frac{\psi}{2} \right) + \psi \operatorname{cosec} \left(\frac{\phi}{2} + \frac{\psi}{2} \right) \right] \quad (6)$$

Where N is number of ECAP pass, Ψ and Φ are angle of intersection of channels and outer radius respectively. Based on above Equation 6, micro-strain induced by the die is found to be 0.6347 during each pass. Figure 8.5 shows the split die setup used for the experiment.



Figure 8.5 ECAP Split die

8.3.3 Lathe

Material, after ECAP, is turned to remove head and tail regions before the next ECAP pass. Head and tail regions of the ECAP processed material are not strained like the middle portion hence causing inhomogeneous deformation (Ma et al. 2005; Yoon and Kim 2008).

8.4 Experimental procedure

ECAP was performed at room temperature with ram velocity of 1mm/s. ECAP was performed up to 8 passes using route B_C where the sample are rotated by 90° along the longitudinal axis between passes. Route B_C is proven to produce better equiaxial grain refinement than other routes (Alawadhi et al. 2020b). Molybdenum disulphide (MoS₂) was used as a lubricant during each ECAP pass. Figure 8.6 shows homogenized and ECAP processed sample. After ECAP, split die was open and specimen was removed.



Figure 8.6 ECAP processed C70600 alloy

8.5 Material characterization

ECAP processed sample was characterized by mechanical and microstructural studies. Figure 8.7 shows location of extraction of samples for different characterization tests.

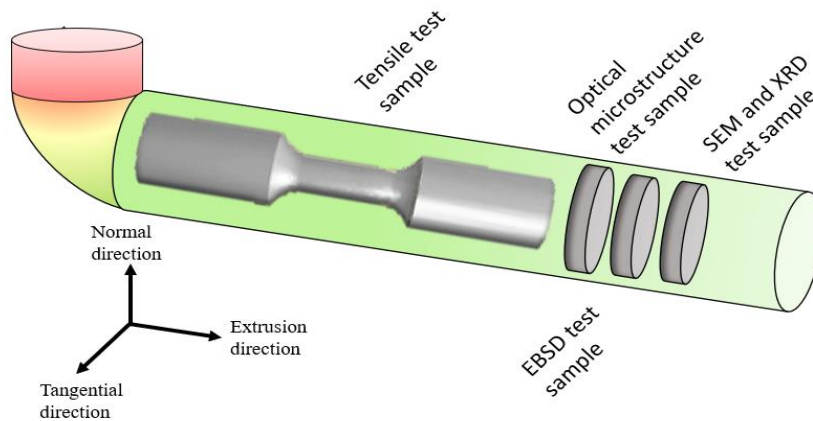


Figure 8.7 Test specimen location

8.5.1 Microstructural characterization

Specimens were extracted from the center of each of the ECAP processed samples for microstructural analysis. Figure 8.7 shows the position of samples taken for analysis.

8.5.1.1 Optical microscope imaging

Specimen for microstructural analysis were polished using emery paper from grade 60 to grade 2500 by manual polishing method. Specimen were then cleaned in acetone and further polished using diamond paste upto 0.5 μ m grade. Samples were polished using diamond paste, on polishing machine METCO. Specimen was cleaned using water and followed by acetone. Cleaned specimens were chemically etched using a freshly prepared solution of 10g $K_2Cr_2O_7$, 2ml HCl, 5ml H_2SO_4 and 95ml distilled water. Etched specimen is observed under optical microscope (Figure 8.8).



Figure 8.8 Optical microscope setup

8.5.1.2 Scanning Electron microscope (SEM)

Microstructural analysis of homogenized and ECAP processed specimens were performed using scanning electron microscope (SEM) of Model JEOL (Figure 8.9). SEM images were used to study microstructure image, tensile test fractured surface and corroded specimen surface morphologies.



Figure 8.9 Scanning electron microscope setup

8.5.1.3 X-ray diffraction (XRD)

X-ray diffraction (XRD) data of ECAP processed specimen and homogenized specimens were capture using Empyrean 3rd Gen, Malvern PANalytical, (Figure 8.10) model using Cu- α radiation. Samples were scanned at a rate of 2° per minute and diffraction angle (2θ) ranged between 30° to 100° .

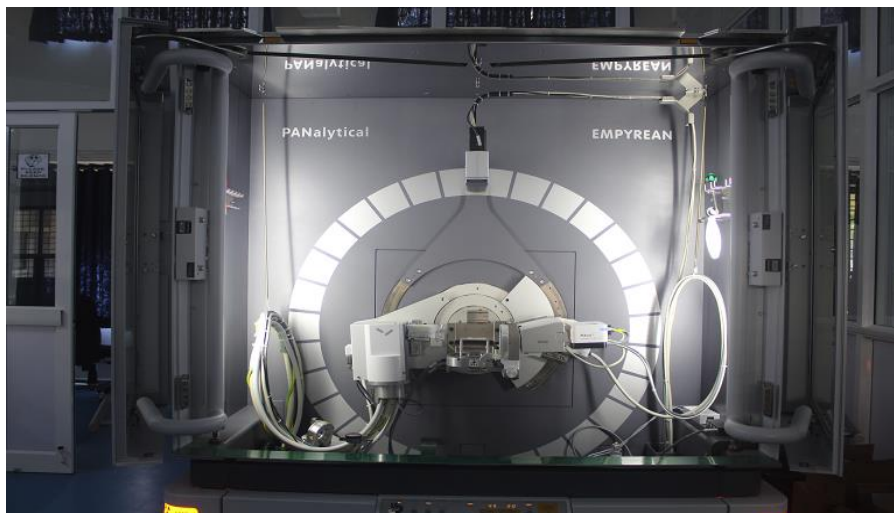


Figure 8.10 X-ray diffraction (XRD) setup

8.5.1.4 Electron Backscatter Diffraction (EBSD)

Grain structure and grain boundary misorientation angles of homogenised and ECAP treated materials were examined using electron backscatter diffraction (EBSD) on a Field Emission Scanning Electron Microscope (Figure 8.11). Middle section of the samples were cut using a diamond wheel cutter and mounted in acrylic powder and acrylic liquid. Mechanical polishing of mounted samples is done with silicon carbide abrasive paper up to 2000 grade. Finally, a 0.5µm diamond paste was used to polish the sample. Additional electro polishing was done to obtain a strain-free surface for Orientation Imaging Microscopy (OIM) analysis. For electro-polishing, a D2 electrolyte solution containing 20% phosphoric acid (H_3PO_4), 50% distilled water, 25% ethanol, propanol 5% was used as electrolyte solution.

EBSD patterns were acquired at accelerating voltage 20 keV with step size of 1 µm and EBSD camera binning mode was 4X4, area of scan was 465 X 347 mm² and Kikuchi patterns were indexed for Cu phase.



Figure 8.11 Electron Backscatter Diffraction (EBSD) setup

8.5.2 Mechanical Characterization

8.5.2.1 Tensile test

Specimens for tensile test were extracted from each of the ECAP processed samples up to 6th pass and homogenized samples. Samples formed after 7th and 8th pass were too small to be turned to tensile specimens that meet the ASTM standards. All the specimens (Figure 8.12) were turned to meet the ASTM E8M standard (Figure 8.13). 3 specimens for each of the ECAP passes were prepared and all samples are subjected to tensile testing and average value was considered. Tensile tests were performed on homogenized and ECAP processed samples using Shimadzu (AG-X plusTM-100 kN) universal testing machine (Figure 8.14). Test was carried out at constant ram speed of 0.5 mm/min at room temperature.

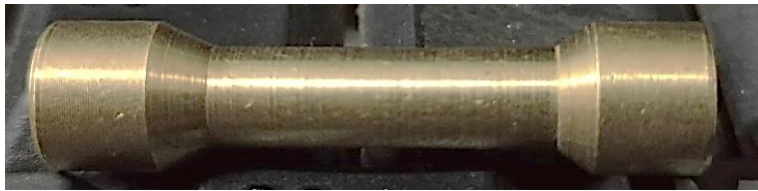


Figure 8.12 Tensile test specimen

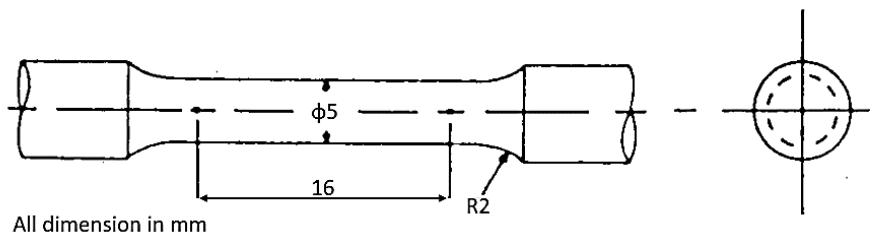


Figure 8.13 Dimensions of tensile test specimen

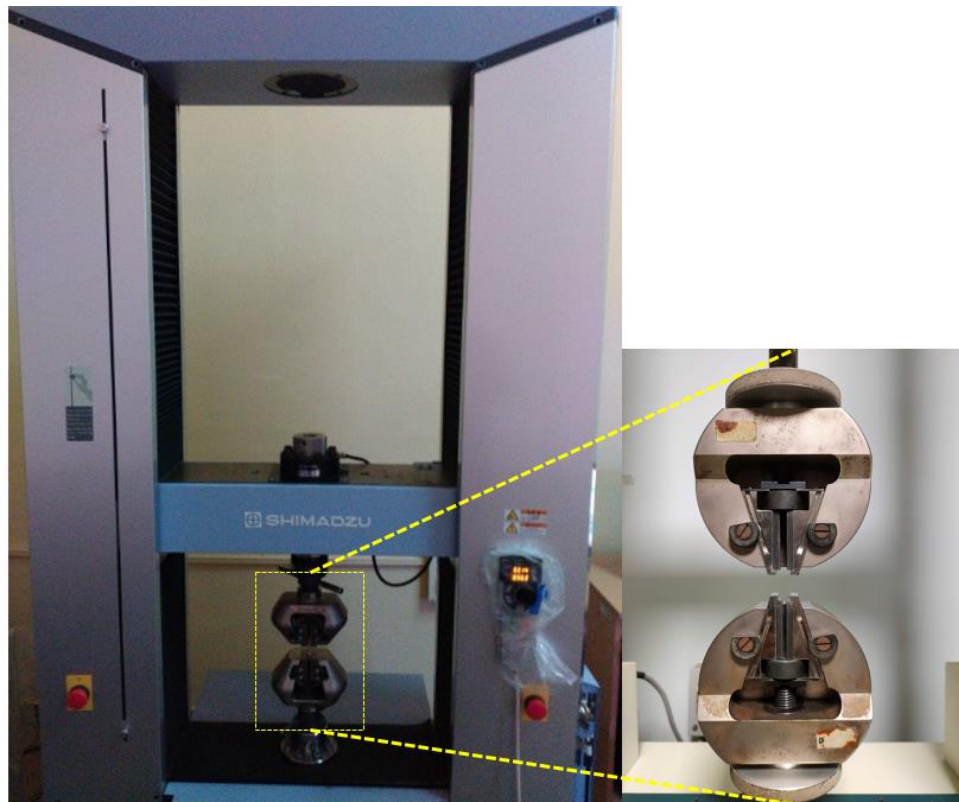


Figure 8.14 Tensile testing machine (Micro Universal Testing Machine)

8.5.2.2 Vickers micro hardness test

Micro hardness value of homogenized and ECAP processed samples were tested using Vickers Tester, Omni Tech, MVH-S-Auto (Figure 8.15). Samples were cut in a direction perpendicular to horizontal direction and polished using emery paper. Cleaned samples were then tested for micro hardness with a load of 100g and a dwell time of 15s. 20 readings were taken for each sample and average was considered.

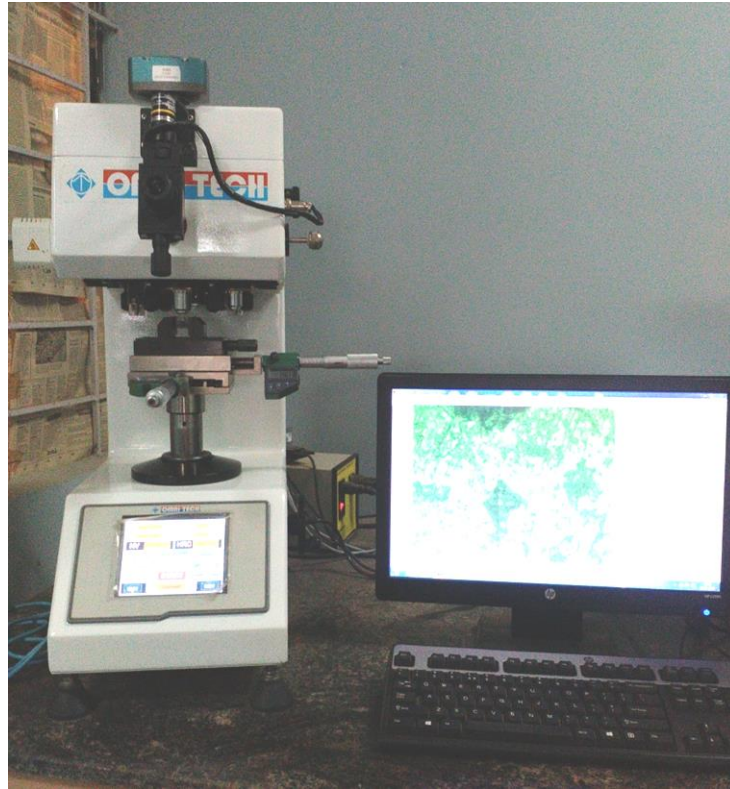


Figure 8.15 Micro hardness testing setup

8.5.2.3 Corrosion test

Specimens used for electrochemical analysis were extracted from center of each of the ECAP processed sample. Each of the specimens were molded to expose only 1cm^2 of the specimen to the electrolyte. The molded specimens were then polished to remove all cracks and produce mirror like finish. Electrochemical measurements were performed using a conventional three-electrode setup (EC lab-Biologic SP-150), with Ag/AgCl as the reference electrode and a platinum wire as the counter electrode (Figure 8.16). Working electrode was the sample with a 1cm^2 surface area exposed to solution. Aqueous solutions of 0.1M, 0.5M, and 1M NaCl were synthesized in distilled water using A.R. grade NaCl, and pH of solution was held at 7.5. Samples were polished using SiC paper before each experiment (400-2000 grade). At a scan rate of 0.5mV/s , potentiodynamic polarisation tests were performed. Corrosion potential (E_{corr}) and corrosion current density (i_{corr}) were calculated using Tafel plots for cathodic and

anodic parts. Electrochemical impedance spectroscopy (EIS) measurements were performed at frequencies ranging from 100 kHz to 10 mHz, using a sinusoidal potential signal amplitude of 5 mV. Surface morphology of corroded samples was investigated using an optical microscope and a scanning electron microscope.



Figure 8.16 Corrosion test setup

CHAPTER 9 RESULTS AND DISCUSSION

This chapter provides the results of mechanical and microstructural study performed on ECAP processed Cu-Ni alloy.

9.1 Microstructure study

Microstructure of homogenized and ECAP processed samples were studied using optical microscope, XRD, EBSD and SEM

9.1.1 Optical microscope image analysis

Figure 9.1 shows microstructure of homogenized and ECAP processed samples along the cross section of the sample. Microstructure is observed on the sample in a direction perpendicular to the ECAP axis and at the central portion of the sample, as there is a change in grain size at the leading edge and tail portion of the sample (Wei et al. 2006). Also, along the cross section of the sample, there are variations in grain sizes. Hence, average grain size can be determined by linear intercept method, using at least 20 vertical and horizontal lines at various regions on the cross section of each ECAP pass sample. Homogenized sample showed several annealing twin formations (indicated by black arrows in Figure 9.1(a)) and equiaxed grains of average size $75\mu\text{m}$ distributed throughout the sample. Figure 60(b) shows the microstructure of 1 pass ECAP processed sample, which shows shear band formation, and the average grain size reduced to $35\mu\text{m}$. With further deformations, grains elongate and showed clustered fine-grained regions (shown by the circle) distributed throughout the sample. With further increase in passes, shear bands became narrower. A prominent rate of refining of grains is noticed in even number of passes (Cabibbo 2010). Grain refinement was significant up to 5th ECAP pass. On further deformation, grain size remained consistent at $20\mu\text{m}$ and a saturated state was reached.

Grain refinement was controlled by varying the processing parameters like pressing route, temperature and strain. Pressing route produced a total strain of 5 after 8 pass. Final grain size obtained is dependent on initial grain size after homogenizing (Zhu et

al. 2013). Hence, high initial grain size of the alloy used has prominent effect on the refined grain size after the ECAP process.

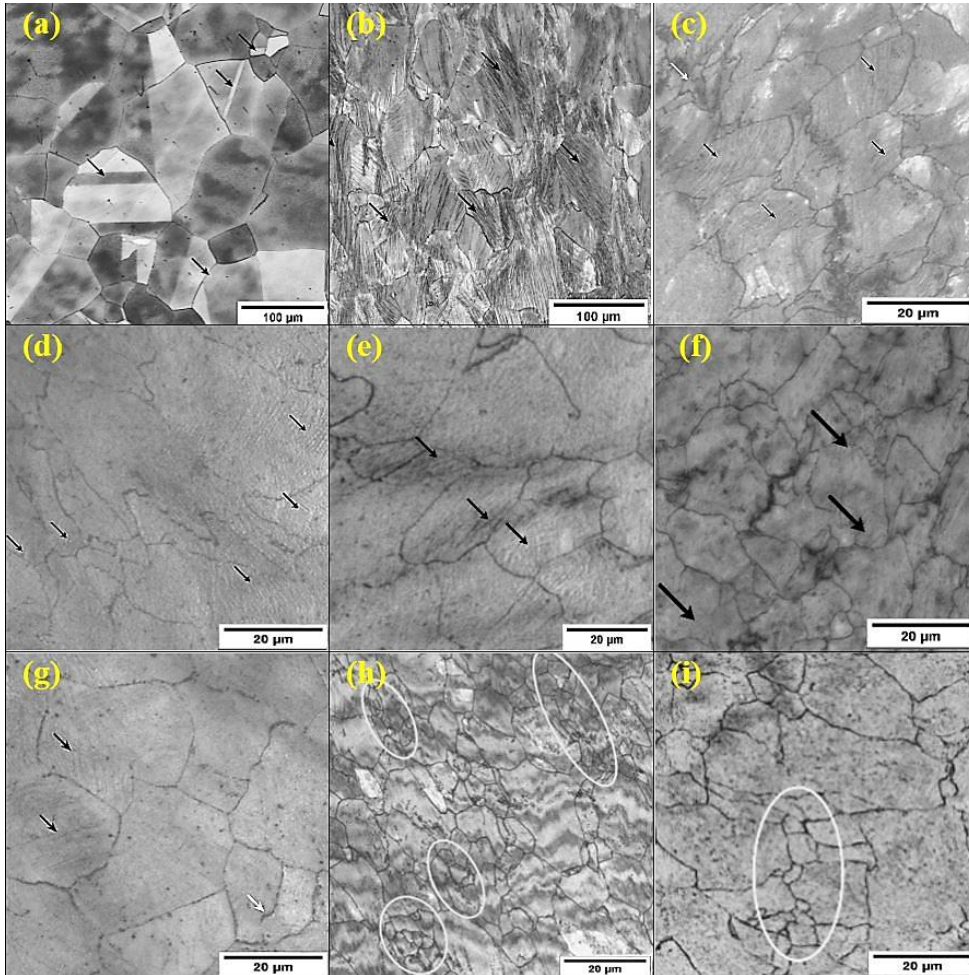


Figure 9.1 Optical microstructure of C70600 copper alloy samples in (a) homogenised condition and ECAP (b) 1P, (c) 2P, (d) 3P, (e) 4P, (f) 5P, (g) 6P, (h) 7P, (i) 8P conditions.

Grain refinement in the initial stages of deformation may be because of two prominent methods: (a) dislocation subdivision (DS) and (b) twin fragmentation (TF) (Qu et al. 2009). Here, both mechanisms are present in initial deformation cycles. Grain refinement by dislocation sub division was caused by dislocation cells formed from initial grains (Segal 2002). These dislocation cells formed were characterized by shear band formation and low angle misorientations of sub-boundaries. These misorientation

accumulations over further deformation caused an increase in strain and generation of higher angle grain boundaries (Naseri et al. 2018).

Another possible way where grain refinement takes place is by the mechanism of deformation twins formation in low stacking fault energy materials (Zi 2010). Cu, being a low stacking fault energy metal, showed deformation twins in initial deformation passes. But as deformation increased, twin formation was reduced and predominant mechanism of grain refinement was found to be dislocation subdivision. Twin formation is restricted over dislocation accumulation at higher deformation passes, because of crystal orientation and dislocation structure (An et al. 2019). As the dislocation accumulation and dynamic recrystallization balances each other, grain refinement reaches a saturated state (Figure 9.2). Due to concurrent dynamic recovery and relaxation, further deformation had no significant influence on grain size (Baik et al. 2003).

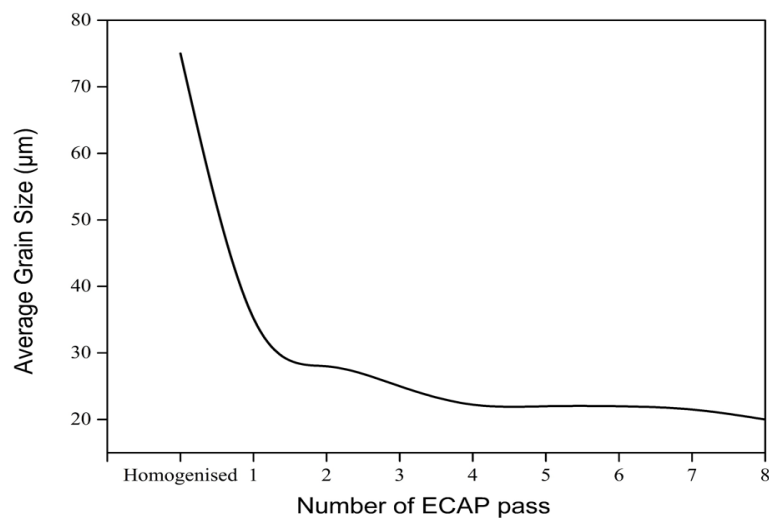


Figure 9.2 Change in average grain size with respect to number of ECAP passes

9.1.2 XRD analysis

Figure 9.3 shows the XRD image of homogenized and ECAP processed samples. The peaks in XRD data are of typical CuNi crystal with peaks at 2θ angles of ~ 46 , ~ 50 , ~ 75 , ~ 90 , ~ 95 . These peaks represent the planes of CuNi crystal structure for (111), (200), (220), (311), (222) planes, respectively. All peaks seen in XRD graph are of CuNi,

indicating an absence of formation of other phases during ECAP process. It is observed that there is decrease in intensity of peaks (111), (222) and (200) after first ECAP pass, indicating refinement of grains along these planes, during ECAP. There is no significant variation in (220) and (311) peaks.

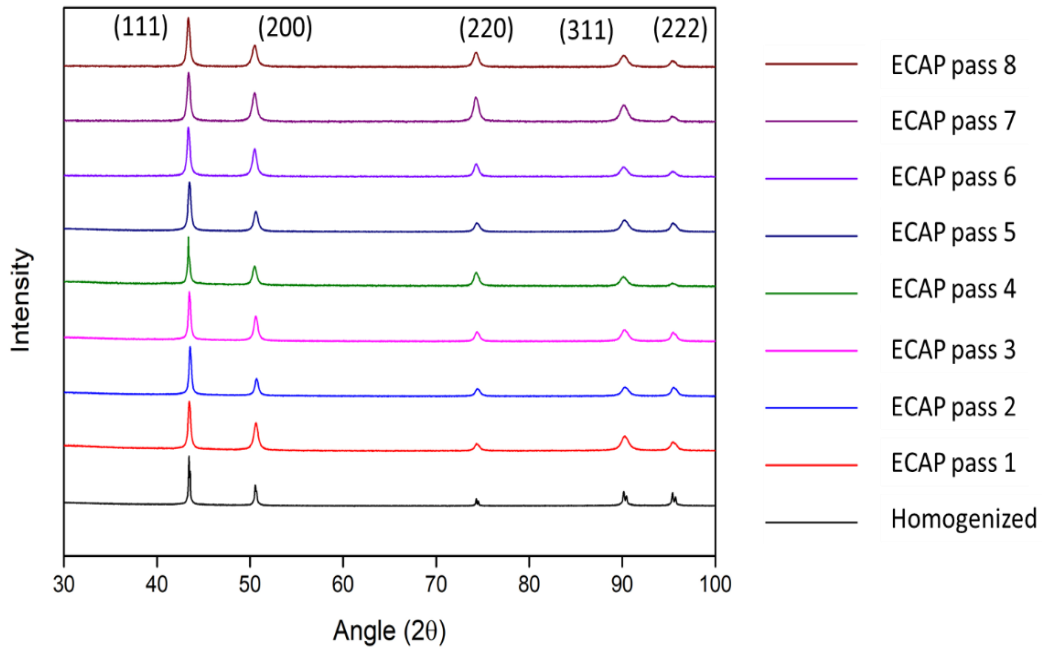


Figure 9.3 XRD graph of homogenized and ECAP processed samples

X-ray Diffraction data can provide information about micro-strain(ϵ) induced in the material during each pass, using Williamson–Hall’s equation (Williamson and Hall 1953)

$$\beta \cos (\theta) = \frac{k\lambda}{d} + 4\epsilon \sin (\theta) \quad (7)$$

Where k is the shape factor taken as 0.9 (Jiang et al. 2020), λ – radiation wavelength, d – effective crystallite size, θ – Bragg angle and ϵ – root mean square value of micro-strain. Micro-strain (ϵ) is obtained from slope of linear plot of $\beta \cos (\theta)$ against

$4\varepsilon \sin(\theta)$. From the slope, it was found that micro-strain of ECAP processed sample increased from 0.0016 to 0.0028 after 4th ECAP passes.

Further dislocation density(ρ) can be determined from micro-strain value using

$$\rho = \frac{2\sqrt{3}\varepsilon}{db} \quad (8)$$

Where, b – full width at half maximum (FWHM) of diffraction peaks, and d – grain size. Dislocation density increases from 0.00028 nm⁻² to 0.0015 nm⁻² after 4th ECAP pass.

It is noted that, grain size, determined from XRD data, was lower than the values obtained from optical microscope image analysis by ~0.1%. This is because, XRD data is based on intensity of X-rays received by sensor. Intensity of X-rays are affected by coherence of reflected X-rays from grain boundary and X-rays reflected off the dislocations cell walls. Grain size calculation by linear intercepts method is more accurate, as, it is based on average length of separation between grain boundaries only (Alawadhi et al. 2020a; Khereddine et al. 2013)

9.1.3 SEM Image analysis

Figure 9.4 represents Scanning Electron Microscope (SEM) images of homogenized and ECAP processed samples. Homogenized samples showed equiaxial grains with multiple twin formations spread throughout the sample. SEM image of ECAP processed sample showed the presence of shear band throughout the sample. Shear bands were visible in samples processed up to fourth pass. Figure 9.4(f) represents energy dispersive spectroscopy (EDS) of processed sample. Readings of EDS showed the presence of elements Cu, Ni, Fe, Si and Mn. EDS readings were consistent with homogenized and ECAP processed samples.

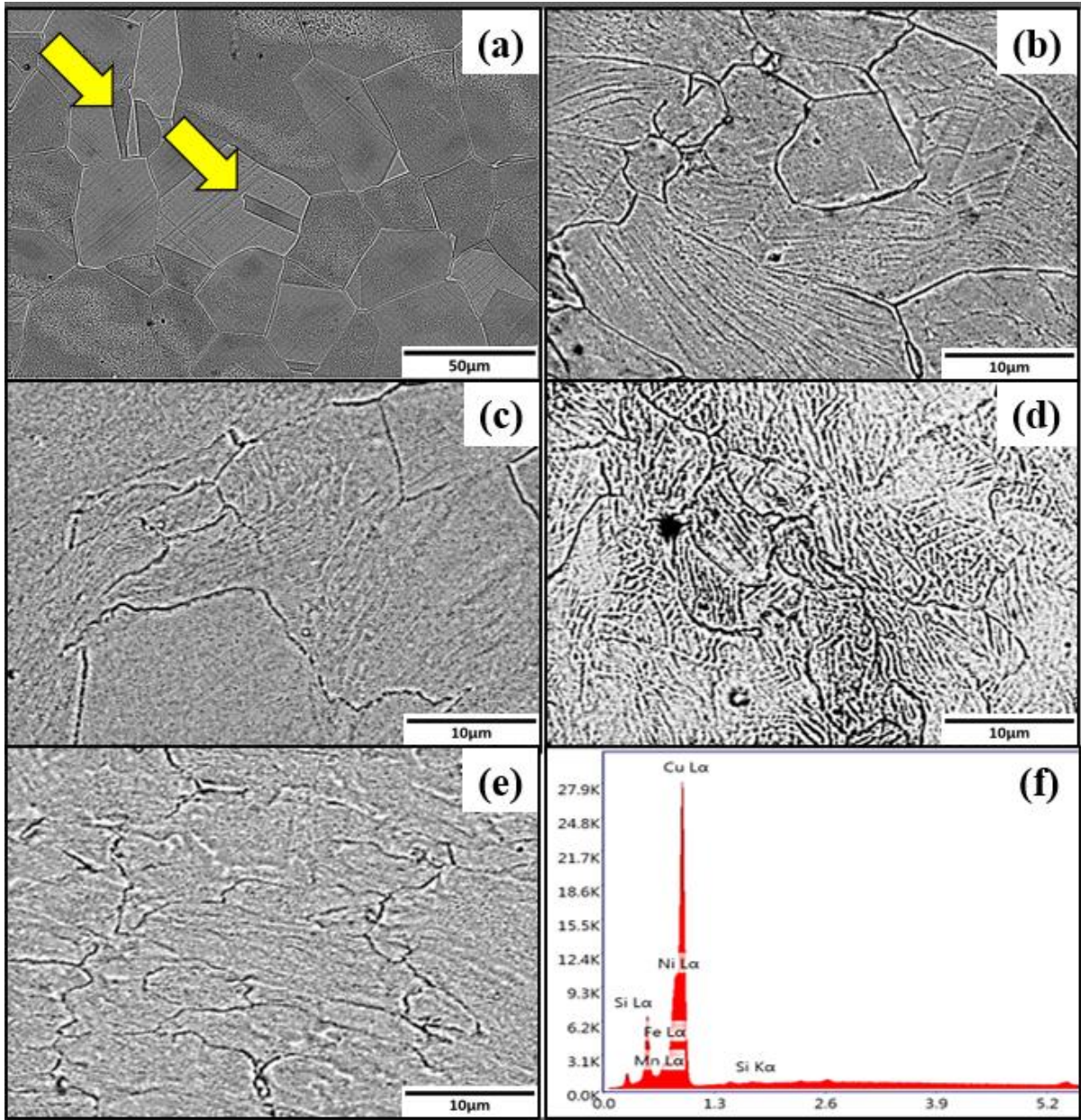


Figure 9.4 SEM image of (a) homogenized and ECAP processed samples (b) 1 pass, (c) 2 pass, (d) 3 pass, (e) 4 pass, (f) EDS data of processed sample

9.1.4 EBSD analysis

Figure 9.5 represents Orientation Imaging Microscope (OIM) based inverse pole figure of C70600 alloy. Homogenized sample consisted of equiaxial grains with an average grain size of 75 μm . Large number of twins were also observed from OIM image. After 4 ECAP passes, ultra-fine grains were found to be distributed along the boundaries of grains. OIM image of 8th ECAP pass sample showed equiaxial grains of average grain size 6 μm .

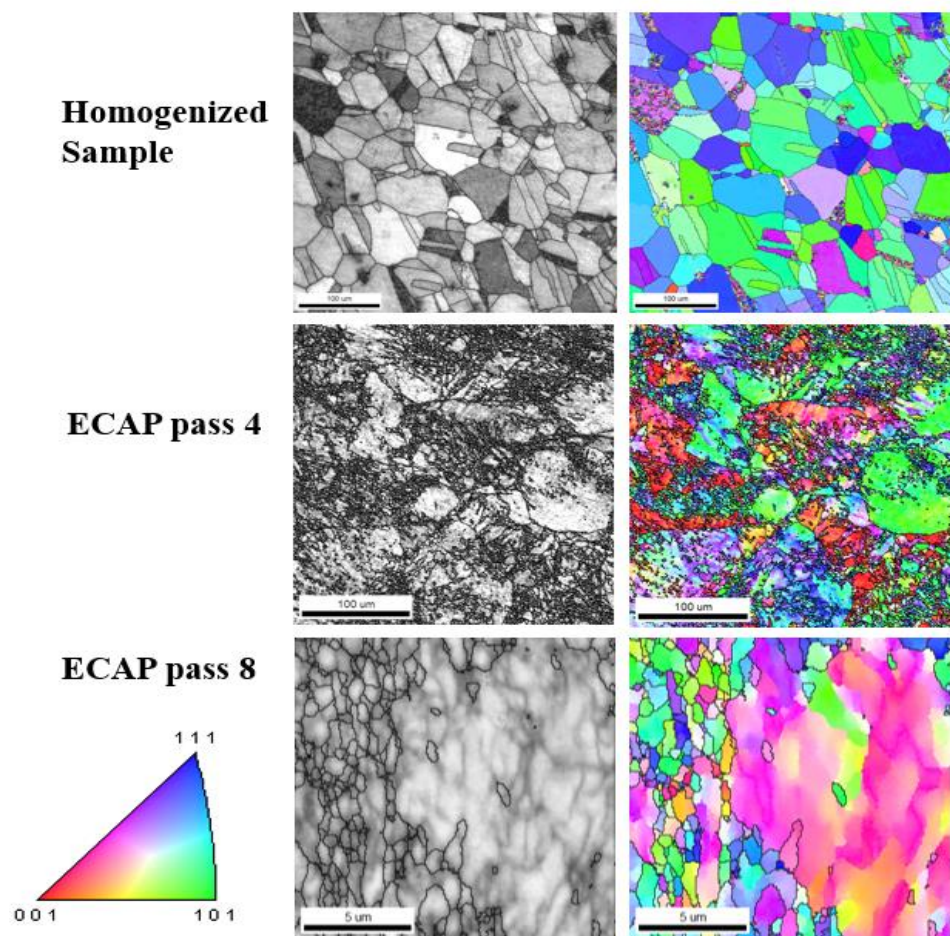


Figure 9.5 Orientation-imaging microscopy of C70600 alloy for homogenized and ECAP processed samples

Figure 9.6 represents misorientation distribution of C70600 alloy. There is an increase in low angle grain boundary (LAGB) with an increase in the number of ECAP passes. Misorientation angle less than 15 $^{\circ}$ is termed as LAGB. With increase in number of

ECAP passes, strain accumulation increase which results in conversion of high angle grain boundaries (HAGB) into LAGB (Mishra et al. 2005). The dominant orientation at the end of 8 pass ECAP process is in between the 001 plane and the 111 planes.

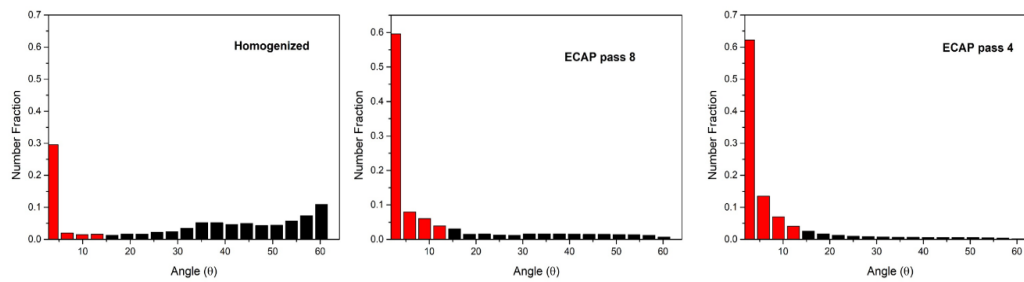


Figure 9.6 Misorientation angle distribution of C70600 alloy for homogenized and ECAP processed samples

9.2 Mechanical characterization

Homogenized and ECAP processed samples were subjected to tensile test and hardness test to characterize the mechanical properties and the results are shown below.

9.2.1 Micro hardness test

Hardness of homogenized sample was found to be 96 HV. Figure 9.7 shows the variation of microhardness with ECAP passes. Microhardness increases with increase in number of ECAP passes. Increase in hardness could be interpreted in two stages. In the first stage, steep increase in microhardness is observed with increase in number of ECAP passes i.e., upto 5th ECAP pass. In the second stage, i.e., from 5th to 8th ECAP pass, microhardness value remains stable with highest microhardness value of 174HV after 8 ECAP passes. Similar trend was reported by Khereddine et al. (Khereddine et al. 2013) during processing of Cu-Ni-Si specimen up to 8 ECAP passes. C70600 alloy sample, processed by ECAP upto 8th pass, produced hardness, 15% more than that produced by Friction stir processed (FSP) CuNi/ZrCp composite material (Suganya Priyadarshini et al. 2017). Drastic increase in microhardness, during the first stage is attributed to work hardening due to combined effect of grain boundary and dislocation strengthening mechanism (Alawadhi et al. 2020b). High strain induced during each

ECAP pass creates finer grains and more dislocations, which in turn caused restriction to dislocation movement. After 4th ECAP pass, specimen has completed one complete rotation in Bc route of ECAP and grain refinement has reached saturated state. With increase in ECAP passes further, there was no refining of grain and hardness value remained constant (Emeis et al. 2020).

It is also important to note the decrease in length of error bars as the number of passes increase. This indicates that the homogeneity in the hardness across a sample is achieved with higher number of passes (Wongsa-Ngam et al. 2012). This variation of hardness in the first stage may be attributed to dead zone formed at outer corner of the die, where specimen moves freely without any constraints of contact with the die wall. (Shan et al. 1999; Wei et al. 2006; Wu and Baker 1997) have reported this phenomenon experimentally and in simulations (Son et al. 2007; Yoon et al. 2007; Yoon and Kim 2008).

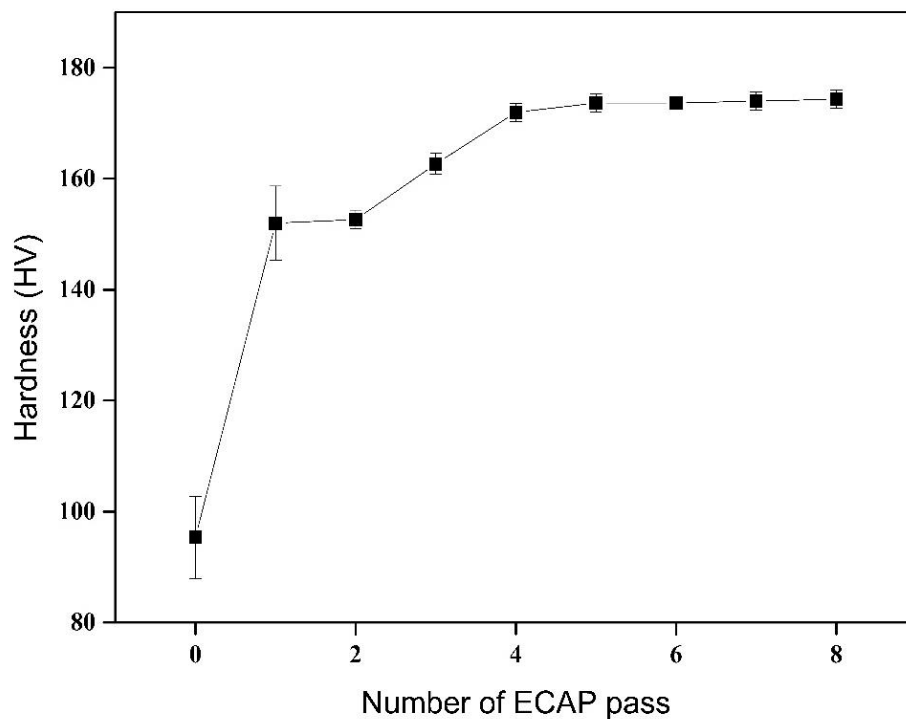


Figure 9.7 Hardness of homogenised and ECAP processed samples

9.2.2 Tensile test

Figure 54 shows the variation of UTS and % elongation with number of ECAP passes. It is noted that ultimate tensile strength (UTS) of the material increased with increase in the number of ECAP passes, but ductility is reduced. A continuous yield to failure is seen which is a typical pattern in coarse-grained Cu (Tian et al. 2018). A similar variation is reported in literature (Alawadhi et al. 2021; Gopi and Shivananda Nayaka 2017a; Wei et al. 2011). Increase in ultimate tensile strength is seen up to 5th ECAP pass. Further deformations reduce the ultimate tensile strength and elongation before failure (Figure 9.8). There is an increase of UTS by 54% and a reduction in elongation at the fracture by 8% after the 5th ECAP pass.

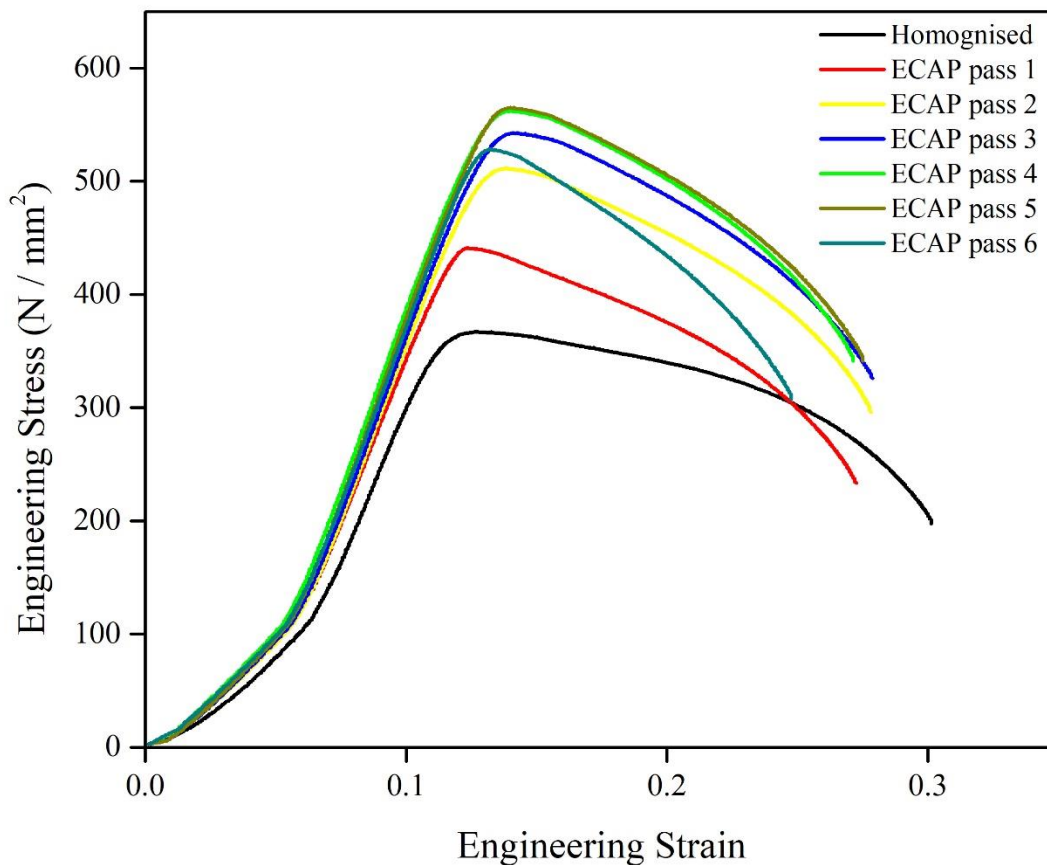


Figure 9.8 Stress vs strain graph of homogenized and ECAP processed samples

Figure 9.9 shows the variation of ultimate tensile strength (UTS) and total elongation to failure measurements with respect to grain size of homogenized and ECAP processed

C70600 samples. All the samples failed by typical ductile failure pattern of cup and cone. Homogenized C70600 sample exhibited a mean UTS of 360MPa and approximately 30% elongation before failure. Yield strength (YS) of homogenized sample was found to be 350MPa. After first ECAP pass, grain size reduced by over 50%, UTS and YS of C70600 increased by 20% and elongation to failure reduced drastically by 9%. The value of percentage elongation before necking also reduced from 6.3% to approximately 5.3%. Further, ECAP process progressively increased the UTS up to 565MPa and YS to 535MPa respectively, for the 5th ECAP pass sample, whereas elongation to failure remained nearly constant around 27.59%. After 6th ECAP pass, reduction in UTS and drastic reduction in elongation to failure is noted. Compared to research on improving mechanical property of C70600 alloy, UTS of 5th ECAP pass specimen was found to be 81%, better than friction stir processed 12 wt% ZrC particle embedded C70600 composite (Suganya Priyadarshini et al. 2017).

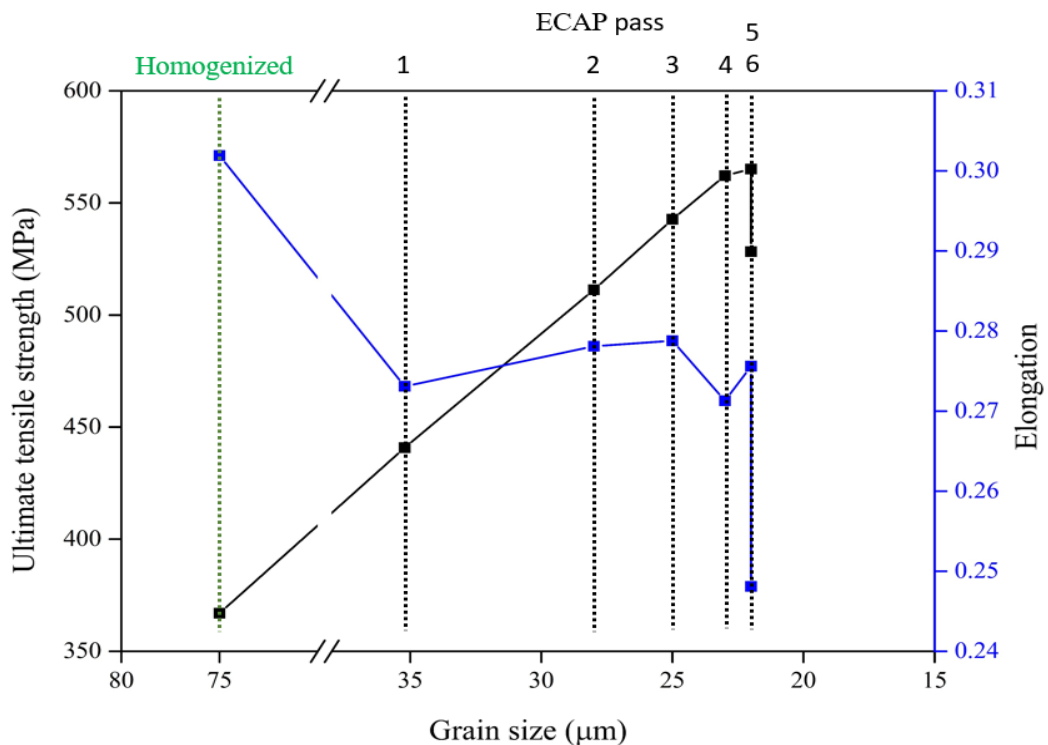


Figure 9.9 Ultimate Tensile Strength and elongation for Homogenized and ECAP processed

Three possible ways of strengthening observed in this study are solid solution strengthening, strengthening by grain refinement and strengthening by dislocation

(Suresh et al. 2019). Ni being the major alloying element and atomic size of Ni being similar to that of Cu and both being completely immiscible in each other, solid solution strengthening plays a minor role in strengthening of alloy. Upto 4th ECAP pass, large reduction in grain size and formation of sub-grain boundaries were noticed after each pass. Relation between grain size reduction and strength improvement is explained by classic Hall–Petch relationship (Hall 1951). After 6th pass, reduction in ultimate tensile strength is witnessed, a similar trend is seen in Cu processed by high pressure torsion (Edalati et al. 2008; Edalati and Horita 2011; Jiang et al. 2000) and ECAP (Chinh et al. 2004; Ebrahimi and Gode 2017; Wang et al. 2008). During tensile test, dislocations within the grains were activated and resulted in yielding pattern without typical yield drop (Tian et al. 2018). Hence, grain refinement strengthening and dislocation strengthening contribute to overall strengthening of C70600 alloy. Also, saturation of dislocation density resulted in saturation of strength of the material (Zhu et al. 2013).

ECAP may cause an increase in dislocation density and high angle grain boundaries and decrease in distance between grain boundaries (El Aal 2020). These boundaries act as restrictions and prevent the movement of dislocations and twins, which are the most significant deformation mechanism in coarse grained materials (Reihanian et al. 2008; Salimyanfard et al. 2011; Valiev et al. 2002). Hence, load required to overcome these restrictions increase the strength of the material. At higher number of passes, there is a reduction in rate of grain refinement and rate of increase of dislocation density. Also in SPD processes, grain boundaries that are formed from geometrically unnecessary dislocations makes grain boundaries highly unstable (Valiev et al. 2002). These grain boundaries enable grain boundary sliding or rotation (Salimyanfard et al. 2011). At higher number of passes, contribution of dislocation-strengthening and grain-refinement strengthening in strengthen of the material reduces which is seen by the reduction of UTS at after 6th pass.

9.2.2.1 Fractography

Figure 9.10 shows the SEM images of fracture surface of tensile test specimen. SEM image shows multiple dimple formation in the fractured surface. This indicates tensile type of cup and cone fracture. Dimples are characterized by tear ridges formation with cave in the center. These caves act as possible points of initiation of crack (Salimyanfard et al. 2013; Wang et al. 2020). Homogenized sample (Figure 9.10 (a)) showed deeper and wider caves. Also, numerous pores were detected in homogenized sample fractured surface (arrows in Figure 9.10 (a)). Dimples formed in the homogeneous samples were elongated compared to equiaxial dimples in ECAP processed samples.

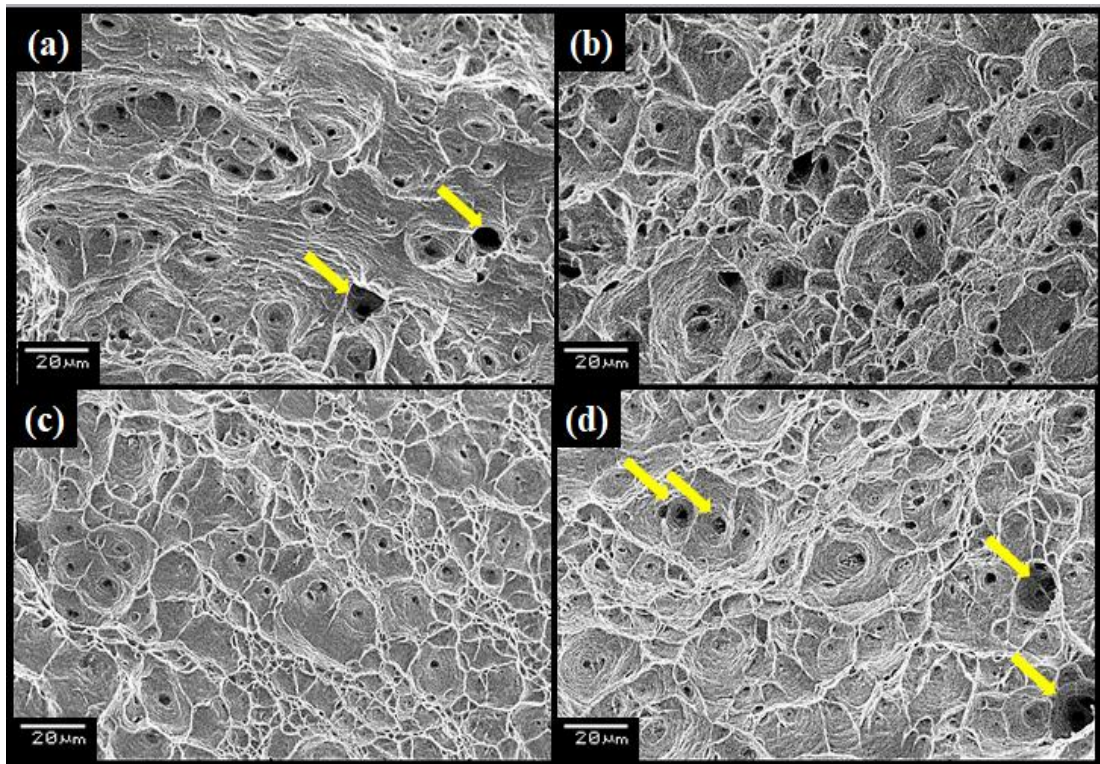


Figure 9.10 SEM image of tensile test fractured surface for (a) homogenized, ECAP pass

In the ECAP processed samples, formation of small and shallow dimples is the indication of very little plastic deformation before failure. Although grain refinement enables the material to withstand larger loads and the material became less ductile. Multiple pass in route B_c produces more equiaxial grains compared to other routes.

Equiaxial dimples at higher ECAP passes are because of fine equiaxial grains formed. More crack initiation points in 6th pass ECAP processed sample caused the reduction in ultimate tensile strength from 5th pass to 6th pass. Number and location of these crack initiation points depend on the strain induced in the process, sub-grain and dislocation accumulation at grain boundaries (El Aal 2020; Salimyanfard et al. 2013).

9.2.3 Corrosion test

Corrosion behaviour of homogenised and ECAP processed samples with 1 pass, 3 pass and 5 pass immersed in 1M NaCl solution at room temperature were studied using potentiodynamic polarization and Electrochemical impedance spectroscopy (EIS) methods

9.2.3.1 Potentiodynamic polarization study

Table 2 Electrochemical kinetic parameters like corrosion potential, corrosion current and corrosion rate

	E_{corr} (mV)			i_{corr} (μA)			Corrosion rate (mm/y)		
	0.1M	0.5M	1M	0.1M	0.5M	1M	0.1M	0.5M	1M
Homogenized	-141.69	-211.84	-285.47	9.03	16.39	15.88	0.21	0.37	0.36
ECAP pass 1	-169.55	-148.65	-271.76	12.39	22.70	17.90	0.28	0.52	0.41
ECAP pass 3	-125.28	-235.73	-272.43	13.02	12.61	13.71	0.30	0.29	0.31
ECAP pass 5	-145.69	-189.63	-260.06	8.70	13.62	15.23	0.20	0.31	0.35

Potentiodynamic polarization tests were performed to investigate corrosion behaviour of homogenized and ECAP processed samples. The test gives various electrochemical information like corrosion potential (E_{corr}), corrosion current density (i_{corr}) and corrosion rate (mm/y). Tafel extrapolation method gives E_{corr} and i_{corr} values from anodic part of polarization curves. Figure 9.11 gives the Tafel plot of homogenized and ECAP processed samples in 0.1M, 0.5M and 1M NaCl solutions. It is observed from

Figure 9.11 that the i_{corr} values after ECAP pass decreased. It is also noted that, with increase in concentration of NaCl solution, E_{corr} value of higher ECAP pass samples shifted in noble direction. Lower i_{corr} values indicate high corrosion resistance. Corrosion rate was obtained from Tafel plot and is tabulated in Table 2. It is noted that corrosion rate of the material reduced with increase in ECAP pass. Main reason for enhancement in corrosion resistance of grain-refined materials is attributed to improvement in passive film formation and adhesion due to increased grain boundary density (Ralston and Birbilis 2010).

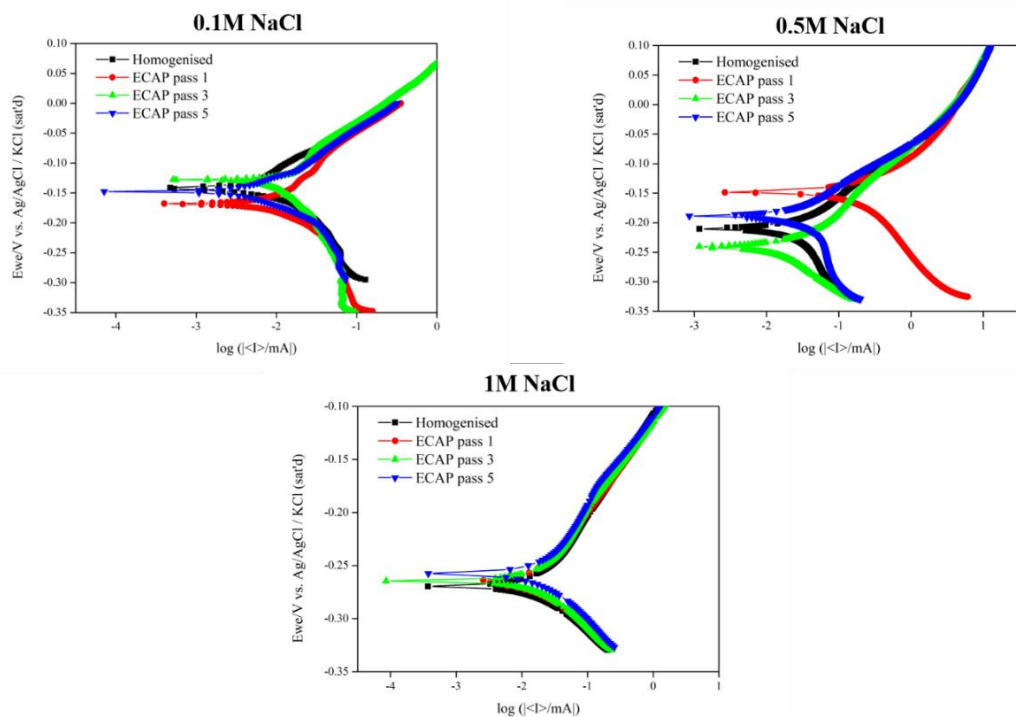


Figure 9.11 Tafel plot of Homogenized and ECAP processed samples in 0.1M, 0.5M and 1M NaCl solution

Figure 9.12 shows the variation in Tafel plot for homogenized and ECAP processed sample with increase in concentration of NaCl solution. It is seen that with increase in NaCl concentration, corrosion resistance of the material decreases and Tafel plot shifts in less noble direction. In general, Tafel plots shifted towards the direction of increasing current density and lower potential values with increase in chloride ion concentration

due to its destructive nature. Similar trend was reported by H. Ezuber and A. Al Shater (Ezuber and Shater 2016)

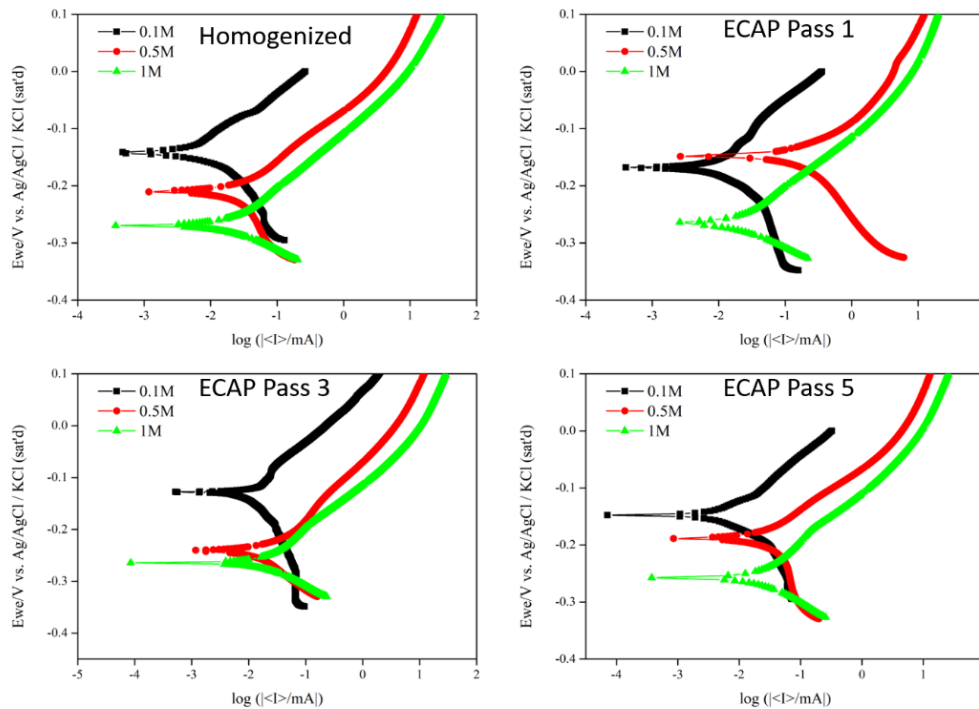


Figure 9.12 Tafel plot of homogenized and ECAP processed sample with increase in

9.2.3.2 Electrochemical impedance spectroscopy (EIS)

Electrochemical impedance spectroscopy (EIS) is used to understand the mechanism of corrosion process taking place at the interface between the electrode and the electrolyte. The process provides the impedance and capacitance loops that depict the mechanism of corrosion taking place at the interface. Figure 9.13 shows Nyquist plots for homogenised and ECAP processed samples placed in NaCl solution. Nyquist plot shows two semicircles. The larger circle depicts the formation of protective film on the surface of the electrode and it is the capacitance arc. The smaller semicircle is the impedance arc and it represents the degradation of the protective film formed on the surface. Radius of the capacitance arc provides information about the corrosion resistance of the material. Larger arc relates to better corrosion resistance.

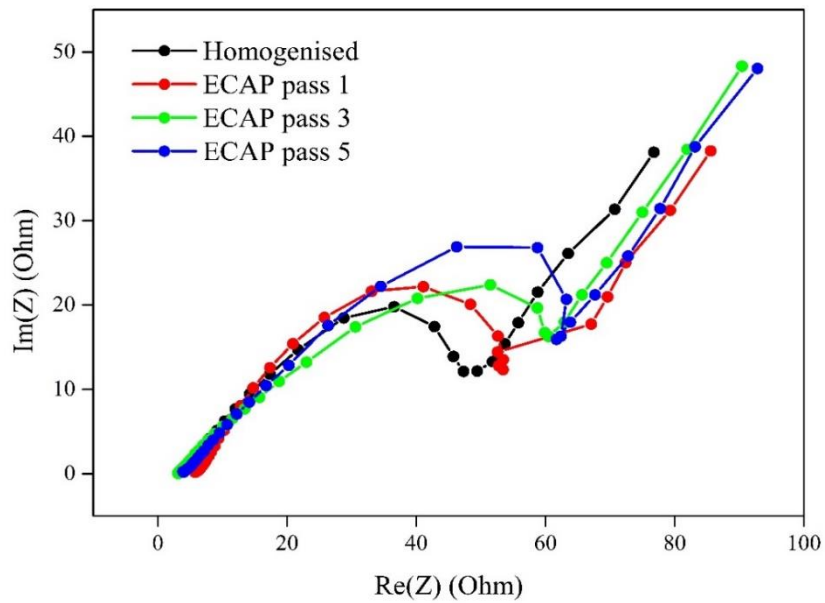


Figure 9.13 Nyquist plots for homogenised and ECAP processed Cu-Ni samples

From the Nyquist plot, it can be derived that corrosion resistance of the alloy has increased with increase in the number of ECAP passes. Capacitance arc of ECAP processed sample after 5 passes has the highest radius.

CHAPTER 10 CONCLUSION

Copper-Nickel alloy C70600 is extensively used in enormous quantities for structural application in the marine environment. An improvement in the mechanical properties of the material without affecting the corrosion resistance property of the material could promote better usage. Studies by researchers have proven Severe Plastic Deformation (SPD) to improve the mechanical properties of many materials. Among SPD processes, Equal Channel Angular Pressing (ECAP) is advantageous in continuously processing bulk material without change in the material's cross section and requires minimum specimen preparation.

In the present work, copper alloy C70600 was successfully processed at room temperature up to 8 ECAP passes. Microstructural study of ECAP processed sample showed a reduction in grain size from 75 μ m for the homogenized sample to 20 μ m for the 8th ECAP pass sample. Grain refinement was intense up to the 5th ECAP pass. During further processing of the alloy there was no significant change in the grain size.

XRD data analysis of processed samples showed peaks of Cu-Ni only. There was no presence of any precipitate peaks. An increase in micro-strain and dislocation density with an increase in deformation was noticed from XRD data.

SEM images of the homogenized samples showed presence of annealing twins. ECAP processed samples showed presence shear bands up to 6th ECAP pass. EDS data showed major constituents to be Cu and Ni.

ECAP processed C70600 alloy also resulted in mechanical property enhancement. Micro hardness of the homogenized sample was found to be 96HV. Micro hardness increased by 45% during the first 5 ECAP passes. Further increase in deformation had no impact on micro hardness value and remained constant at 174HV.

The yield strength and ultimate tensile strength (UTS) of the homogenized sample was found to be 350MPa and 360MPa respectively. An increase in YS by 52%, UTS by 54% and a reduction in elongation by 8% was witnessed after the 5th ECAP pass.

Further, deformation softened the material, resulting in a reduction of ultimate tensile strength and ductility.

Fractured surface of tensile tested 5th ECAP processed sample showed the least number of dimples. ECAP processing resulted in the formation of equiaxial, shallow and small dimples in the alloy.

The corrosion resistance of the 5th pass ECAP processed material was found to be more than the homogenized material.

SCOPE FOR FUTURE WORK

- Dry sliding wear test to be conducted using pin-on-disc type test rig (ASTM G-99) at room temperature to study the wear resistance of as received and ECAP processed Cu-Ni alloys.
- To examine the corrosion behavior of as-received and ECAP processed samples in Sulphur rich and Oxygen rich NaCl solutions
- Examine the fatigue behavior after ECAP processing

REFERENCES

- Aal, M. I. A. El. (2020). "The influence of ECAP and HPT processing on the microstructure evolution, mechanical properties and tribology characteristics of an Al6061 alloy." *J. Mater. Res. Technol.*, 9(6), 12525–12546.
- Al-Odwani, A., El-Sayed, E. E. F., Al-Tabtabaei, M., and Safar, M. (2006). "Corrosion resistance and performance of copper-nickel and titanium alloys in MSF distillation plants." *Desalination*, 201(1–3), 46–57.
- Alawadhi, M. Y., Sabbaghianrad, S., Huang, Y., and Langdon, T. G. (2020a). "Evaluating the paradox of strength and ductility in ultrafine-grained oxygen-free copper processed by ECAP at room temperature." *Mater. Sci. Eng. A*, 802(September 2020), 140546.
- Alawadhi, M. Y., Sabbaghianrad, S., Huang, Y., and Langdon, T. G. (2021). "Evaluating the paradox of strength and ductility in ultrafine-grained oxygen-free copper processed by ECAP at room temperature." *Mater. Sci. Eng. A*, 802(September), 140546.
- Alawadhi, M. Y., Sabbaghianrad, S., Wang, Y. C., Huang, Y., and Langdon, T. G. (2020b). "Characteristics of grain refinement in oxygen-free copper processed by equal-channel angular pressing and dynamic testing." *Mater. Sci. Eng. A*, 775, 138985.
- An, X. H., Wu, S. D., Wang, Z. G., and Zhang, Z. F. (2019). "Significance of stacking fault energy in bulk nanostructured materials: Insights from Cu and its binary alloys as model systems." *Prog. Mater. Sci.*, 101(November 2018), 1–45.
- Ardy, H., Sasmita, F., Adhe, E., and Pradana, P. (2021). "The corrosion study of 90Cu-10Ni (UNS C70600) materials in ammonia and sulfide environments." *AIP Conf. Proc.*, 040007(2338).
- ASTM. (2014). "D5528-01: Standard Test Method for Mode I Interlaminar Fracture Toughness of Unidirectional Fiber-Reinforced Polymer Matrix Composites 1." *Am. Stand. Test. Methods*, 03(Reapproved 2007), 1–12.

Baik, S. C., Estrin, Y., Kim, H. S., and Hellmig, R. J. (2003). "Dislocation density-based modeling of deformation behavior of aluminium under equal channel angular pressing." *Mater. Sci. Eng. A*, 351(1–2), 86–97.

Biglari, H., Salahi, S., Gharajeh, S. N., and Azar, M. G. (2014). "Investigation of Annealing Heat Treatment Effect on the Microstructure and Mechanical Properties of Friction Stir Welded C70600 Copper Nickel Alloy Joints." *J. Mechatronics*, 2(2), 119–123.

Cabibbo, M. (2010). "A TEM Kikuchi pattern study of ECAP AA1200 via routes A, C, BC." *Mater. Charact.*, 61(6), 613–625.

Chinh, N. Q., Horita, Z., and Langdon, T. G. (2004). "A new constitutive relationship for the homogeneous deformation of metals over a wide range of strain." *Acta Mater.*, 52, 3555–3563.

Chung, S. W., Yun, T. J., Noh, J. S., and Kang, C. Y. (2018). "Microstructure and Mechanical Properties in the Friction Stir Welded C70600 Alloy." *J. Weld. Join.*, 36(2), 60–66.

Ebrahimi, M., and Gode, C. (2017). "Severely deformed copper by equal channel angular pressing." *Prog. Nat. Sci. Mater. Int.*, 27(2), 244–250.

Edalati, K., Fujioka, T., and Horita, Z. (2008). "Microstructure and mechanical properties of pure Cu processed by high-pressure torsion." *Mater. Sci. Eng. A*, 497, 168–173.

Edalati, K., and Horita, Z. (2011). "Significance of homologous temperature in softening behavior and grain size of pure metals processed by high-pressure torsion." *Mater. Sci. Eng. A*, 528(25–26), 7514–7523.

Eiselstein, L. E., Syrett, B. C., Wing, S. S., and Caligiuri, R. D. (1983). "The accelerated corrosion of CuNi alloys in sulphide-polluted seawater: Mechanism no. 2." *Corros. Sci.*, 23(3), 223–239.

Emeis, F., Peterlechner, M., and Wilde, G. (2020). "Hall–Petch Relations of Severely Deformed Cu, Ni, and Cu–Ni Alloys: Analysis of the Dislocation Blockage Strength of Deformation-Modified Grain Boundaries." *Adv. Eng. Mater.*, 22(1), 1900429.

Ezuber, H. (2014). "Corrosion failure 90 / 10 cupronickel tubes in a desalination plant Corrosion Cupronickel Tubes in a Desalination Plant Corrosion failure cupronickel tubes in a desalination plant." *Desalin. Water Treat.*, 21 (2010)(September 2010), 17–22.

Ezuber, H. M. (2015a). "Effect of temperature and thiosulphate on the corrosion behaviour of 90-10 copper-nickel alloys in seawater." *Anti-Corrosion Methods Mater.*, 56/3 2009(May 2009), 168–172.

Ezuber, H. M. (2015b). "The role of iron content on the corrosion behavior of 90Cu-10Ni alloys in 3 . 5 % NaCl solutions." *Anti-Corrosion Methods Mater.*, 59/4(June 2012), 195–202.

Ezuber, H., and Shater, A. Al. (2015). "Influence of environmental parameters on the corrosion behavior of 90 / 10 cupronickel tubes in 3 . 5 % NaCl." *Desalin. Water Treat.*, 57(March), 1–10.

Ezuber, H., and Shater, A. Al. (2016). "Corrosion Behavior of Copper-Nickel Alloys in Seawater Environment." *16th Middle east Corros. confrence Exhib.*, (February).

Faeghfar, H., Khanzadeh, M., Bakhtiari, H., Shajari, Y., and Seyedraoufi, Z. S. (2019). "Microstructural and mechanical investigation of dissimilar joint of AISI 304L and UNS C70600 via pulsed gas tungsten arc welding." *Eng. Res. Express*, 1(2).

Faraji, G., Kim, H. S., and Kashi, H. T. (2018). "Severe Plastic Deformation Methods for Sheets." *Sev. Plast. Deform.*, 113–129.

Gopi, K. R., and Shivananda Nayaka, H. (2017a). "Microstructure and mechanical properties of magnesium alloy processed by equal channel angular pressing (ECAP)." *Mater. Today Proc.*, 4(9), 10288–10292.

Gopi, K. R., and Shivananda Nayaka, H. (2017b). "Microstructure and mechanical

properties of magnesium alloy processed by equal channel angular pressing (ECAP).” *Mater. Today Proc.*, 4(9), 10288–10292.

Hall, E. O. (1951). “The Deformation and Ageing of Mild Steel: {III} Discussion of Results.” *Proc. Phys. Soc. Sect. B*, 64(9), 747–753.

Hallett, S. R. (2000). “Three-point beam impact tests on T300 / 914 carbon- ® bre composites.” *Compos. Sci. Technol.*, 60, 115–124.

Hallett, S. R., and Ruiz, C. (1997). “Material Characterization Tests and Modelling of Carbon Fibre T300/914 at Impact Rates of Strain.” *Le J. Phys. IV*, 07(C3), C3-465-C3-470.

Henaff-Gardin, C., and Lafarie-Frenot, M. C. (2002). “The use of a characteristic damage variable in the study of transverse cracking development under fatigue loading in cross-ply laminates.” *Int. J. Fatigue*, 24(2–4), 389–395.

Hou, J. P., and Ruiz, C. (2000). “Measurement of the properties of woven CFRP T300/914 at different strain rates.” *Compos. Sci. Technol.*, 60(15), 2829–2834.

Hug, G., Thévenet, P., Fitoussi, J., and Baptiste, D. (2006). “Effect of the loading rate on mode I interlaminar fracture toughness of laminated composites.” *Eng. Fract. Mech.*, 73(16), 2456–2462.

Jiang, H., Zhu, Y. T., Butt, D. P., Alexandrov, I. V., and Lowe, T. C. (2000). “Microstructural evolution , microhardness and thermal stability of HPT-processed Cu.” *Mater. Sci. Eng. A*, 290, 128–138.

Jiang, L., Fu, H., Wang, C., Li, W., and Xie, J. (2020). “Enhanced Mechanical and Electrical Properties of a Cu-Ni-Si Alloy by Thermo-mechanical Processing.” *Metall. Mater. Trans. A Phys. Metall. Mater. Sci.*, 51(1), 331–341.

Kapoor, R. (2017). “Chapter 20 - Severe Plastic Deformation of Materials.” *Mater. Under Extrem. Cond.*, Amsterdam: Elsevier, 717–754.

Khereddine, A. Y., Larbi, F. H., Kawasaki, M., Baudin, T., Bradai, D., and Langdon, T. G. (2013). “An examination of microstructural evolution in a Cu–Ni–Si alloy

processed by HPT and ECAP.” *Mater. Sci. Eng. A*, 576, 149–155.

Kim, H. S., Kim, W. Y., and Song, K. H. (2012). “Effect of post-heat-treatment in ECAP processed Cu-40%Zn brass.” *J. Alloys Compd.*, 536(SUPPL.1), S200–S203.

Lafarie-Frenot, M. C., and Touchard, F. (1994). “Comparative in-plane shear behaviour of long-carbon-fibre composites with thermoset or thermoplastic matrix.” *Compos. Sci. Technol.*, 52(3), 417–425.

Lee, T. S. (1983). “Use of Sodium Dichromate Pretreatment for Enhanced Marine Corrosion Resistance of C70600.” *Corrosion*, 39(9), 371–376.

Liu, H. Y., Yan, W., Yu, X. Y., and Mai, Y. W. (2007). “Experimental study on effect of loading rate on mode I delamination of z-pin reinforced laminates.” *Compos. Sci. Technol.*, 67(7–8), 1294–1301.

Ma, A. L., Jiang, S. L., Zheng, Y. G., and Ke, W. (2015). “Corrosion product film formed on the 90/10 copper-nickel tube in natural seawater: Composition/structure and formation mechanism.” *Corros. Sci.*, 91, 245–261.

Ma, A., Nishida, Y., Suzuki, K., Shigematsu, I., and Saito, N. (2005). “Characteristics of plastic deformation by rotary-die equal-channel angular pressing.” *Scr. Mater.*, 52(6), 433–437.

Mehr, V. Y., Rezaeian, A., and Toroghinejad, M. R. (2015). “Application of accumulative roll bonding and anodizing process to produce Al–Cu–Al₂O₃ composite.” *Mater. Des.*, 70, 53–59.

Mishra, A., Richard, V., Gr, F., Asaro, R. J., Meyers, M. A., and Propri, L. (2005). “Microstructural evolution in copper processed by severe plastic deformation.” *Mater. Sci. Eng. A*, 410–411, 290–298.

Mouritz, A. P., and Koh, T. M. (2014). “Re-evaluation of mode I bridging traction modelling for z-pinned laminates based on experimental analysis.” *Compos. Part B Eng.*, 56, 797–807.

Naseri, M., Gholami, D., Imantalab, O., Attarzadeh, F. R., and Fattah-Alhosseini, A.

(2018). “Effect of grain refinement on mechanical and electrochemical properties of severely deformed pure copper through equal channel angular pressing.” *Mater. Res. Express*, 5(7), 76504.

Ni, S., Jiang, J., Chen, J., Song, D., and Ma, A. (2016). “Microstructure and properties of in-situ synthesized Cu-1 wt%TiC alloy followed by ECAP and post-annealing.” *Prog. Nat. Sci. Mater. Int.*, 26(6), 643–649.

North, R. F., and Pryor, M. J. (1970). “The influence of corrosion product structure on the corrosion rate of Cu-Ni alloys.” *Corros. Sci.*, 10(5), 297–311.

Pierron, F., and Vautrin, A. (1994). “Accurate comparative determination of the in-plane shear modulus of T300/914 by the iosipescu and 45° off-axis tests.” *Compos. Sci. Technol.*, 52(1), 61–72.

Praveen, T. R., Gopi, K. R., and Nayaka, H. S. (2018). “Numerical Simulation of Shot Peening Process on Equal Channel Angular Pressed Magnesium Alloy.” *Silicon*, 10(6), 2463–2472.

Qu, S., An, X. H., Yang, H. J., Huang, C. X., Yang, G., Zang, Q. S., Wang, Z. G., Wu, S. D., and Zhang, Z. F. (2009). “Microstructural evolution and mechanical properties of Cu – Al alloys subjected to equal channel angular pressing.” *Acta Mater.*, 57(5), 1586–1601.

Ralston, K. D., and Birbilis, N. (2010). “Effect of Grain Size on Corrosion : A Review.” *Corrosion*, 66(7), 1–13.

Ramesh, S., Anne, G., Nayaka, H. S., Sahu, S., and Ramesh, M. R. (2019). “Investigation of dry sliding wear properties of multi-directional forged Mg–Zn alloys.” *J. Magnes. Alloy.*, 7(3), 444–455.

Ramkumar, J. D. W. (1985). “Characterization of Mode I and Mixed-Mode Delamination Growth in T300 / 5208 Graphite / Epoxy.” *ASTM Int.*, 315–335.

- Reihanian, M., Ebrahimi, R., Tsuji, N., and Moshksar, M. M. (2008). "Analysis of the mechanical properties and deformation behavior of nanostructured commercially pure Al processed by equal channel angular pressing (ECAP)." *Mater. Sci. Eng. A*, 473(1–2), 189–194.
- Salimyanfard, F., Reza Toroghinejad, M., Ashrafizadeh, F., and Jafari, M. (2011). "EBSD analysis of nano-structured copper processed by ECAP." *Mater. Sci. Eng. A*, 528(16–17), 5348–5355.
- Salimyanfard, F., Toroghinejad, M. R., Ashrafizadeh, F., Hoseini, M., and Szpunar, J. A. (2013). "Investigation of texture and mechanical properties of copper processed by new route of equal channel angular pressing." *Mater. Des.*, 44, 374–381.
- Schleich, W. (2004). "Typical failures of cuni 90/10 seawater tubing systems and how to avoid them." *EUROCORR 2004 - Eur. Corros. Conf. Long Term Predict. Model. Corros.*, 0049(0).
- Schön, J., Nyman, T., Blom, A., and Ansell, H. (2000). "A numerical and experimental investigation of delamination behaviour in the DCB specimen." *Compos. Sci. Technol.*, 60(2), 173–184.
- Segal, V. M. (2002). "Severe plastic deformation: Simple shear versus pure shear." *Mater. Sci. Eng. A*, 338(1–2), 331–344.
- Shan, A., Moon, I. G., Ko, H. S., and Park, J. W. (1999). "Direct observation of shear deformation during equal channel angular pressing of pure aluminum." *Scr. Mater.*, 41(4), 353–357.
- Shivakumar, K., Chen, H., Abali, F., Le, D., and Davis, C. (2006). "A total fatigue life model for mode I delaminated composite laminates." *Int. J. Fatigue*, 28(1), 33–42.
- Son, I. H., Jin, Y. G., Im, Y. T., Chon, S. H., and Park, J. K. (2007). "Sensitivity of friction condition in finite element investigations of equal channel angular extrusion." *Mater. Sci. Eng. A*, 445–446, 676–685.

Stewart, W. C., and LaQue, F. L. (1952). "Corrosion characteristics of iron modified 90:10 Cu-Ni alloy." *Corros.-NACE*.

Suganya Priyadarshini, G., Subramanian, R., Murugan, N., and Sathiskumar, R. (2017). "Surface modification and characterization of zirconium carbide particulate reinforced C70600 CuNi composite fabricated via friction stir processing." *J. Mech. Sci. Technol.*, 31(8), 3755–3760.

Suresh, M., Sharma, A., More, A. M., Kalsar, R., Bisht, A., Nayan, N., and Suwas, S. (2019). "Effect of equal channel angular pressing (ECAP) on the evolution of texture, microstructure and mechanical properties in the Al-Cu-Li alloy AA2195." *J. Alloys Compd.*, 785, 972–983.

Symons, D. D. (2000). "Characterisation of indentation damage in 0/90 lay-up T300/914 CFRP." *Compos. Sci. Technol.*, 60(3), 391–401.

Symons, D. D., and Davis, G. (2000). "Fatigue testing of impact-damaged T300/914 carbon-fibre-reinforced plastic." *Compos. Sci. Technol.*, 60(3), 379–389.

Taher, A., Jarjoura, G., and Kipouros, G. J. (2007). "Corrosion Behaviour of Commercial Cu-Ni-Fe alloy (C70600) in Sea Water." *ECS Meet.*, MA2007-01, 512.

Taher, A. M., Jarjoura, G., and Kipouros, G. J. (2011). "Effect of iron as alloying element on electrochemical behaviour of 90 : 10 Cu-Ni alloy." *Can. Metall. Q.*, 50(4), 425–438.

Tian, Y. Z., Gao, S., Zhao, L. J., Lu, S., Pippan, R., Zhang, Z. F., and Tsuji, N. (2018). "Scripta Materialia Remarkable transitions of yield behavior and Lüders deformation in pure Cu by changing grain sizes." *Scr. Mater.*, 142, 88–91.

Turon, A., Costa, J., Camanho, P. P., and Dávila, C. G. (2007). "Simulation of delamination in composites under high-cycle fatigue." *Compos. Part A Appl. Sci. Manuf.*, 38(11), 2270–2282.

Tuthill, A. H. (1987). "Guidelines for the use of copper alloys in seawater." *Mater. Perform.*, 26, 12–22.

- Valiev, R. Z., Alexandrov, I. V., Zhu, Y. T., and Lowe, T. C. (2002). "Paradox on of strength and ductility in metals processed by SPD." *J. Mater. Res.*, 17, 5–8.
- Valiev, R. Z., and Langdon, T. G. (2006). "Principles of equal-channel angular pressing as a processing tool for grain refinement." *Prog. Mater. Sci.*, 51(7), 881–981.
- Wang, J. T., Zhang, Y., and Liu, J. Q. (2008). "Continuous recrystallization phenomenon in high purity copper during equal channel angular pressing up to high strain at room temperature." *Mater. Sci. Forum*, 584–586, 929–937.
- Wang, W., Zhu, J., Qin, N., Zhang, Y., Li, S., Xiao, Z., Lei, Q., and Li, Z. (2020). "Effects of minor rare earths on the microstructure and properties of Cu-Cr-Zr alloy." *J. Alloys Compd.*, 847, 155762.
- Wei, K. X., Wei, W., Wang, F., Du, Q. B., Alexandrov, I. V., and Hu, J. (2011). "Microstructure, mechanical properties and electrical conductivity of industrial Cu-0.5%Cr alloy processed by severe plastic deformation." *Mater. Sci. Eng. A*, 528(3), 1478–1484.
- Wei, W., Nagasekhar, A. V., Chen, G., Tick-Hon, Y., and Wei, K. X. (2006). "Origin of inhomogenous behavior during equal channel angular pressing." *Scr. Mater.*, 54(11), 1865–1869.
- Williams, G., Trask, R., and Bond, I. (2007). "A self-healing carbon fibre reinforced polymer for aerospace applications." *Compos. Part A Appl. Sci. Manuf.*, 38(6), 1525–1532.
- Williamson, G. K., and Hall, W. H. (1953). "X-ray line broadening from filed aluminium and wolfram." *Acta Metall.*, 1(1), 22–31.
- Wongsa-Ngam, J., Kawasaki, M., and Langdon, T. G. (2012). "The development of hardness homogeneity in a Cu-Zr alloy processed by equal-channel angular pressing." *Mater. Sci. Eng. A*, 556, 526–532.
- Wu, Y., and Baker, I. (1997). "An experimental study of equal channel angular extrusion." *Scr. Mater.*, 37(4), 437–442.

Xu, C., Horita, A. Z., and Langdon, A. T. G. (2008). "Evaluating the influence of pressure and torsional strain on processing by high-pressure torsion." *J. Mater. Sci.*, 43, 7286–7292.

Yang, R., Wen, J., Zhou, Y., Song, K., and Song, Z. (2018). "Effect of Al element on the microstructure and properties of Cu-Ni-Fe-Mn alloys." *Materials (Basel)*, 11(9).

Yasaee, M., Lander, J. K., Allegri, G., and Hallett, S. R. (2014). "Experimental characterisation of mixed mode traction-displacement relationships for a single carbon composite Z-pin." *Compos. Sci. Technol.*, 94, 123–131.

Yoon, S. C., and Kim, H. S. (2008). "Finite element analysis of the effect of the inner corner angle in equal channel angular pressing." *Mater. Sci. Eng. A*, 490(1–2), 438–444.

Yoon, S. C., Quang, P., Hong, S. I., and Kim, H. S. (2007). "Die design for homogeneous plastic deformation during equal channel angular pressing." *J. Mater. Process. Technol.*, 187–188, 46–50.

Zhang, A., Li, D., Lu, H., and Zhang, D. (2011). "Qualitative separation of the effect of voids on the bending fatigue performance of hygrothermal conditioned carbon/epoxy composites." *Mater. Des.*, 32(10), 4803–4809.

Zhou, M., Ren, L., Quan, G., and Gupta, M. (2021). "Solid Phase Processing of Metal Matrix Composites." *Encycl. Mater. Compos.*, D. Brabazon, ed., Oxford: Elsevier, 173–196.

Zhu, C. F., Du, F. P., Jiao, Q. Y., Wang, X. M., Chen, A. Y., Liu, F., and Pan, D. (2013). "Microstructure and strength of pure Cu with large grains processed by equal channel angular pressing." *Mater. Des.*, 52, 23–29.

Zi, A. (2010). "Pure copper processed by extrusion preceded equal channel angular pressing." *Mater. Charact.*, 61(2), 141–144.

ZOU, D. li, HE, L. feng, XIAO, D. wu, ZHAO, Y. wen, QIU, Z. cong, LU, C., and LIU, F. (2020). "Microstructure and mechanical properties of fine grained uranium prepared

by ECAP and subsequent intermediate heat treatment.” *Trans. Nonferrous Met. Soc. China*, 30(10), 2749–2756.

APPENDIX I

Table 3 Mode I test readings for Sample A2

Distance from crack tip mm	δ mm	P N	δ/a_0	G _{1C}	C δ/P	MBT kJ/m ²
0	2.3752	66.3748	0.0475	NL	0.0357847	0.189184
0	2.35003	65.48492	0.047	VIS	0.0358866	0.18467
1	2.3752	66.3748	0.04657		0.0357847	0.185475
2	2.40007	45.95148	0.04616		0.0522305	0.127254
3	2.45011	47.43668	0.04623		0.0516501	0.131576
4	2.50016	48.04456	0.0463		0.0520384	0.133466
5	2.60013	48.1135	0.04728		0.0540416	0.136474
10	3.10003	45.5504	0.05167		0.0680571	0.141208

15	3.55	41.00702	0.05462	0.0865705	0.134377
20	4.04996	40.30513	0.05786	0.1004825	0.139915
25	4.65013	36.97123	0.062	0.125777	0.137537
30	5.25	33.43679	0.06563	0.1570127	0.131657
35	5.95013	32.51557	0.07	0.1829933	0.136568
40	6.52507	30.20314	0.0725	0.2160395	0.131385
45	7.34998	28.04112	0.07737	0.2621144	0.130169
50	8.20031	26.93816	0.082	0.3044124	0.132541
55	8.75019	25.12708	0.08334	0.3482374	0.125638

Table 4 Readings for Mode II non- Pre-cracked specimen

Specimen no	CC Loads (N)		Compliances (mm/N) C			A	m	P _{max}	G _{IIc}	Elf
	at a ₁	at a ₂	at a ₁	at a ₀	at a ₂	(mm/N)	1/(Nmm ²)	(N)	kJ/m ²	
1	400	400	0.00212	0.0015625	0.0014085	0.001	0.00000001	912.5	0.449634375	4961661
2	450	450	0.002	0.00151515	0.0012658	0.001161	0.00000001	798	0.34387416	4273426
3	400	700	0.0022222	0.00166667	0.0013699	0.001252	0.00000002	864	0.80621568	3964381
4	432	432	0.0021739	0.0015625	0.0013333	0.001188	0.00000002	988	1.05423552	4177432
5	485	485	0.0022727	0.00169492	0.0014493	0.001316	0.00000001	880	0.418176	3769486
6	375	750	0.0020833	0.00153846	0.0012821	0.001161	0.00000001	955	0.4924935	4275304
7	450	850	0.0020833	0.0015625	0.0012987	0.001186	0.00000001	872	0.41060736	4185254
8	406	810	0.0021277	0.0015625	0.0012987	0.001172	0.00000001	957	0.49455846	4232307
9	450	850	0.002	0.00153846	0.00125	0.001158	0.00000001	946	0.48325464	4283424
10	450	875	0.0021739	0.00163934	0.0013333	0.001223	0.00000001	933	0.47006406	4057855

Table 5 Readings for Mode II Pre-cracked specimen

Specimen no	CC Loads (N)		Compliances(mm/N) C			A	m	P _{max}	G _{IIc}	Elf
	at a ₁	at a ₂	at a ₁	at a ₀	at a ₂	(mm/N)	1/(Nmm ²)	(N)	(kJ/m ²)	
1	450	450	0.0027027	0.00188679	0.0014706	0.001294	0.00000002	619	0.41381388	3835130
2	350	450	0.0025641	0.00178571	0.0013889	0.00122	0.00000002	648	0.45349632	4066502
3	350	350	0.0025641	0.00185185	0.0014085	0.001267	0.00000002	625	0.421875	3916936
4	256	513	0.0028571	0.00196078	0.0015385	0.001339	0.00000002	609	0.40055148	3706466
5	228	457	0.0027027	0.00196078	0.0014706	0.001327	0.00000002	610	0.401868	3737795
6	229	458	0.0027778	0.00181818	0.0014706	0.00124	0.00000002	675	0.492075	4000791
7	253	506	0.0026316	0.00181818	0.0014085	0.001231	0.00000002	626	0.42322608	4029546
8	235	470	0.0025	0.00178571	0.0013514	0.001208	0.00000002	667	0.48048012	4108730
9	250	500	0.002439	0.00172414	0.0013514	0.001198	0.00000002	665	0.477603	4142727
10	249	499	0.0026316	0.00185185	0.0013333	0.001183	0.00000002	933	0.41649228	4192681

DETAILS OF PUBLICATION:

Sl. No.	Name of Authors	Title of Paper	Name of the Journal/Conference	Month & Year of publication	Category
1	S Sachin, Shivananda Nayaka H	Mechanical properties and Corrosion behaviour of ECAP Processed Cu-Ni alloy in NaCl solution.	International conference on Recent Trends in Mechanical Engineering Sciences 2022	June 2022	4
2	S Sachin, Shivananda Nayaka H	Investigation of microstructure and mechanical properties of Cu Ni alloy processed by Equal Channel angular pressing	The Journal of Mechanical Engineering Science	(Replied to reviewers' comments)	1
3	S Sachin, Shivananda Nayaka H	Microstructural study and mechanical characterization of ECAP processed C70600 alloy	Journal of The Institution of Engineers (India): Series C	May-22	1
4	S Sachin, Shivananda Nayaka H, Santhosh B, Prasad Krishna	Experimental investigation of Mode I & Mode II fracture toughness on T300/914 composite	8th International Engineering Symposium (IES 2019)	Mar-19	4
5	S Sachin, Shivananda Nayaka H, Santhosh B, Prasad Krishna	Experimental Investigation of Interlaminar Fracture Toughness in Aerospace Structural Composite T300/914	Materials Today: Proceedings https://doi.org/10.1016/j.matpr.2020.01.055	Feb-20	1
6	S Sachin, Shivananda Nayaka H, Santhosh B, Prasad Krishna	Experimental Study of Mode I and Mode II Interlaminar Fracture Toughness on Aerospace Structural Composite T300/914	AIP Conference Proceedings https://doi.org/10.1063/1.5085578	Jan-19	1
7	S Sachin, Prasad Krishna, Shivananda Nayaka H	Enhancement of Ablation resistance of carbon/ carbon composite used in spacecraft structures- A review	International Conference on Composite Materials and Structures- ICCMS 2017	Dec-17	3

Category 1: Journal paper, full paper reviewed

3: Conference/Symposium paper, full paper reviewed

2: Journal paper, Abstract reviewed

4: Conference/Symposium paper, abstract reviewed

BIO-DATA

Name : S Sachin
Father's Name : R Sateesh
Date of Birth : 13-07-1992
Nationality : Indian
Marital Status : Single

Address:

Permanent Address

Present Address

S Sachin s/o R Sateesh Flat-1, Floor-1, Block-D, Ramdatt Apartments, Keshwapur, Hubli, Dharwad (Dist.) Karnataka-580023	Department of Mechanical Engineering, National Institute of Technology Karnataka, Srinivasanagar, Dhakshina Kannada (Dist.), Karnataka,- 575025
--	--

Mobile Number : +91-7829646368

E-mail id. : sachin.sateesh6666@gmail.com

Educational Qualification:

Qualification	College/school	University/Board	Year of Passing	Performance
Ph.D. in Mechanical Engineering	National Institute of Technology Karnataka	National Institute of Technology Karnataka	On going	8.25 (CGPA)
M. Tech in Materials Science and Engineering	Bangalore Institute of Technology	Visvesvaraya Technological University (VTU)	2016	79.8%
B. E in Mechanical Engineering	SDM college of Engineering and Technology	Visvesvaraya Technological University (VTU)	2014	8.44(CGPA)

I declare that above information is true and correct to best of my knowledge.

S Sachin
13/07/2022
(Sachin)